POLITECNICO DI TORINO

Master of Science

in Energy and Nuclear Engineering

Master's Degree Thesis

Dynamic Performance Analysis of a Thermochemical Resorption System for Low-grade Heat Storage and Cogeneration of Power and Cold

Supervisors:

Prof. Vittorio Verda

Prof. Adriano Sciacovelli

Candidate:

Jonas Antonio Miguel Parker

ID: s254870

Academic Year 2019/2020

Acknowledgements

Coming to the end of this journey, I would like to express my deep gratitude to my supervisor Dr. Adriano Sciacovelli for his continuous guidance and wise suggestions throughout this research experience. I also wish to offer my warm thanks to Robin Fisher and Gabriele Humbert for their kind help and friendship during my time as a visiting student at the University of Birmingham. Despite the strange historical moment characterizing my stay, I will always keep a beautiful memory of this experience.

Finally, I would like to express my profound thanks to my parents for their support and loving encouragement throughout my whole academic path. I gratefully dedicate this thesis to them.

Abstract

Thermochemical Sorption Systems can provide multiple functions, including storage of low-grade thermal energy, heat upgrade, cold production and provision of power when coupled with adequate turbomachines. As such, they have the potential to play a significant role in the decarbonization of industrial processes whose energy demand is dominated by thermal needs. Thermochemical Resorption Systems exploit two reversible solid-gas chemisorption reactions to store thermal energy in the form of chemical potential during the charge phase, while producing cold and/or heat during the discharge phase. This work investigates the performance of a thermochemical resorption system for recovery and storage of low-grade heat and cogeneration of cold and power through a scroll expander (TRSC). The work focuses on the study of dynamic performance and addresses the relationship between components behavior and system performance.

A series of metal chlorides – NH_3 reactions to be employed in the TRSC under investigation have been evaluated. The performance analysis of different TRSC configurations suitable to meet the requirements of cold and work production of 120 kWh and 12 kWh respectively, with a hot source temperature in the range of 100-200 °C has been carried out. Firstly, the efficiency of the ideal thermodynamic cycle was investigated. Subsequently, the system performance including the effective thermal masses of the sized reactors was analyzed in the steady state case. A dynamic model accounting for the effects of chemical reaction kinetics within such a system was implemented for the first time. The dynamic model was used to explore the transient behavior of relevant quantities, as well as the impact of operating parameters on the cycle time. The thermodynamic efficiency of the ideal cycle revealed to be higher for TRSC configurations adopting lower hot source temperature and higher expander pressure ratio. The system energy efficiency ranges between 0.19 and 0.57, with a maximum energy density of 91.7 kWh/m^3. The intrinsic property of the solid/gas reaction that mostly affects the efficiency loss between ideal and sized system due to thermal masses was found to be the specific adsorption capacity. The dynamic analysis showed that selecting an expander pressure close to the maximum admissible value causes the reaction charge time to increase drastically. Moreover, imposing a larger pressure difference between the two reactors prior to adsorption/desorption allows to reduce the reaction discharge time.

Motivations for the present work

1) Study the influence of cycle parameters and intrinsic properties of solid/gas reactions on the steady state performance of the TRSC.
2) Build a dynamic model for TRSC to investigate the transient evolution of relevant physical quantities.
3) Address the relationship between dynamic system performance and components behavior of TRSC.

Table of Contents

List of Figures

APPENDIX

List of Tables

Nomenclature

Symbols

A	Surface [m^2]
A_r	Arrhenius factor
c	Specific heat [J/kg/K]
$\bar{c}$	Molar heat capacity [J/mol/K]
E	Exergy [J]
e	Specific exergy [J/kg]
E_{rel}	Percentage relative error [%]
ed_m, ed_V	Solid/gas specific energy [J/kg], energy density [J/m^3]
ED_m, ED_V	System total specific energy [J/kg], total energy density [J/m^3]
f_{EG}	Graphite ratio
ΔH	Heat of reaction [J]
$\Delta \bar{h}$	Molar heat of reaction [J/mol]
h	Specific enthalpy [J/kg]
L	Work [J]
l	Specific work [J/kg]
m	Mass [kg]
$\dot{m}$	Mass flow rate [kg/s]
$\bar{M}$	Molar mass [kg/mol]
n	Number of moles [mol]
p	Pressure [Pa]
PD_m, PD_V	Total system mass power density [W/kg], volume power density [W/m^3]
Q	Thermal energy [J]
$\dot{q}$	Heat transfer rate [W]
q	Specific thermal energy [J/kg]
R	Gas constant [J/mol/K], Thermal resistance [K/W]
R_v	Volumetric expansion ratio
$r_{p,T}$	Heat of reaction at fixed pressure and temperature [J/kg]
$\Delta \bar{s}$	Molar entropy of reaction [J/mol/K]
s	Specific entropy [J/kg/K]
S_C	Specific adsorption capacity [kg_{NH_3}/kg_s]
T	Temperature [K]
t	Time [s]
U	Global heat transfer coefficient [$W/m^2/K$]

$\Delta\bar{v}_S$	Molar volume variation between solids at high and low ammonization state [m^3/mol]
v	Specific volume [m^3/kg]
V	Volume [m^3]
W	Power [W]
x	Global conversion rate

Greek letters

β	Pressure ratio
γ	Heat capacity ratio
δ	Deviation, relative percentage deviation [%]
η	Efficiency
λ	Sensible heat coefficient [$kg_S K/kg_{NH_3}$]
ν	Stoichiometric coefficient
ξ	Expander coefficient
ρ	Density [kg/m^3]
τ	Metal ratio

Superscripts

0	Standard reference conditions
$*$	Adsorbed state

Subscripts

0	Standard reference conditions; ambient sink/source
I	First law-related
II	Second law-related
ads	Adsorbed; adsorption
b	Reactive bed
C	Cold source/sink; refrigeration
c	Charge phase
$comp$	Compressor
d	Discharge phase
des	Desorbed; desorption
e	Expander outlet
EG	Expanded graphite
eq	Thermodynamic equilibrium
exp	Expander
f	Heat transfer fluid

H	Hot source/sink; high level
h	HTR/HTM
HP	Heat pump
HX	Metal of heat exchanger
id	Ideal
in	Inlet
is	Isentropic
j	Generic point of thermodynamic cycle related to HTM or LTM
L	Low level
l	LTR/LTM
m	Intermediate sink/source; normalized with respect to the mass
NH_3	Ammonia-related
ORC	Organic Rankine cycle
out	Outlet
$pump$	Pump
r	Reaction
RF	Refrigeration cycle
s	Pure solid; pure salt
S_1, S_2	Solid at low ammonization state, high ammonization state
sen	Sensible
t	Related to quantities integrated in time
TM	Thermal mass
tot	Stoichiometric amount of ammonia; total
vap	Vapor; gas

Acronyms/Abbreviations

COP	Coefficient of performance
G	Gas
HTF	Heat transfer fluid
HTM	Hight temperature material
HTR	High temperature reactor
L	Liquid
LTM	Low temperature material
LTR	Low temperature reactor
S	Pure solid; pure salt
$TRSC$	Thermochemical resorption system for heat storage and cogeneration of power and cold
V_1, V_2	Valve 1, 2

1. Introduction

Low-grade heat recovery and exploitation has great potential to drive the energy sector towards a more sustainable future. The first part of the following chapter aims to present the current industrial decarbonization context and the main available technologies and pathways for the recovery of low-grade thermal energy to convert it into useful products. Subsequently, the physical and working principles of sorption systems are described to introduce the reader to the specific system analyzed in this work (TRSC). Finally, after a literature review on thermochemical sorption systems for power and cold production is carried out, the motivations for the present study are illustrated.

1.1 Low-grade heat recovery: an opportunity for decarbonization

The reduction of greenhouse gas emissions (GHG) is an international long-term commitment of pivotal importance to tackle the dramatic effects of climate change. Pursuant to the Paris Agreement, each nation must undertake paramount measures to limit the global temperature rise to 1.5 ℃ by the year 2100 [1]. To meet such a goal, it is estimated that the maximum allowable carbon budget is 770 $GtCO_2$, while the current GHG emission rate is about 42 $GtCO_2$/year [2]. Moreover, recent projections forecast an increment of global energy consumption of approximately 50% between 2018 and 2050, with 70 % of the increase occurring in non-OECD developing countries, as a result of their rapid economic growth [3]. In such a challenging scenario, low-grade heat recovery and utilization represents a promising opportunity to favor the decarbonization of the energy sector. On one hand, it can promote the share of renewable low-temperature thermal sources, such as solar and geothermal heat, in the overall energy mix. On the other, it allows to valorize waste thermal energy coming from industrial processes: studies reveal that in Europe 20 % to 50 % of the industrial energy consumption is discharged as waste heat to the environment [4]. Exploiting industrial waste heat through thermally efficient technologies allows to obtain crucial benefits in terms of lower fuel consumption, higher industrial energy efficiency, and reduced noxious emissions [5]. The temperatures at which waste heat is released vary in a broad range, from 30 ℃ to more than 1000 ℃, depending on the process. Hence, based on the discharge temperature, waste heat is generally distinguished as high-grade ($T > 650$ ℃), medium-grade ($200 - 300$ ℃ $< T < 650$ ℃) and low-grade ($T < 200 - 300$ ℃). As shown in Figure 1.1, the industrial waste thermal energy in the low-grade heat range is between 66 % and 89 % of the total industrial waste heat discharged to the environment.

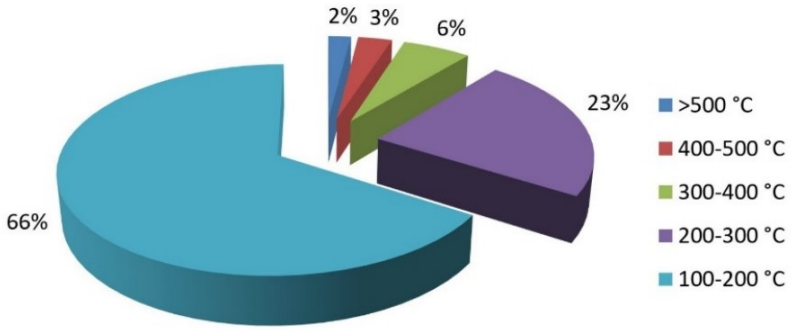

Figure 1.1: Waste heat temperature distribution in the industry [4].

1.2 Barriers to low-grade heat exploitation

Although the recovery and utilization of low-grade heat can provide significant advantages, it is far less feasible and more challenging with respect to exploiting high and medium-grade heat. Indeed, several technical and economic barriers prevent low-grade heat technologies to be widely employed in commercial applications. For instance, low-grade thermal energy has limited potential to be converted efficiently into mechanical work and electrical energy. Such a concept can be clarified by considering the definition of exergy:

$$E = Q\left(1 - \frac{T_0}{T}\right) \tag{1.1}$$

The exergy associated to a certain amount of heat Q available at temperature T represents the maximum work achievable through an ideal device exploiting completely Q and interacting exclusively with the environment at temperature T_0 [6]. Indeed, the term in the brackets in equation 1.1 represents the Carnot factor, i.e. the efficiency of conversion of thermal energy into work through an ideal Carnot machine: as a consequence of the second law of thermodynamics, a part of the heat used in an ideal thermal machine cannot be converted into work and is unavoidably rejected to the ambient:

$$Q_0 = Q - E \tag{1.2}$$

The amount of heat Q_0 that is not converted into work depends on the temperature of the heat source, in relation with the environmental temperature. As an example, let us consider an available amount of heat $Q = 1\,\mathrm{kWh}$, that can be provided at temperature T. Figure 1.2 represents the exergy related to Q, with two different values of environmental temperature T_0.

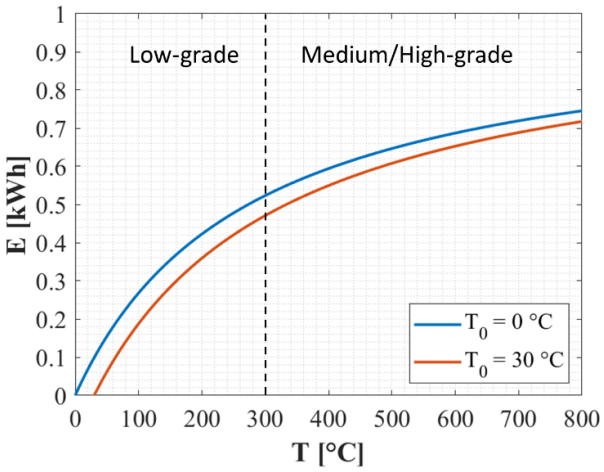

Figure 1.2: Exergy associated to 1 kWh of thermal energy available at different temperatures *T*, at environmental temperature of 0 °C and 30 °C. The exergy reduces as the heat source temperature is closer to the ambient temperature.

It can be observed that the exergy decreases as the hot source temperature gets closer to the ambient temperature. Therefore, recovering heat in the low-grade heat range to produce work is less convenient since, even by adopting an ideal Carnot device, the conversion efficiency is lower compared to the case in which the temperature of the source is in the medium or high-grade range.

Additional techno-economic limits for low-grade heat utilization are related to heat exchangers [7]. For instance, the heat transfer rate between two energy carriers through a surface can be expressed by the following general equation:

$$\dot{q} = UA\Delta T_{ml} \tag{1.3}$$

Where U is the global heat transfer coefficient, A is the surface area and ΔT_{ml} is the logarithmic mean temperature difference, which is defined based on the heat exchanger configuration. If ΔT_{ml} between the low-grade heat source and the energy sink stream is low, a larger heat exchanger may be required to achieve optimum heat transfer, resulting in higher costs. Furthermore, if the waste stream is flue water vapor in the low-grade heat range, water droplets might mix with other particles, causing the deposit of corrosive solids onto the heat exchanger surfaces. The consequent need for advanced materials minimizing corrosion and reducing maintenance can negatively impact on the cost of low-grade heat recovery applications.

The limits mentioned so far represent only few examples among the challenges to promote wider commercial low-grade heat applications in the future. Research and development have been advancing to overcome technical constraints and increase the efficiency of established systems for low-grade heat utilization, as well as investigate emerging technologies, working fluids, and materials [5].

1.3 Overview on low-grade heat applications

The following section aims to carry out a non-exhaustive review of benchmark solutions for low-grade thermal energy exploitation, as well as to illustrate the technological framework in which the system analyzed in this work (TRSC) is placed. As shown in Figure 1.3, low-grade thermal energy can generally be used for heating, cooling and power production purposes. A further category considered is Thermal Energy Storage (TES), which allows to overcome the time and distance mismatch between energy demand and low-grade heat recovery. In other words, low-grade heat can initially be stored in TES during charge phase, to be indirectly used for heating/cooling and power production during discharge phase.

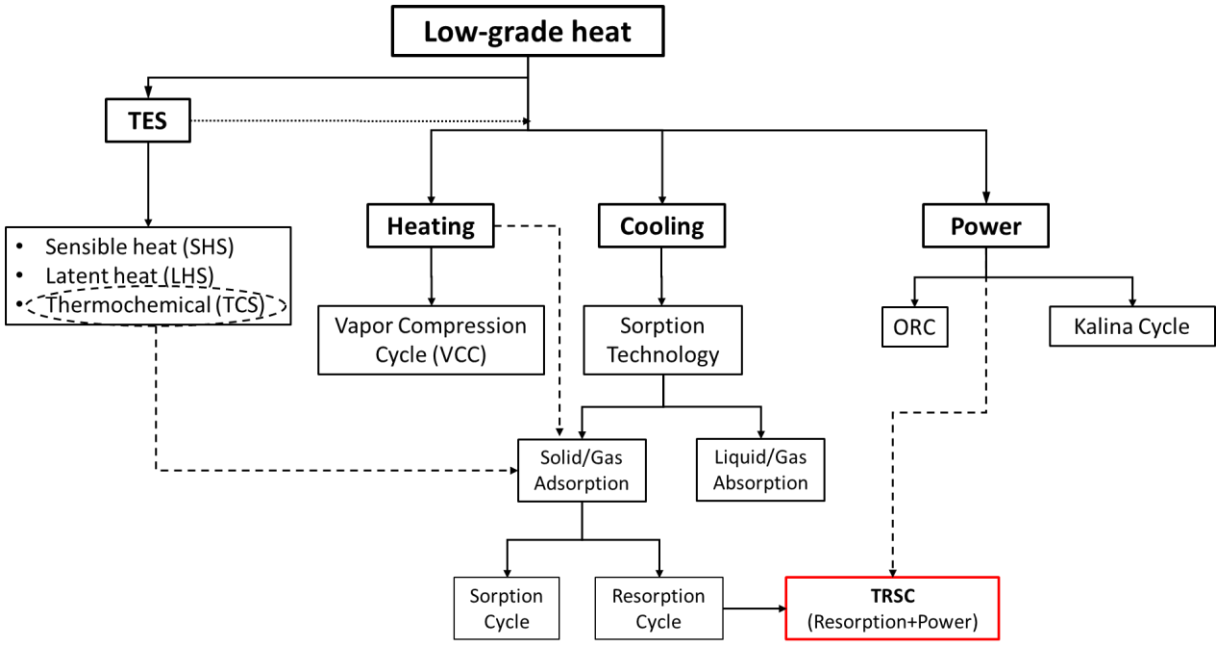

Figure 1.3: Possible pathways for usage of low-grade heat. TRSC combines a resorption cycle with a turbomachine to produce power. The dashed lines indicate further non-conventional uses of low-grade heat.

Conventional cycles for low-grade heat recovery and power generation are the Organic Rankine Cycle (ORC) and the Kalina cycle. On the other hand, low-grade is typically used in sorption systems to provide refrigeration, or in vapor compression cycle operating as heat pumps to supply heating. The dashed line in the scheme indicates further possible functions that can be achieved exploiting low-grade, other than the conventional ones: solid/gas adsorption technologies can provide not only refrigeration, but also heating, storage and power. The studied thermochemical system (TRSC) is classified as resorption system (red box in Figure 1.3) and it combines solid/gas adsorption technology with the use of a scroll expander to provide both thermochemical storage function and cogeneration of power and cold.
In the next paragraphs a brief description of the benchmark systems for low-grade heat utilization illustrated in Figure 1.3 is carried out. Subsequently, operating principles of sorption technology and sorption-based cycles are described more in detail.

1.3.1 ORC

Organic Rankine cycles derive from the basic steam-based Rankine cycle, with the main difference that the working fluids are organic compounds with lower boiling points, critical points and viscosity than water [5]. The low boiling temperature of the organic compounds allows to exploit thermal energy at lower temperature to produce work, with respect to the standard Rankine cycle. Such compounds can be classified as organic refrigerants, hydrocarbons, and siloxanes. The components of the standard ORC are an evaporator, a condenser a pump and an expander (Figure 1.4).

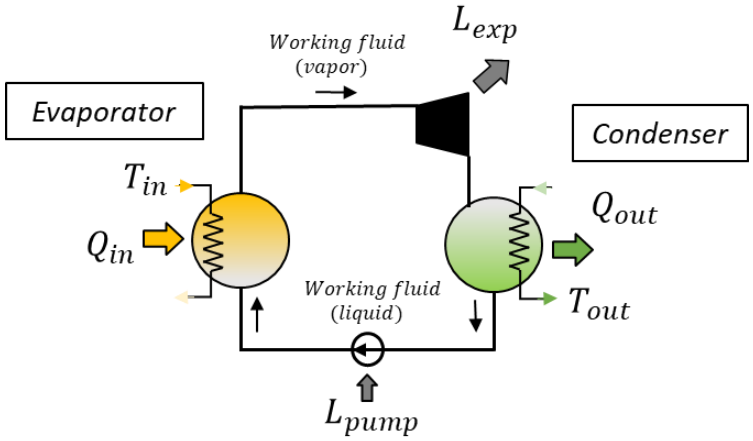

Figure 1.4: Schematic diagram of ORC.

In the evaporator low-grade heat Q_{in} is exploited to obtain high pressure vapor working fluid, which then expands to produce mechanical work L_{exp}. The fluid leaving the expander is now a mixture of liquid and vapor at low pressure, which is liquefied in the condenser. The saturated liquid is pumped back to the evaporator and the cycle repeats. The cycle efficiency of ORC is defined as:

$$\eta_{ORC} = \frac{L_{exp} - L_{pump}}{Q_{in}} \qquad 1.4$$

Several improvements of the ORC have been proposed for better use of low-grade thermal energy [8]. For instance, in ORC with recuperator the residual sensible heat of the vapor exiting the expander is used to preheat the working fluid before it enters the evaporator. Therefore, at fixed work production, less heat is needed to achieve organic fluid evaporation, resulting in an increment of the cycle efficiency η_{ORC}.

1.3.2 Kalina Cycle

The standard Kalina cycle is essentially a variation of the Rankine cycle in which the working fluid is a solution of two substances with different boiling points, typically ammonia/water. Similarly to the ORC, the lower boiling point of the mixture rich in ammonia allows to exploit

thermal energy available at various temperatures in the low-grade range. Moreover, compared to water-base cycles, ammonia rich solutions achieve higher working pressure at the expander inlet, resulting in higher thermodynamic efficiency. In Kalina cycles a separator is commonly implemented to decrease the percentage of ammonia in the solution before condensation (Figure 1.5). Indeed, a very low temperature coolant would be required to liquify an ammonia rich mixture, making the process less feasible.

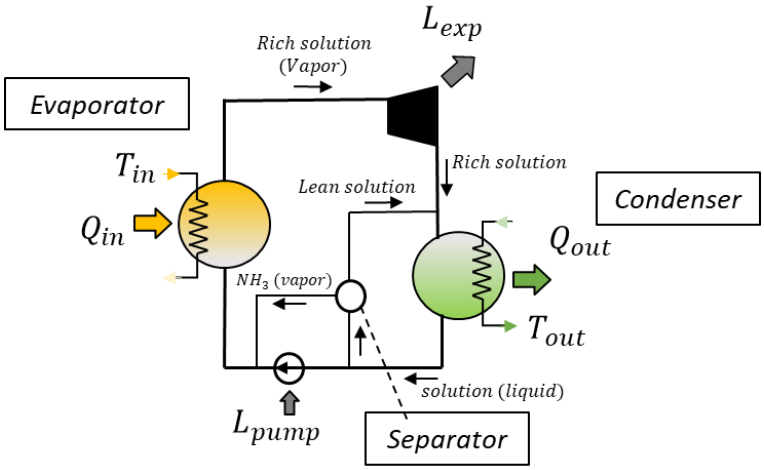

Figure 1.5: Simple Kalina cycle with a separator [7].

In the configuration shown in Figure 1.5, the separator operates between the expander and the condenser. Therefore, the rich solution stream exiting the turbine is diluted with lean solution coming from the separator before undergoing condensation. The lean solution is obtained by separating a fraction of liquid solution exiting the condenser from NH_3 vapor. The rich solution is regenerated at the pump outlet mixing separated NH_3 vapor with the other fraction of liquid solution. The working principles of the separator is usually based on liquid-gas absorption phenomena (Section 1.3.5).
Another advantage of Kalina cycles with respect to Rankine/ORC systems is the additional degree of freedom given by the composition of the ammonia-water solution. More specifically, adjusting the composition of the solution allows to obtain different high and low pressure levels of the system, i.e. higher operating flexibility [9].

1.3.3 Thermal Energy Storage (TES)

TES systems can be classified depending on the physical principles which provide the storage process:

- *Sensible heat storage (SHS)*, in which thermal energy is stored by means of a temperature variation of the storage medium. Hence, the capacity of SES depends on the mass and specific heat capacity of the adopted material. Major drawbacks of SES are large space requirements and high thermal losses [10].

- *Latent heat storage (LHS),* which exploit the phase change of a material to store thermal energy. Hence during charge phase heat is used to activate the phase change of the storage material at constant temperature. During discharge the reverse process is accomplished and thermal energy is obtained in the form of latent heat of the phase changing medium.
- *Thermochemical storage (TCS),* in which thermal energy is stored in the form of heat of reaction in reversible chemical reactions or in sorption processes. Main advantages of TCS are the large energy density and low thermal losses.

TRSC can be classified as thermochemical storage since it exploits reversible solid/gas sorption reactions to store heat in the form of chemical potential. Thermal energy storage in the industrial sector for low-grade waste heat recovery can provide several benefits, such as fossil fuel consumption reduction and increased process flexibility.

1.3.4 Vapor compression cycle

Vapor compression cycles (VCC) are considered as the most mature technology for heat pumping, refrigeration, and dehumidification purposes. Typical working fluids adopted in commercial applications are water, R134a and R407c refrigerants. VCC application for low-grade heat exploitation is a heat pump providing energy upgrade: the low-temperature thermal input Q_{in} supplied is upgraded to high temperature heat Q_{out}, available to the user. The standard VCC consists in a compressor, an evaporator, a condenser, and an expansion valve (Figure 1.6).

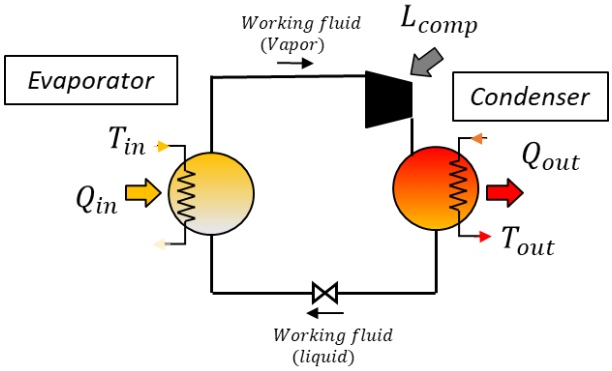

Figure 1.6: Vapor compression cycle.

The working principles of the heat pump starting from the evaporator can be summarized as follows: the working fluid coming from the expansion valve undergoes evaporation extracting heat low-grade heat Q_{in} at low pressure. Saturated vapor refrigerant is then compressed at high pressure state and liquefied in the condenser, supplying heat at higher grade Q_{out}. Saturated liquid refrigerant is expanded in the valve and the cycle repeats. The coefficient of performance (COP) of vapor compression cycle is defined as the ratio between the useful effect and the energetic expense, which in the case of heat pump is:

$$COP_{HP} = \frac{Q_{out}}{L_{comp}} = \frac{Q_{out}}{Q_{out} - Q_{in}} \quad 1.5$$

In refrigeration cycles the input heat Q_{in} represents the cooling effect, thus it is the useful product, while Q_{out} is rejected to an external source. Hence the COP for refrigeration cycles is:

$$COP_{RF} = \frac{Q_{in}}{L_{comp}} = COP_{HP} - 1 \quad 1.6$$

1.3.5 Sorption technology

Sorption refrigeration cycles are in general classified as thermal cooling technology, based on the form of the primary energy input [11]. They essentially work as conventional VCC cooling systems, with the main difference being that mechanical energy input is substituted with thermal energy. Two main categories of sorption refrigeration cycles can be defined depending on the type of technology:

- *Liquid/gas absorption cycles.* During absorption phenomena the molecules of the adsorbate penetrate the surface layer of the sorbent, entering the structure of the bulk liquid, resulting in a single sorbent/adsorbate solution (bulk phenomenon). The process of separation between the two substances (desorption) requires heat to cause the adsorbate to evaporate out, hence it is endothermal. On the other hand, the absorption process is exothermal since the adsorbate releases latent heat as it is mixed with the liquid phase of the solution. The most common liquid/gas working fluids employed in absorption cycles are LiBr/water and water/NH_3 [12]. Liquid/gas absorption cycles are feasible for low-grade heat applications, since the thermal input to drive desorption can be supplied at various ranges of low temperatures, depending on the boiling point of the binary solution adopted. An important feature of absorption refrigeration cycles is that they operate in a continuous state, hence they are intrinsically unfeasible for thermal energy storage purposes.
- *Solid/gas adsorption cycles*, which exploit physical sorption or chemisorption principles. In adsorption processes a gaseous substance is adsorbed/desorbed onto a solid surface, by means of intermolecular or chemical bonds, thus it is a surface phenomenon. To break such bindings, thermal energy is required, meaning that desorption is an endothermal process. On the other contrary, once the bindings between adsorbate and sorbent generate, the intensity of the surface interactions decrease and the corresponding potential energy is converted into heat, implying the exothermicity of adsorption. Differently with respect to absorption cycles, solid/gas adsorption cycles typically consist of two operation steps shifted in time, enabling the storage function. Working principles of solid/gas adsorption cycles are illustrated more in detail in the next section.

1.4 Solid/gas adsorption technology

Solid/gas adsorption technologies have been extensively investigated in literature (e.g., [13],[14]). Typically, two different processes can occur during adsorption:

- Physical adsorption (physisorption), driven by weak intermolecular binding forces, e.g., Van der Waals forces. It generally takes place on the surface of the sorbent and it does not involve decomposition of the molecules. Common physical adsorption working pairs are NH_3/activated carbon and water/silica gel.
- Chemical adsorption (chemisorption), consisting of chemical reactions occurring between adsorbate and sorbent on the first surface monolayer, with the formation of new molecules. Thus, chemisorption phenomena are characterized by covalent or ionic chemical bonds, with binding forces much stronger with respect to physisorption. Typical working pairs for chemisorption processes are salt hydrates/water or metal chlorides/NH_3.

Chemical adsorption and desorption are also referred to as synthesis and decomposition, respectively. Solid/gas adsorption processes can be represented as a chemical reaction occurring between the mixture composed of sorbent S_1 and gas G in desorbed state, and the solid substance S_2 in adsorbed state:

$$Adsorption: \quad S_1 + G \Rightarrow S_2 + \Delta H_r \quad exothermal \tag{1.7}$$

$$Desorption: \quad S_2 + \Delta H_r \Rightarrow S_1 + G \quad endothermal \tag{1.8}$$

Where ΔH_r is the heat of reaction absorbed/released during desorption/adsorption. Because of the strong bindings occurring in chemical adsorption processes, ΔH_r is much higher for chemisorption phenomena with respect to physical adsorption processes. The equilibrium state for physisorption and chemisorption reactions are modeled in different ways: the equilibrium state for physical adsorption is defined by two independent variables, i.e. pressure and temperature. On the other hand, chemisorption equilibrium state is represented by one independent variable. Hence, the pressure of a solid/gas chemisorption reaction is commonly defined as a monovariant function of its temperature through the Clausius-Clapeyron equation:

$$p_{eq} = f(T_{eq}) \quad \Rightarrow \quad ln\left(\frac{p_{eq}}{p_0}\right) = -\frac{\Delta \bar{h}_r^0}{RT_{eq}} + \frac{\Delta \bar{s}_r^0}{R} \tag{1.9}$$

$\Delta \bar{h}_r^0$ and $\Delta \bar{s}_r^0$ are respectively the molar heat and entropy of reaction at standard reference conditions, and they are specific properties of the considered chemical reaction. Therefore, each reaction is defined by one equilibrium state. Once the equilibrium condition is reached the amount of adsorbed refrigerant cannot change, until the reactive complex is put outside such equilibrium. Liquid/gas (L/G) equilibrium is also monovariant, and it can be represented with an equation similar to 1.9:

$$Evaporation: \quad L + \Delta H_{vap} \Rightarrow G \tag{1.10}$$

$$Condensation: \quad G \Rightarrow L + \Delta H_{vap} \tag{1.11}$$

$$ln\left(\frac{p_{vap}}{p_0}\right) = -\frac{\Delta \bar{h}^0_{vap}}{RT_{eq}} + \frac{\Delta \bar{s}^0_{vap}}{R} \tag{1.12}$$

Where $\Delta \bar{h}^0_{vap}$ and $\Delta \bar{s}^0_{vap}$ are respectively the molar latent heat of vaporization and molar entropy of vaporization at standard reference conditions. The equilibrium state of solid/gas reactions and liquid/gas transformations can be represented in the Clapeyron diagram. As an example, Figure 1.7 shows the equilibrium lines of liquid/vapor ammonia compared to the equilibrium of the following manganese chloride – NH_3 reaction:

$$MnCl_2(NH_3)_2 + 4NH_3 \rightleftarrows MnCl_2(NH_3)_6 \tag{1.13}$$

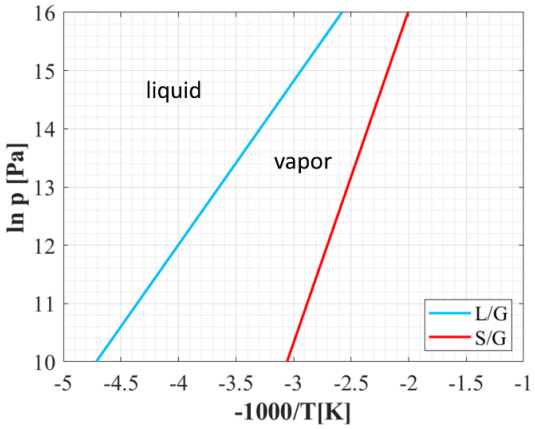

Figure 1.7: Clapeyron diagram representing equilibrium line of solid/gas (S/G) reaction 1.13 compared to liquid/gas (L/G) saturation line of ammonia. The lines are obtained through the Clausius-Clapeyron equations.

The molar enthalpy and entropy of reaction associated to the solid/gas reaction are respectively $\Delta \bar{h}^0_r = 47.42$ kJ/mol and $\Delta \bar{s}^0_r = 132.24$ J/mol/K, while ammonia is characterized by $\Delta \bar{h}^0_{vap}$=23.35 kJ/mol and $\Delta \bar{s}^0_{vap}$=97.41 J/mol/K.

The system analyzed in this work (TRSC) is based on solid/gas chemisorption working principles: it exploits solid/gas sorption heat of reaction to store thermal energy and release heat or produce cold. In the next paragraphs the main solid/gas adsorption cycles are described and reviewed.

1.4.1 Thermochemical Sorption Cycles

Sorption cycles can provide both refrigeration and heat upgrade [15]. Moreover, solid-gas sorption working principles make such systems intrinsically feasible for storage purposes. Hence, the cycle can be divided into two main operating phases shifted in time, defined as

charge and discharge phases. Low-grade heat can be stored during charge phase, while refrigeration effect or upgraded thermal energy can be supplied during discharge phase.

Refrigeration cycle

The basic solid/gas sorption refrigeration cycle is represented in Figure 1.8.

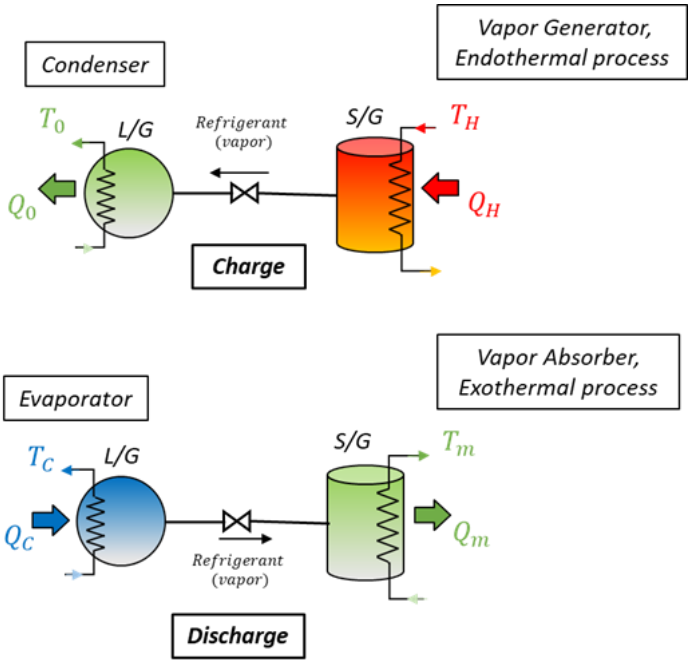

Figure 1.8: Thermochemical sorption refrigeration cycle.

The only two components required are a refrigerant vessel, indicated as L/G, and a reactive bed, indicated as S/G. The refrigerant vessel acts as a condenser during charge phase and as evaporator during discharge phase. The reactive bed acts as a vapor generator in the charge phase, while operating as vapor absorber during discharge phase. During charging phase, the valve is opened and the heat input Q_H to be stored drives endothermal decomposition of the refrigerant from the solid complex in the vapor generator. The gaseous refrigerant, typically water or ammonia, flows towards the condenser where it is liquefied and stored at environmental temperature T_0. When the refrigeration is required, the vessels are connected again, and discharge phase occurs. Thus, the cooling effect Q_C is provided by the evaporation of the refrigerant in L/G vessel. Vapor refrigerant flows towards the absorber vessel where it undergoes exothermal adsorption, releasing heat at intermediate temperature T_m .The ideal thermodynamic path of the working fluid, i.e. the refrigerant, can be represented on the Clapeyron diagram (Figure 1.9):

- *Charge phase:* Hot thermal input Q_H at hot source temperature T_H drives endothermal decomposition of the reactive complex in the vapor generator (point 1). Desorbed gas at high pressure p_H reaches thermal equilibrium with the condenser kept at environmental sink temperature T_0 through an ideal isobaric transformation (1-2). The refrigerant is liquified releasing condensation heat Q_0 to the environment (point 2).

- *Discharge phase:* Cold thermal input Q_C providing refrigeration at cold source temperature T_C drives evaporation of the refrigerant in the evaporator (point 3). The gaseous refrigerant at low pressure p_L reaches thermal equilibrium with the reactive bed kept at intermediate sink temperature T_m through an ideal isobaric transformation (3-4). The refrigerant is adsorbed releasing heat Q_m (point 4).

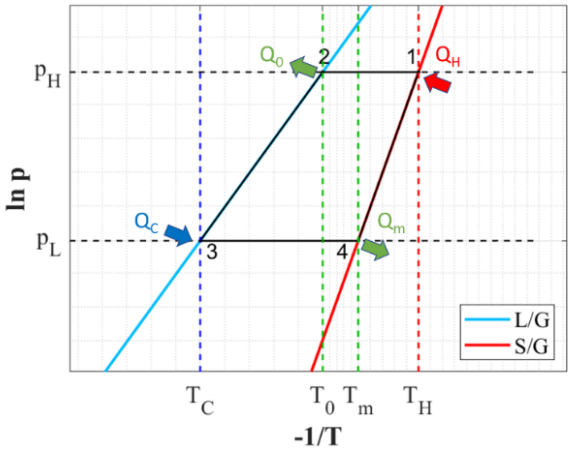

Figure 1.9: Clapeyron diagram of the sorption refrigeration cycle. L/G is the liquid/gas equilibrium line; S/G is the solid/gas adsorption equilibrium line.

Between the charge and discharge phases, an intermediate step is required:

- After the charge phase, the reactive bed and the refrigeration vessel are disconnected and brought respectively to the intermediate sink temperature T_m and cold source temperature T_C. Since the refrigerant liquid/gas and solid/gas equilibria are monovariant the decrease in temperature results in a decrease of pressure (from p_H to p_L) along their corresponding equilibrium lines. Such a phase is commonly referred to as precool phase.
- After the discharge phase, the reversed intermediate step is achieved in a similar way: the reactive bed and the refrigeration vessel are disconnected and brought respectively to the hot source temperature T_H and the environmental sink temperature T_0 (preheat phase).

The coefficient of performance of sorption refrigeration cycle can be defined as the ratio between the thermal energy stored during charge phase and cooling effect provided during discharge phase:

$$COP_{RF} = \frac{Q_C}{Q_H} \qquad 1.14$$

Heat upgrade

As show in Figure 1.10, the structure of the sorption system for energy upgrade is the same as in the refrigeration cycle.

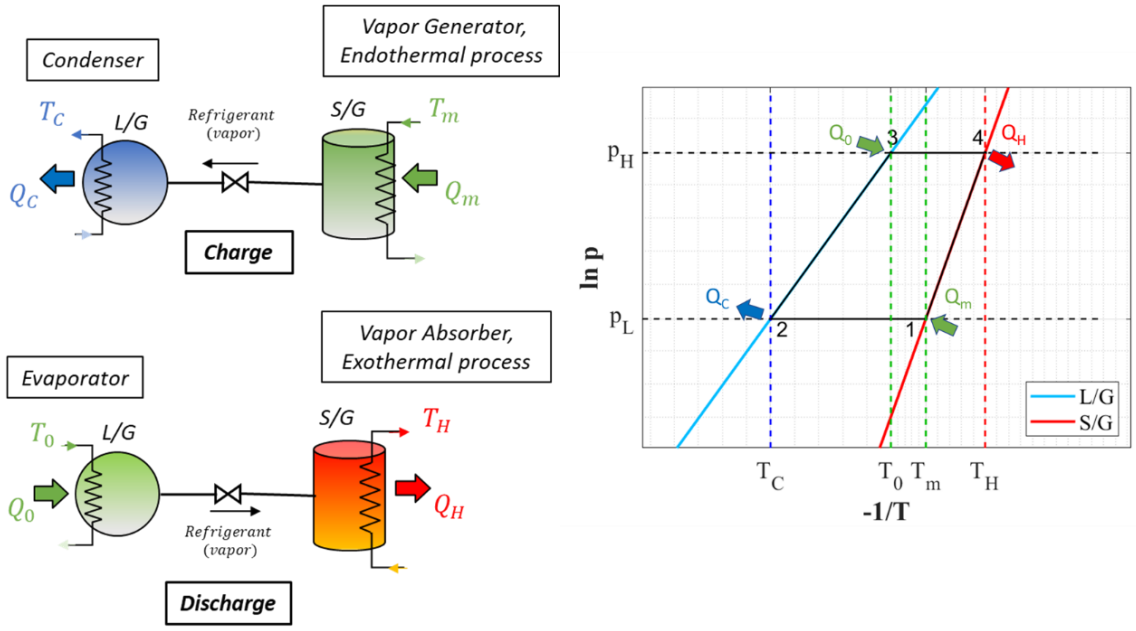

Figure 1.10: Thermochemical sorption cycle for energy upgrade. Left: schematic diagram of the system. Right: ideal thermodynamic cycle on Clapeyron diagram.

However, the heat upgrade cycle is reversed with respect to the refrigeration cycle, and the way the thermal fluxes are managed is different: during charge phase, the thermal input Q_m driving desorption in the vapor generator (point 1) is at an intermediate temperature T_m. The working fluid at low pressure p_L is liquified in the refrigeration vessel acting as a condenser, rejecting heat to the cold sink at temperature T_C (point 2). After the intermediate step at which the vessels are disconnected and brought to the required temperature levels, the discharge phase occurs. Therefore, heat coming from the environmental source Q_0 drives the evaporation in the refrigeration vessel (point 3) and gaseous refrigerant undergoes adsorption at high pressure p_H, releasing useful thermal energy Q_H at high temperature T_H (point 4). Hence, the final useful effect is the upgrade of the available heat Q_m from low-grade (at T_m) to high-grade (at T_H), and the performance of the cycle can be defined as:

$$COP_{HP} = \frac{Q_H}{Q_m + Q_0} \qquad 1.15$$

In sorption cycles for energy upgrade, low-grade heat coming from available waste streams could be used not only during charge phase, but also during discharge phase to drive evaporation in the refrigeration vessel (Q_0 in point 3). The temperature level of the provided thermal energy Q_H can be adjusted depending on the temperature at which the selected waste stream supplies heat Q_0 to the evaporator.

1.4.2 Thermochemical resorption cycles

The basic operating principles of the thermochemical resorption refrigeration cycle is represented in Figure 1.11.

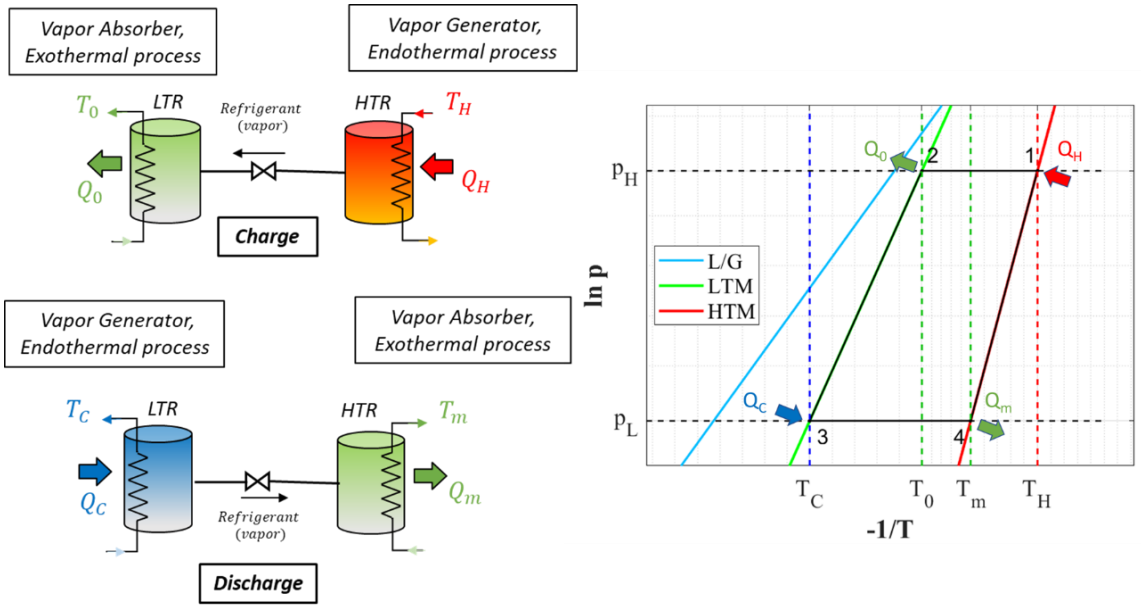

Figure 1.11: Thermochemical resorption refrigeration cycle. Left: schematic diagram of the cycle. Right: ideal thermodynamic cycle on Clapeyron diagram. HTM and LTM are the S/G equilibrium lines of the reactive mixtures inside HTR and LTR.

With respect to sorption cycles, resorption systems consist of two chemical reactors filled with two solid/gas reactive mixtures. Hence, the refrigeration vessel in the simple sorption is substituted with a reactive bed. The two reactors of a resorption cycle are conventionally denominated High Temperature Reactor (HTR) and Low Temperature Reactor (LTR). The solid/gas reactive material composing the HTR is defined High Temperature Material (HTM), while the reactive complex adopted in the LTR is the Low Temperature Material (LTM). The difference between HTM and LTM is related to their thermodynamic properties at equilibrium: at fixed pressure, HTM has a higher equilibrium temperature than LTM. Graphically, as is shown on the right-hand graph of Figure 1.11, the equilibrium line of the HTM is to the right line of the LTM equilibrium line. The working steps are essentially the same as described in the previous section for the sorption refrigeration cycle, with the only difference that in this case the ideal cycle develops on two solid/gas equilibrium lines, i.e. corresponding to HTM and LTM.

Some relevant advantages of thermochemical resorption cycles with respect to solid sorption cycles are summarized:

- At fixed pressure and temperature conditions of the cycle, the resorption system achieves a higher refrigeration COP than the simple sorption system [16]. The reason for this is related to the strong cooling capacity of resorption systems given by the larger decomposition heat of solid/gas reactions compared to refrigerant evaporation heat.

- Wider range in terms of refrigeration temperature and operating pressures of the cycle can be achieved by means of a resorption system rather than adopting a sorption system. Indeed, several solid/gas reactions with different equilibrium lines can be selected as LTM of the resorption system, while a single liquid/gas equilibrium line is associated to the refrigerant in the sorption cycle.
- Resorption refrigeration is more suitable for cold production in some special situations, where the presence of liquid is not desirable.

1.4.3 Comments on solid/gas adsorption cycles

In the representation of the thermodynamic cycle of sorption and resorption systems on the Clapeyron diagram, the decomposition/synthesis reactions are assumed to occur at equilibrium. In a real case, the reactive complex needs to be brought out of the equilibrium state, hence the thermodynamic parameter (p and/or T) of the reactive mixture must deviate from the corresponding equilibrium line (S/G). The operating principles of the reactive components at non-equilibrium conditions are illustrated in the next chapter (2.2.1), describing the kinetics of the reactors.
Besides the capability of achieving storage function, relevant advantages of solid/gas adsorption refrigeration cycles with respect to liquid/gas absorption cycles can be summarized as follows:

- A wider range of working temperatures, since different equilibrium lines are associated to the various solid/gas reactions available. Such a feature makes solid/gas sorption cycles also more suitable for low grade and ultra low-grade heat (< 100 °C) recovery and utilization.
- Higher reliability of the system since the primary process has no moving parts.

There are several studies in literature that investigated the potential of thermochemical sorption cycles. Citing just a few: Wu et al [17] experimentally investigated a thermochemical sorption refrigeration system adopting $SrCl_2/NH_3$ reactive mixture. The system had the advantage of higher refrigeration performance at ultra low-grade heat input compared to physisorption cycles. Li et al. [15] proposed and investigated from a thermodynamic viewpoint a multifunctional sorption heat transformer, able to provide low-grade thermal energy storage, as well as combined cooling and heat supply. Not only did the sorption system prove to be suitable for multifunctional purposes, but It also demonstrated an energy density in the range of 2000-2500 kJ/kg, over ten times higher than conventional sensible and latent heat energy storage systems. The same authors experimentally investigated a dual-mode thermochemical sorption cycle for heat supply and energy upgrade [18]. The work focused on studying direct heat supply and heat upgrade modes during the discharge phase at different ambient temperatures during Winter. With a COP ranging between 0.17 and 0.41 and an energy density of 300-700 kJ/kg, the system showed to be suitable for long-term seasonal storage of solar thermal heat, independently from the ambient temperature. Ma et al [19] studied a thermochemical sorption cycle for seasonal solar thermal energy storage, adopting ammonia as refrigerant, through a dynamic model. An important conclusion was that preferable solid/gas reactions should have

higher slope of the equilibrium line, i.e. higher $\Delta\bar{h}_r^0$, to guarantee low hot source temperature during the charge phase that matches capability of the solar collectors, and relatively high adsorption temperature for heating during the discharge phase.

1.4.4 Sorption technology for combined power and cold: literature review

Cycle concepts that combine power and cold production have recently attracted great interest in the scientific community. Pioneer of power and cold cogeneration cycles, D.Y. Goswami proposed a combination of an ammonia-based Rankine cycle and an ammonia-water absorption refrigeration cycle, capable of providing first law efficiency of 0.32 [20,21]. On the other hand, Ziegler was one of the first researchers to explore the potential of combined power and cold generation in adsorption cycles, which resulted in first law efficiency similar to that of the Goswami cycle [22]. Among the various types of cycles, ammonia-based adsorption cycles for power generation are considered a highly appealing technology, for its greater potential in producing work with respect to water-based cycle, due to the higher working pressure achievable [5]. Furthermore, ammonia is a working fluid featuring relevant advantages compared to other environmentally friendly refrigerants, such as water and methanol. For instance, it is chemically stable, it has a low boiling temperature and ammonia-based chemisorption reactions have a large adsorption capacity: as much as 1 kg of ammonia can be bonded to 1 kg of solid sorbents, [23]. On the other hand, ammonia is classified as group B2 refrigerant in ANSI/ASHRAE Standard 34, meaning that it is characterized by high toxicity and low flammability [24]. Nevertheless, ammonia is safely handled in the industrial refrigeration field for over 100 years and it is considered as a standard refrigerant by the International Institute for Refrigeration [14]. The system investigated in this work adopts ammonia as working fluid.
Several studies were conducted on thermochemical sorption cogeneration cycles, from the point of view of both steady state and dynamic state conditions. A few of them are cited below.

Steady state studies
Wang et al. [25] investigated an ammonia-based resorption cycle for cogeneration of power and cold, proving that theoretically an optimal total exergy efficiency of 0.9 can be obtained, while the highest achievable refrigeration COP is 0.77. The authors in [26] and [27] investigated two similar resorption cogeneration system concepts, designed to operate continuously. Both works are focused on studying the influence of operating parameters, such as heat source temperature and metal to pure solid ratio, on the system performance from the viewpoint of first and second law efficiencies. Lu et al. [28] investigated a dual-source chemisorption power generation cycle obtained by integrating four thermochemical reactors with two expanders. The purpose of such a system configuration is to overcome the intermittency imposed by solid/gas sorption reactions, providing power and refrigeration continuously. Bao et al. proposed an integrated resorption system which combines the chemical reactors with a compressor and an expander. Such a system has the capability to store electricity and low-grade heat during charge, while providing refrigeration, heating and power during discharge [29,30]. Godefroy et al. [31]

carried out an exhaustive performance analysis on a hybrid sorption cycle for low-grade heat storage and cogeneration of power and cold operating in three different modes. The work is focused on first and second law analysis and achieves a parametric study, varying cycles operating conditions and design variables such as metal ratio and expander isentropic efficiency.

Dynamic state studies

Jiang et al. [22] conducted a one-dimensional dynamic study on a resorption cogeneration cycle operating continuously. The work is focused on the performance analysis in terms of COP and specific cooling capacity. The same authors investigated a resorption power generation cycle integrated with PCM storage tanks providing heat and cold storage, through a mathematical model supported by an experimental setup [32]. Bao et al. [33] studied the dynamic performance of a cogeneration cycle for continuous and simultaneous power and cold production, combining a simple chemisorption cycle (Thermochemical Sorption Cycles 1.4.1) with a scroll expander. They concluded that the mismatch between ammonia vapor expansion and adsorption and the non-optimal design of the scroll expander might lead to a dramatic loss in efficiency (about 70 %). Lu et al. [34] carried out the investigation of the dual sources chemisorption power generation cycle [28], conducting a dynamic performance study through an analytical kinetic model.

1.5 Motivations for the present work

Thermochemical resorption cogeneration cycle represents a promising technology, that can provide multiple functions in several applications. However, since it is non-established technology, analytical and experimental investigations at different scales are still required. In this work an ammonia-based thermochemical resorption cycle for low-grade heat storage and cogeneration of power and cold is investigated at system level, in both steady state and dynamic state conditions. The study is conducted on a specific low-grade heat application, adopting Metal Chlorides-NH_3 reactive mixtures in the reactors. The purpose of the work is to increase the knowledge about combined sorption refrigeration and power cycles and to address eventual gaps in the current literature. Therefore, the following objectives have been stated for this thesis:

1) Study the influence of cycle parameters and intrinsic properties of solid/gas reactions on the steady state performance of the system.

The relationship between thermochemical sorption cogeneration steady state performance and cycle operating conditions have been addressed many times in literature. However, limited research analyzes the influence of the intrinsic properties of solid/gas reactions on the system performance. Such an investigation could serve to identify which kind of solid/gas reactions is more suitable for a specific application and system size. Therefore, the following tasks are carried out in the thesis:

- Building a steady state model for TRSC which encompasses the size of the reactors through the definition of thermal masses (Section 3.2).
- Conducting a steady state analysis focused on the correlation between system efficiency and reactive materials properties (Section 5.1).

2) Formulate a Dynamic model for TRSC and transient behavior of relevant physical quantities.

Although several steady/dynamic models have been proposed for thermochemical sorption/resorption cycles for continuous cogeneration of power and cold, there is narrow evidence about dynamic models used to investigate thermochemical resorption cogeneration cycles with storage function. Such models are essential to investigate the system's transient behavior and estimate the performance in terms of power and/or cycle time. Dynamic models for resorption cogeneration cycles should encompass the coupling of the thermochemical reactors operating in non-equilibrium conditions, and the presence of a turbomachine providing work. Therefore, the following specific tasks are conducted in the thesis:

- Building a lumped parameters dynamic model for TRSC including practical assumptions related to the kinetics of the reactions during simultaneous adsorption/desorption of the reactors: the reactive mixtures need to be brought to thermodynamic conditions out of their equilibrium (Section 3.3).
- Discussing the evolution in time of relevant quantities, e.g., temperatures and pressures of the reactors, with the aim to carry out a physical interpretation for such transient trends (Section 5.2).

3) Address relationship between dynamic state system performance and components behavior.

Since limited e.vidence is to be found in literature on dynamic modeling of resorption cogeneration storage cycles, research addressing the correlation between dynamic performance and components behavior is scant. Such kind of study is relevant since it could allow to investigate how system parameters and operating conditions affect the dynamic performance in terms of cycle time and other fundamental efficiency indicators for storage systems. For instance, TRSC has the potential to be applied as a retrofit solution for intermittent industrial waste low-grade heat recovery. In such an application, a lower duration of the whole storage cycle could enable the recovery and exploitation of larger amounts of waste thermal energy. Therefore, the following tasks are carried out in the thesis:

- Discussing the influence of the system's operating features, e.g., thermal masses and expander pressure ratio, on the dynamic performance in terms of cycle time (Section 5.3).
- Conducting a parametric study on the adsorption/desorption reaction times during charge and discharge phases (paragraphs 5.3.3 and 5.3.4).

2. System description

The physical and working fundamentals of sorption processes have been illustrated in the previous chapter, together with the main thermochemical sorption systems. In the following chapter a detailed description of the operation principles of the TRSC is carried out. Firstly, the working steps of the ideal cycle are defined and visualized on the Clapeyron diagram and on the T-s diagram. Subsequently, the real cycle is addressed by considering the non-equilibrium conditions required for chemisorption reactions to occur. In the last two sections, a brief description of the system components is accomplished and some potential applications for TRSC are pointed out.

2.1 TRSC

The ammonia-based thermochemical cogeneration resorption system analyzed in this work is visualized in Figure 2.1.

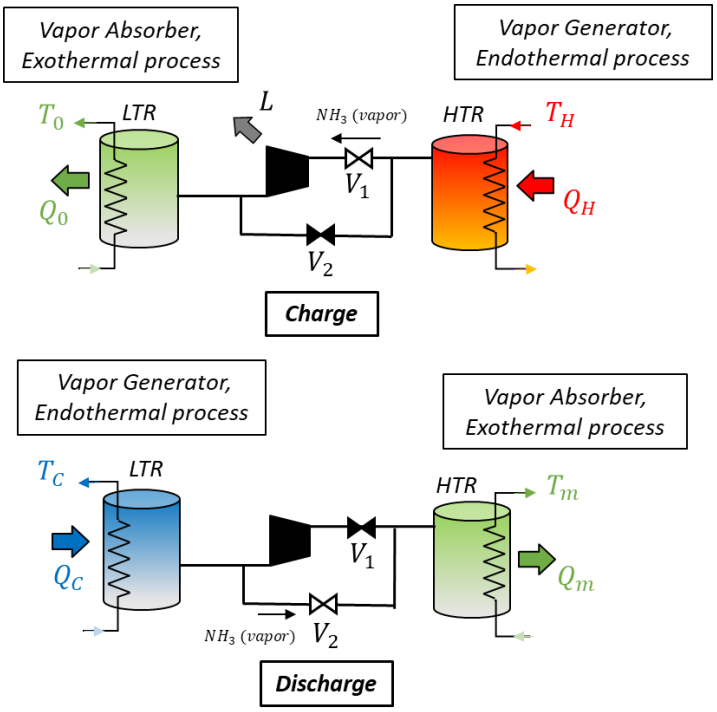

Figure 2.1: Thermochemical Resorption cycle for low-grade heat storage and cogeneration for power and cold (TRSC).

TRSC consists of a resorption cycle combined with a scroll expander, which harnesses the high pressure of the desorbed ammonia exiting the HTR during charge phase to produce mechanical work. The working steps are illustrated in detail taking as reference the ideal thermodynamic cycle of TRSC on the Clapeyron diagram (Figure 2.2). Moreover, the cycle path is represented

on a T-s diagram to differentiate between operating points with the same pressure and temperature, but different values of specific entropy of the working fluid. In particular, the equilibrium curves of HTM and LTM are represented in the adsorbed state (right curve) and desorbed state (left curve). The operating points of the cycle at which the working fluid is in the adsorbed state are indicated with an asterisk superscript on the T-s diagram. The equilibrium curves of the two solid/gas reactive mixtures have been obtained with a method proposed by Neveu [35], illustrated in Chapter 3.

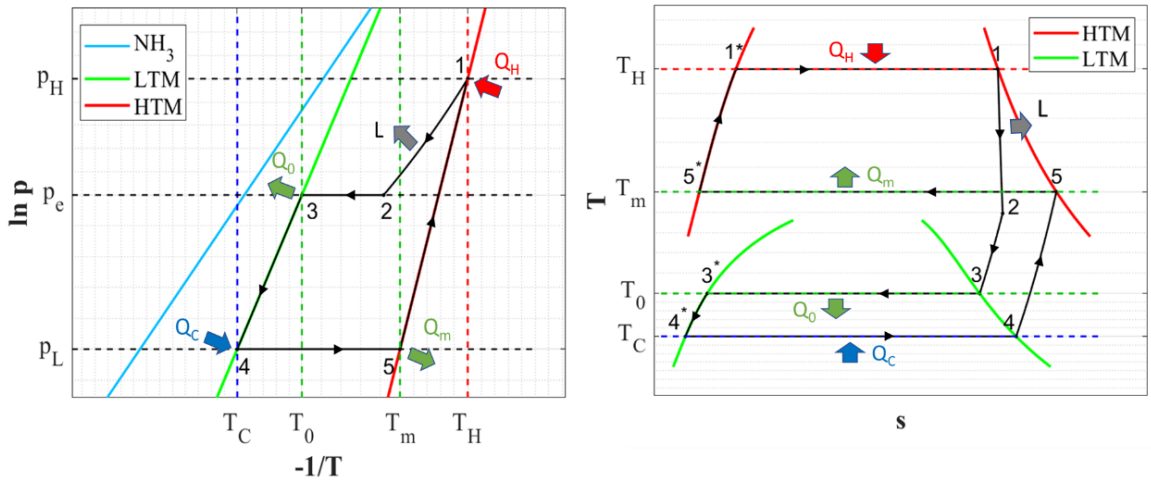

Figure 2.2: Thermodynamic path of the TRSC cycle on the Clapeyron diagram (left) and T-s diagram (right).

Besides the two main working phases of charge and discharge, the intermediate precooling and preheating steps are represented in Figure 2.2. Hence, the working steps are:

- *Charge phase:* valve V_1 is opened and valve V_2 is closed. The HTM at hot source temperature T_H is subjected to endothermal desorption (1*-1), by means of the heat input Q_H. The superheated ammonia leaves the reactor and generates work L flowing through the scroll expander (1-2). Expanded ammonia reaches thermal equilibrium with the LTR, kept at environmental sink temperature T_0 through an isobaric transformation (2-3). The ammonia is adsorbed in LTM rejecting heat Q_0 (3-3*).
- *Precool phase:* both valves are closed. The LTM in the adsorbed state is brought to cold source temperature T_C along its equilibrium line (3*-4* on T-s diagram, 3-4 on Clapeyron diagram). Note that simultaneously the HTM in the desorbed state is cooled and brought to intermediate sink temperature T_m. Such a transformation is not shown in the thermodynamic cycle because it does not involve the working fluid ammonia. The precool step is also referred to as sensible discharge phase.
- *Discharge phase*: valve V_1 is closed and valve V_2 is opened. The LTM at cold source temperature T_C undergoes endothermal decomposition providing refrigeration Q_C (4*-4). The generated ammonia bypasses the expander and flows directly towards the HTM, where it reaches thermal equilibrium (4-5). Exothermal adsorption of the refrigerant occurs and heat Q_m is rejected at intermediate sink temperature T_m (5-5*).

- *Preheat phase:* both valves are closed. The HTM in the adsorbed state is brought to hot source temperature T_H along its equilibrium line (5^*-1^* on T-s diagram, 5-1 on Clapeyron diagram). Again, also LTM in the desorbed state is heated and brought to environmental sink temperature T_0. The preheat step is also referred to as sensible charge phase.

Note that a simple resorption cycle is accomplished when the expander is bypassed during the reaction charge phase, thus valve V_1 is closed and valve V_2 is opened.

2.2 Chemisorption non-equilibrium reactions

In the description of the working principles of chemical solid/gas sorption phenomena made so far, no aspect related to the reaction kinetics were considered. Thus, the reactions of decomposition and synthesis are supposed to occur even if the thermodynamic properties of the reactive mixtures are not outside the corresponding equilibrium conditions (equilibrium lines of HTM and LTM). Nevertheless, as already mentioned in section 1.4, for a practical thermochemical solid/gas transformation it is important that the of the temperature and pressure of the reactive mixture deviate from the corresponding equilibrium line. Let us consider Figure 2.3, which shows the non-equilibrium condition to be imposed on a solid/gas reaction to activate desorption/adsorption.

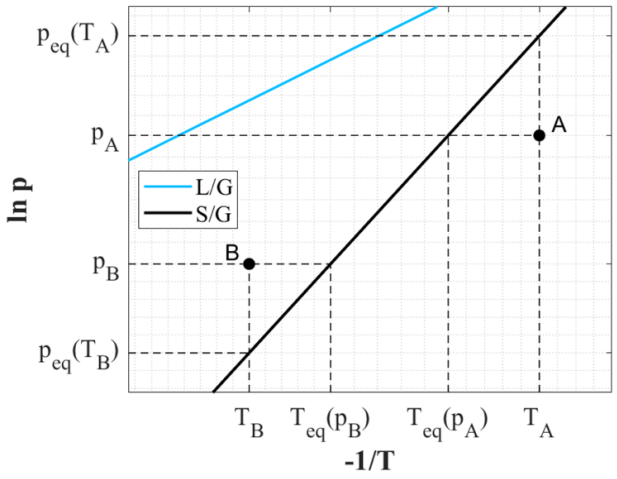

Figure 2.3: Non-equilibrium conditions imposed on the solid/gas reactive mixture (S/G). Constraint A activates desorption. Constraint B activates adsorption.

The chemical decomposition reaction is triggered if the solid/gas mixture is brought to a thermodynamic state to the right of the reaction equilibrium line (S/G), i.e. state A. Such a condition can be essentially obtained in two ways:

1. The reactive mixture is kept at pressure p_A and the temperature is increased from $T_{eq}(p_A)$ to T_A. Hence a thermal positive equilibrium deviation (or equilibrium drop) $\delta T_{eq} = T_A - T_{eq}(p_A)$ is imposed.
2. The reactive mixture is kept at temperature T_A and the pressure is decreased from $p_{eq}(T_A)$ to p_A, imposing a negative pressure equilibrium deviation $\delta p_{eq} = p_A - p_{eq}(T_A)$.

In other words, the desorption reaction is favored by high temperature and low pressure conditions with respect to the equilibrium state. On the contrary, the chemical synthesis reaction occurs when the solid/gas mixture is brought to a thermodynamic state to the left with respect to the equilibrium line (state B). Hence, adsorption is triggered when the reactive mixture is constrained by a negative thermal equilibrium deviation ($\delta T_{eq} = T_b - T_{eq}(p_B)$) or a positive pressure equilibrium drop ($\delta p_{eq} = p_b - p_{eq}(T_b)$). With respect to the equilibrium state, adsorption is favored by low temperature and high pressure conditions.

The kinetics of desorption/adsorption reactions are typically affected by two types of limitations, depending on the type of equilibrium deviation constraint [36,37]:

- When the thermal equilibrium drop is imposed, the reaction kinetics is affected mainly by heat transfer limitations. Heat transfer enhancement can be achieved by incrementing the equivalent conductivity of the reactive block.
- Imposing a pressure equilibrium deviation, the reaction kinetics is affected primarily by mass transfer limitations. Mass transfer can be improved through an increase in permeability of the reactive block.

2.2.1 Operating principles of TRSC with non-equilibrium reactions

Since proper non-equilibrium thermodynamic conditions need to be imposed to trigger decomposition/synthesis reactions, the operating principles of a simple resorption cycle in the real case are different with respect to the ideal case. An additional feature to consider in the real case is that to activate charge/discharge phase the reactive mixtures inside HTR and LTR must be brought out of the corresponding equilibrium lines simultaneously, in such a way that one reactor undergoes desorption, while the other undergoes adsorption. The operation of the real resorption system compared to the ideal cycle can be visualized in Figure 2.4. In the real case, during the intermediate steps as the reactors are disconnected, i.e. preheat phase and precool phase, the solid/gas mixtures are brought at equilibrium temperatures corresponding to different pressures. For instance, considering preheat phase, HTM is heated to temperature T_H (point **1**), while LTM is brought to temperature T_0 (point **2**), with $\boldsymbol{p_1 > p_2}$. As the valve is opened to connect the LTR and HTR, the non-equilibrium pressure p_c is imposed on both reactors, which activates the simultaneous desorption and adsorption of HTM and LTM, respectively [38].

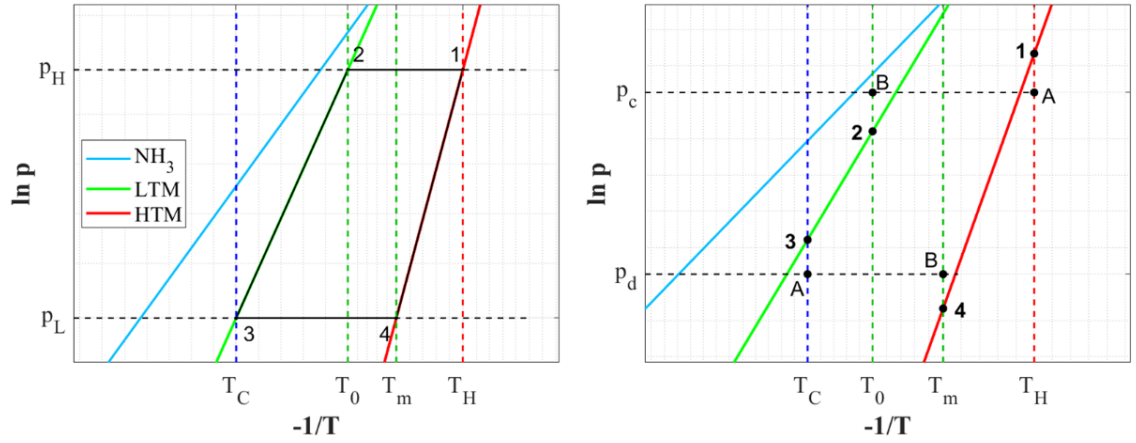

Figure 2.4: Simple resorption ideal cycle (left) compared with the operating points in the real case (right). Points A and B indicate non-equilibrium conditions which activate respectively desorption and adsorption.

Indeed, the constrain pressure p_c is lower than the equilibrium pressure of HTM at the corresponding temperature (T_H at the beginning of the reaction). In other words, a negative pressure equilibrium drop is imposed, favoring decomposition (point A). Moreover, p_c is higher than the equilibrium pressure of LTM corresponding to its temperature (initially T_0), thus adsorption is activated by means of a positive pressure equilibrium deviation (point B). Similarly, during the precool phase as the valve is closed, the reactors need to be cooled at equilibrium temperatures which allow a proper pressure difference before the discharge phase. In particular, HTM and LTM are brought to T_m (point **4**) and T_C (point **3**) respectively, with $\boldsymbol{p_3 > p_4}$. Therefore, after connecting the two reactors, the constraint pressure p_d is set, and the driving force for the decomposition of LTM and synthesis of HTM is activated. In conclusion, it can be asserted that in the real case the following additional aspects need to be considered:

- The solid/gas reactive mixtures must be brought to different equilibrium pressure levels during the preheat and precool intermediate stages.
- The pressure difference between the two reactors should guarantee the imposition of a proper non-equilibrium pressure on both reactors as they are connected. Therefore, such a constraint pressure should simultaneously ensure a negative equilibrium drop on the desorbing material and a positive equilibrium drop on the adsorbing material.

In this work, the real case of the TRSC cycle is addressed in the dynamic model, in which the kinetics of non-equilibrium decomposition/synthesis reactions is considered. Clearly, besides the practical considerations made in this paragraph regarding the simple resorption system, the effect of the scroll expander needs to be included. Hence, the TRSC cycle in the real case could be represented as in Figure 2.5. Note that the presence of the scroll expander imposing the expansion of ammonia will result in two different non-equilibrium pressure constraints $p_{c,h}$ and $p_{c,l}$, triggering HTM desorption and LTR adsorption, respectively. The dynamic model is explained in detail in the methodology chapter.

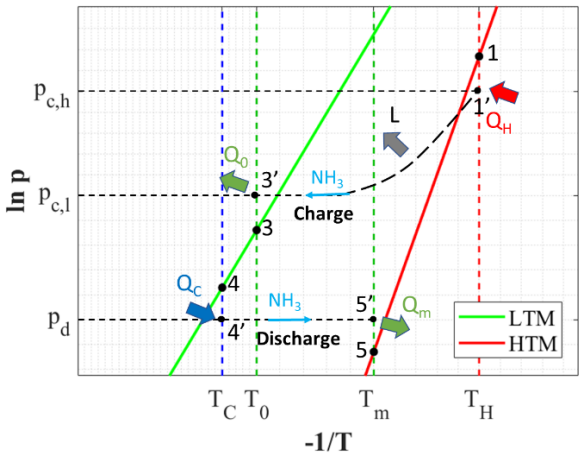

Figure 2.5: TRSC cycle in the real case. Note that two different constraint pressures are imposed during the charge phase, due to the presence of the scroll expander.

2.3 System components

The TRSC has been widely described from the point of view of the sorption phenomena and processes involved. In this section, a brief description of the single units composing the system is carried out. Therefore, typical adsorption bed technologies are presented and the working principles and features of the scroll expander are illustrated.

2.3.1 Adsorption bed

In solid/gas chemical sorption processes two main limitations affect the reaction kinetics, thus the overall cycle time: mass transfer limitations and heat transfer limitations. Adsorption beds are usually designed to maximize the overall heat transfer between the thermal energy carrier, i.e., heat transfer fluid (HTF), and reactive material. Heat transfer limitations are mainly caused by:

a) Low thermal conductivity of the adsorbent material.
b) Limited heat transfer coefficient between the adsorbent and the heat exchanger.
c) Low heat transfer coefficient of the heat transfer fluid.

To enhance the heat transfer between adsorbent and heat exchanger (b), a possible approach is to increase the heat exchange area. Two types of adsorption beds commonly fulfill the requirement of high heat exchange area, i.e., plate-fin and shell-tube types.

- **Plate-fin type** (Figure 2.6).
  It is composed by several plate-fin heat exchanger units. Fins can be installed on both the fluid side and on the adsorbent side to maximize the heat transfer area. On the adsorbent side, channels ensure the diffusion of the decomposed adsorbate which flows in the depth direction, perpendicular to the thermal fluid flow direction. Fins have pores

which enhance the mass transfer on the adsorbent side. On the thermal fluid side, the pores in the fins favor turbulence, which enhances the heat transfer (reducing limitation c).

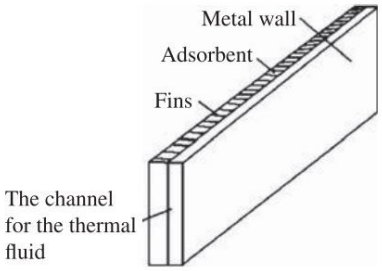

Figure 2.6: Plate-fin heat exchanger unit of adsorption bed [14].

- **Shell-tube type** (Figure 2.7).
  Shell-and-tube is a more suitable type of reactor for high pressure applications, e.g., using ammonia as a refrigerant. Indeed, thanks to its high resistance to structural and thermal stresses, shell-tube reactors are less subjected to leakage phenomena. The heat transfer medium is on the shell side, while the solid adsorbent is in metal tubes. Fins can be installed on the sorbent side in the tubes to enhance heat transfer. During synthesis/decomposition, the gaseous refrigerant flows through proper microchannels in the adsorbent tubes.

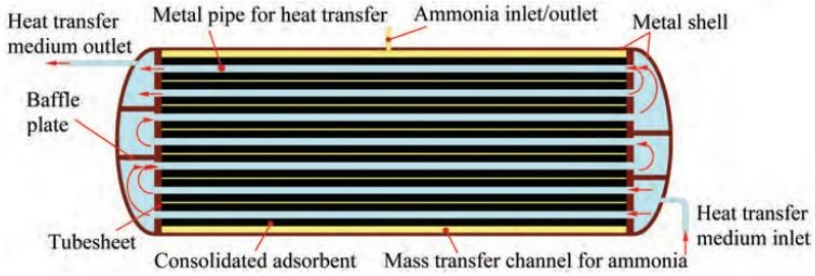

Figure 2.7: Shell-tube adsorption bed [22].

To reduce the heat transfer limitation due to the low thermal conductivity of the adsorbent (limitation a), one typical strategy is to formulate a composite adsorbent. In such materials, the pure adsorbent is combined with a so-called host matrix, usually characterized by high thermal conductivity, which contributes to the decrease of total thermal resistance on the reactive medium side [14]. Expanded natural graphite (ENG) is acknowledged to be one of the best materials to be used as a host matrix. In fact, not only the ENG/adsorbent complex reveals enhanced heat transfer, compared to the pure adsorbend, but it also results in improved mass transfer performance [39].

2.3.2 Scroll expander

In power generation cycles, two categories of expansion machines are commonly used: velocity type turbines and volumetric devices. Scroll expanders belong to the latter category; they are composed of two displaced spiral scrolls (Figure 2.8). One scroll is fixed while the other is free to move with rigid orbiting progressions around the center of the spiral. The gaseous working fluid flowing at high pressure at the center of the device inlet (admission) causes the mobile scroll to orbit with an anticlockwise movement. Such movement allows the gas to flow in the larger volume vanes of the expander, resulting in a progressive pressure decrease until the outlet is reached (discharge). A clockwise orbiting movement of the mobile scroll would produce the reverse effect with the device operating as a compressor.

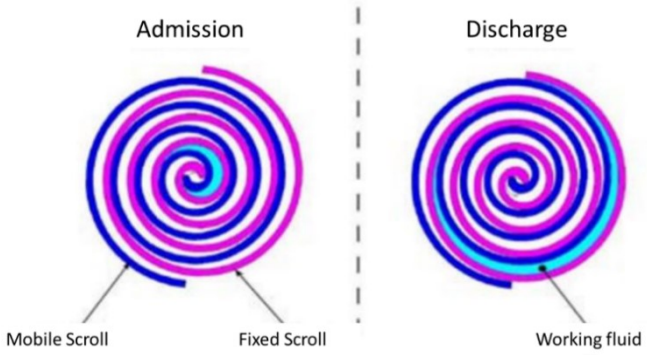

Figure 2.8: Scroll expander expansion process [40].

Compared to velocity turbines, volumetric expanders are characterized by lower flow rates, lower rotational speed, higher pressure ratio and are usually more feasible for small-sized power generation systems (< 50 kW) [41]. A beneficial feature of volumetric expanders is the major tolerance to liquid droplets, hence potentially working fluids can be expanded until they are slightly wet at the outlet. Compared to other volumetric devices, scroll expanders have several advantages such as high efficiency and high pressure ratio, low vibrations, low manufacturing cost, and high reliability [42].

2.4 Potential Applications

In the following section, two potential low-grade heat applications for TRSC are presented. A first scenario is the industrial sector, in which TRSC could be integrated as a retrofit solution in a specific process for waste heat recovery and other multiple functions, such as cooling and heating. Another potential application presented for TRSC is in the building space/heating sector, where it is integrated as a storage system in a solar thermal circuit, enabling a higher share of renewables in the yearly energy consumption.

2.4.1 Waste heat recovery

Let us consider an industrial plant which rejects several streams of waste thermal energy at different temperatures in the low-grade range with high refrigeration and heating needs during specific periods. The TRSC could be retrofitted to the already existing process storing intermittently waste heat Q_H during charge phase and producing diverse useful effects depending on the specific requirements during discharge phase (Figure 2.9):

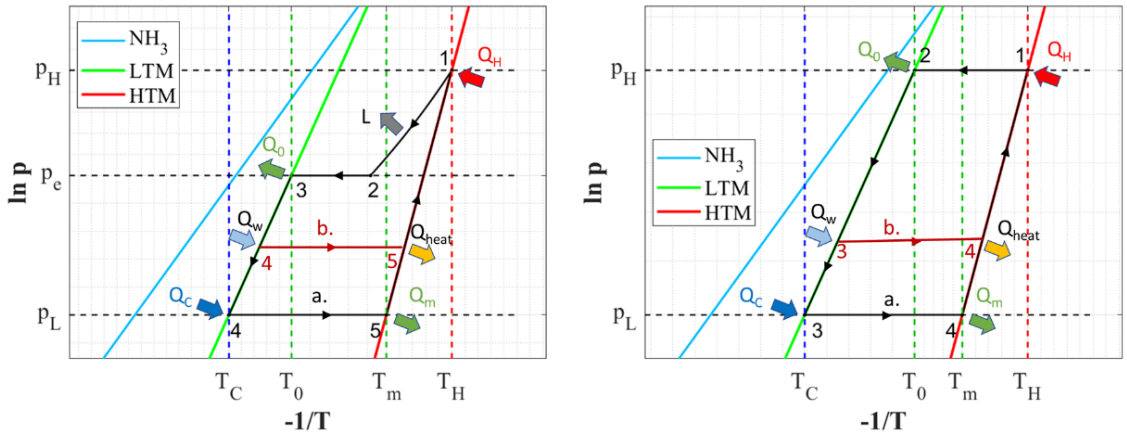

Figure 2.9: TRSC application for waste heat recovery in the case of cold production (a.) and heating (b.), with power production (left) and without power production (left).

a. When cold production is needed, the heat transfer fluid to be cooled flows in the LTR undergoing refrigeration effect Q_C, while the thermal energy Q_m related to HTM adsorption is released to the environment or to another stream in the process. It is important to notice that before the discharge phase, the LTR must be precooled to the desired refrigeration temperature. Hence, a pre-existent cold stream or back-up refrigeration cycle to achieve the precool stage should be addressed during the design of retrofit TRSC.
b. If heating is needed and the temperature of the available waste streams is too low, the waste heat Q_w of such streams can be used to trigger desorption in LTR. The gaseous ammonia is adsorbed in HTR and the thermal energy Q_{heat} provides useful heating. The quality of the heat depends on the temperature of the waste heat related to the available streams.

Note that in both cases, the expander produces mechanical power during the charge phase, which can feed a generator producing electricity to be used or sold to the grid. However, when power is not required, the expander can be bypassed to obtain the simple resorption configuration (Figure 2.9 right graph). Finally, TRSC can operate also with the function of energy upgrade, storing low-grade heat during the charge phase, producing high-grade thermal energy during discharge. In such a configuration, production of power is feasible only if during the charge phase the properties of solid/ammonia reaction combined with the temperature thermal input result in the production of gaseous ammonia at a sufficiently high pressure.

2.4.2 Solar thermal application

The TRSC could provide relevant advantages if integrated into a solar thermal loop for hot water production and space heating/cooling. For instance, in periods of low hot water demand, e.g. in summer, the excess solar thermal energy Q_H could be stored during the charge phase, causing ammonia desorption at the HTR, while the LTR kept at thermal equilibrium with the environment would undergo adsorption. During the discharge phase relevant useful effects can be obtained, e.g., as represented in Figure 2.10:

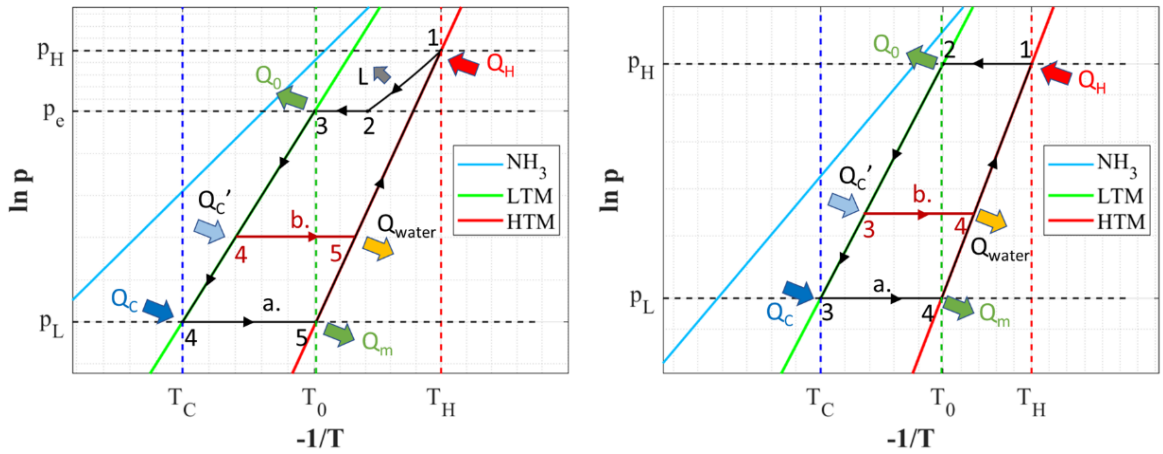

Figure 2.10: TRSC application in a solar thermal circuit in the case of pure refrigeration (a.) and simultaneous refrigeration and hot water production (b.). Power production (left) and no power production (right). Note that the environment acts as thermal sink during both charge and discharge phases.

a. *Pure refrigeration*. The HTR is brought to thermal equilibrium with the environment during the precool step, while LTR is cooled to refrigeration temperature T_C. When the refrigeration effect is required Q_C, the reactors are connected, and reaction discharge is achieved. The adsorption heat coming from HTM is rejected at environmental temperature T_0. Hence, the environment is used as a thermal sink for adsorption heat both during charge and discharge phases.
b. *Refrigeration and hot water production*. The HTR is brought to the desired hot water temperature, during the precool step, while LTR is cooled to refrigeration temperature. As the discharge phase is activated simultaneous refrigeration Q_C' and hot water production Q_{water} are achieved, due to LTR endothermal desorption and HTR exothermal adsorption, respectively. Note that the refrigeration effect is at higher temperature, thus lower quality, with respect to the pure refrigeration case.

In both configurations, power production is achieved during the charge phase, and the generated electricity can be directly used or sold to the grid. As in the previous scenario, if power is not needed, the expander can be easily bypassed by properly controlling the valve connections between the reactors, thus obtaining a simple resorption configuration.

TRSC solar thermal application would allow obtaining higher solar yield in the overall energy consumption related to refrigeration and sanitary water production in hot periods. Based on the

operating and required temperatures, it is important to select proper solid/gas reactions (LTM and HTM) in order to assure the exploitation of the environmental sink at temperature T_0 both in charge and discharge phases (case a.), and to allow the simultaneous production of cold and heat when needed (case b.).
Thanks to high energy density and low thermal losses of thermochemical storage systems, TRSC could be applied in solar thermal applications for space heating in buildings, also with seasonal storage function. The working cycle would be structured as follows: during summer, the solar thermal energy is stored in the system and the expander produces power or is bypassed, depending on the needs during the whole charging period. When TRSC is completely charged the reactors are disconnected and the precool phase begins: during winter, LTR reaches thermal equilibrium with the cold external environment, while HTR is kept at building temperature. As space heating is required, the two reactors are connected, and discharge phase is triggered. Hence, the cold thermal energy provided by the environmental source drives LTM desorption, while the heat supplied by the adsorbing HTM provides the heating effect. Since large amounts of energy to be charged and discharged are expected for a seasonal application of TRSC, the system size would be larger with respect to the previous case illustrated in the solar thermal field, which is instead supposed to operate intermittently.

The above presented applications of TRSC for low-grade heat exploitation, recovered from industrial waste heat or in solar thermal systems, represent only some examples among a broad range of possibilities. Indeed, it can be inferred that such a technology based on thermochemical resorption is highly flexible, allowing to design smart systems, capable of varying operating configurations, depending on the specific needs. However, regardless of the type of application, a proper thermo-economic analysis should be carried out to determine if this kind of technology is relevant in terms of overall savings. In other words, the total cost needed to implement and maintain the system should not overcome the benefits in terms of revenues related to refrigeration, heating, and work production in the long term.

3. Methodology

The following chapter aims to illustrate the methods adopted to build the general models for the TRSC. In the first part, the assumptions and equations for the development of the thermodynamic cycle are presented. Subsequently, the model for the sized system in the steady state case is obtained by including the effective materials and thermal masses of the reactors. Finally, a detailed description of the dynamic lumped parameters model used to investigate the sized system is carried out. For both steady state and dynamic state models, a validation based on data found in the literature is proposed.

3.1 Thermodynamic cycle

The thermodynamic cycle of TRSC represents the basis on which the steady state model for the sized system is built. Since the implementation of the thermodynamic cycle of TRSC is based on solid/gas adsorption theory, briefly introduced in section 1.4, such working principles are recalled and described more in detail in the following section. Afterward, the Neveu method adopted to represent the cycle on the T-s diagram is illustrated.

3.1.1 Solid/ammonia chemisorption reactions

As introduced in paragraph 1.4, reversible solid/gas adsorption phenomena can be defined with the general reaction notation:

$$S_1 + G \rightleftarrows S_2 + \Delta H_r \tag{3.1}$$

The reaction evolving towards the right is exothermal adsorption (or sorption), while the reaction towards the left is endothermal desorption. The TRSC exploits the reaction enthalpy ΔH_r of solid/gas chemisorption reactions, in which the working fluid is ammonia. Thus equation 3.1 can be generalized for ammonia sorption as follows:

$$S(NH_3)_{\nu_1} + (\nu_2 - \nu_1)NH_3 \rightleftarrows S(NH_3)_{\nu_2} + (\nu_2 - \nu_1)\Delta\bar{h}_r \tag{3.2}$$

Where the first term in the left-hand side of the reaction is the solid S_1, composed of a substance S at the low ammoniation state defined by coefficient ν_1. When the substance S_1 adsorbs the quantity of ammonia $(\nu_2 - \nu_1)NH_3$, the complex S_2 consisting of the substance S at the high ammoniation state ν_2 is obtained and the reaction heat represented by the second term on the right-hand side of the reaction is released. The general solid/ammonia reaction in equation 3.2 is identified from now on with the notation $S\,(\nu_2 - \nu_1)$. Quantities referring to solid ammoniated at higher and lower states (S_2 and S_1) will have the subscripts S_2 and S_1 respectively, while subscript s indicates a variable related to the pure solid S. The equilibrium

of a solid/gas reaction is described by the Clapeyron equation (equation 3.3), based on the following hypothesis:

- The heat and entropy of reaction are constant with respect to the temperature and equal to $\Delta\bar{h}_r^0$ and $\Delta\bar{s}_r^0$, evaluated at standard reference conditions.
- The molar volume of the solid phase is negligible compared to the volume occupied by the gaseous phase.
- The gas is modeled as an ideal gas.

The Clapeyron equation can be written in two equivalent forms:

$$ln\left(\frac{p_{eq}}{p_0}\right) = -\frac{\Delta\bar{h}_r^0}{RT_{eq}} + \frac{\Delta\bar{s}_r^0}{R} \quad or \quad ln(p_{eq}) = -\frac{\Delta\bar{h}_r}{RT_{eq}} + \frac{\Delta\bar{s}_r}{R} \tag{3.3}$$

where $\Delta\bar{h}_r$ and $\Delta\bar{s}_r$ are molar enthalpy and entropy of reaction of the considered solid/gas reaction related to the reference pressure of 1 Pa. It can be inferred that:

$$\Delta\bar{h}_r = \Delta\bar{h}_r^0; \quad \Delta\bar{s}_r = \Delta\bar{s}_r^0 + Rln(p_0) \tag{3.4}$$

As an example, let us consider the reaction manganese chloride – NH_3 already introduced in section 1.4 :

$$MnCl_2(NH_3)_2 + 4NH_3 \rightleftarrows MnCl_2(NH_3)_6 + 4\,\Delta\bar{h}_{r,MnCl_2(6-2)} \tag{3.5}$$

Such a reaction is indicated as $MnCl_2$ 6-2. From equation 3.4, the molar enthalpy and entropy of reaction with respect to reference pressure of 1 Pa associated to $MnCl_2$ 6-2 result respectively $\Delta\bar{h}_r$ =47.42 kJ/mol and $\Delta\bar{s}_r$ =228.07 J/mol/K.

To evaluate the extent of a sorption reaction the global conversion rate x is defined as follows:

$$x = \frac{quantity\ of\ ammonia\ adsorbed}{total\ quantity\ of\ ammonia\ that\ can\ be\ adsorbed} \tag{3.6}$$

$$x = \frac{m_{NH_3}}{m_{NH_3,tot}} = \frac{n_{NH_3}}{n_{NH_3,tot}} \tag{3.7}$$

Where $n_{NH_3,tot}$ is the stoichiometric number of moles of ammonia associated to the considered reaction:

$$n_{NH_3,tot} = (\nu_2 - \nu_1)n_{S_2} = (\nu_2 - \nu_1)n_{S_1} \tag{3.8}$$

Therefore, the parameter *x* ranges between 0 and 1. and such extreme values correspond to the completed desorbed and adsorbed states, respectively.

3.1.2 The Neveu method

Based on the monovariant characteristic of the equilibrium of chemisorption processes and the dualism with the liquid-vapor phase equilibrium, Neveu et al. [35] proposed a method to calculate the specific enthalpy and entropy of the ammonia in the adsorbed phase. According to such an approach, the specific enthalpy and entropy of ammonia at adsorbed state are defined as follows:

$$h^* = h(T, p_{eq}) - r_{p,T}(T) \tag{3.9}$$

$$s^* = s(T, p_{eq}) - \frac{r_{p,T}(T)}{T} \tag{3.10}$$

Where $h(T, p_{eq})$ and $s(T, p_{eq})$ are respectively the enthalpy and entropy of gaseous ammonia at temperature T and equilibrium pressure p_{eq}. The term $r_{p,T}(T)$ is the heat of reaction at fixed pressure and temperature, which is a function of the considered temperature T. It is obtained starting from the Clapeyron equation for a solid/gas reaction in its general form:

$$\left(\frac{dp}{dT}\right)_{eq} = \frac{r_{p,T}}{T(v + v_{S_1} - v_{S_2})} \tag{3.11}$$

Where v is the gas specific volume at temperature T and equilibrium pressure p_{eq}. Defining Δv_s as the specific volume variation between the high-ammoniated solid and low-ammoniated solid, we can write:

$$r_{p,T}(T) = \left(\frac{dp}{dT}\right)_{eq} T(v - \Delta v_S) \tag{3.12}$$

The first term on the right-hand side of the above equation can be obtained by rewriting the Clapeyron equation (3.3) in exponential form and deriving the obtained expression with respect to temperature:

$$\left(\frac{dp}{dT}\right)_{eq} = \frac{\Delta \bar{h}_r^0}{RT^2} p_0 \, exp\left(-\frac{\Delta \bar{h}_r^0}{RT} + \frac{\Delta \bar{s}_r^0}{R}\right) \tag{3.13}$$

Substituting in equation 3.12:

$$r_{p,T}(T) = \frac{\Delta \bar{h}_r^0}{RT^2} p_0 \, exp\left(-\frac{\Delta \bar{h}_r^0}{RT} + \frac{\Delta \bar{s}_r^0}{R}\right)(v - \Delta v_S) \tag{3.14}$$

The value of Δv_S should be experimentally measured for each solid/gas reaction considered. However, as experimental values are not available, the value of molar volume variation between

solids at high and low ammoniation states $\Delta\bar{v}_S$ can be assumed constant and equal to 20 cm^3/mol, as suggested by Neveu. Thus, for each solid/gas reaction evaluated in this work:

$$\Delta v_S = \frac{20}{\bar{M}_{NH_3}} \simeq 11.76 \cdot 10^{-4} \frac{m^3}{kg} \tag{3.15}$$

In Figure 3.1 the equilibrium lines of $MnCl_2$ 6-2 reaction are represented on a Clapeyron diagram and on T-s diagram, together with the liquid/gas ammonia saturation curve.

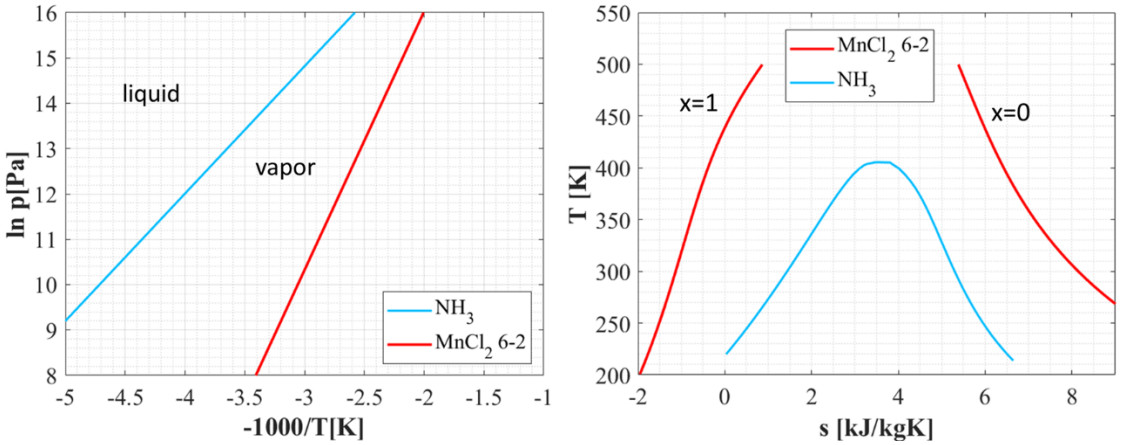

Figure 3.1: Clapeyron diagram (left) and T-s diagram (right) related to reaction $MnCl_2$ 6-2 and to the ammonia saturation line. On the T-s diagram the left red line represents the adsorbed state of the reactive mixture, the right red line is the desorbed state.

One of the advantages of the Neveu method is the possibility of representing the adsorption and desorption processes as thermodynamic transformations on T-s or Mollier diagrams, widely used in the power and refrigeration field. Moreover, such an approach overcomes the hypothesis of constant variation of enthalpy and entropy with respect to temperature during adsorption/desorption, related to the Clapeyron equation.

3.1.3 Cycle implementation

The thermodynamic cycle was implemented on EES (Engineering Equation Solver), a software capable of solving any set of implicit equations. Moreover, it contains a database of thermodynamic properties for several working fluids, meaning that relevant quantities, such as specific enthalpy or temperature, can be obtained by simply calling functions in the code. Let us recall the thermodynamic cycle of TRSC, represented in Figure 3.2 on the Clapeyron diagram and on the T-s diagram.

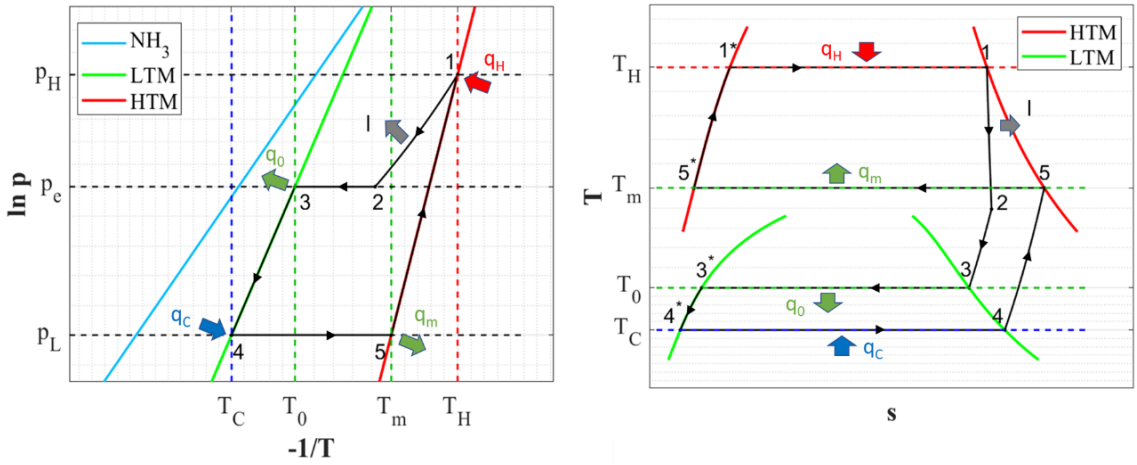

Figure 3.2; Thermodynamic cycle of the TRSC on the Clapeyron diagram (left) and T-s diagram (right).

Firstly, the Clapeyron equilibrium equations are set to fix the relation between temperature and pressure of the considered solid/ammonia reactions:

$$p_j = exp\left(-\frac{\Delta\bar{h}_{r,h}}{RT_j} + \frac{\Delta\bar{s}_{r,h}}{R}\right); \quad j = 1,5 \tag{3.16}$$

$$p_j = exp\left(-\frac{\Delta\bar{h}_{r,l}}{RT_j} + \frac{\Delta\bar{s}_{r,l}}{R}\right); \quad j = 3,4 \tag{3.17}$$

The index j refers to a generic point of the thermodynamic cycle in the Clapeyron diagram, which is on the equilibrium lines of HTM or LTM, indicated respectively by the subscripts h and l. The expansion is modeled with the following set of equations:

$$\eta_{is} = \frac{h_1 - h_2}{h_1 - h_{2,is}} \tag{3.18}$$

$$\frac{T_1}{T_{2,is}} = \beta^{\frac{\gamma-1}{\gamma}} \tag{3.19}$$

$$\beta = \frac{p_1}{p_2} \tag{3.20}$$

$$h_{2,is} = enthalpy(T_{2,is}, s_2) \tag{3.21}$$

$$s_2 = s_1 \tag{3.22}$$

Where η_{is} is the isentropic efficiency of the expander while h is the specific enthalpy of ammonia. The assumption of ideal gas is made for the adiabatic expansion (equation 3.19), with a constant specific heat ratio $\gamma = 1.31$. The right-hand side of Equation 3.21 represents the function called on EES to obtain the specific enthalpy corresponding to temperature $T_{2,is}$ and entropy s_2. In general, thermodynamic quantities can be obtained on EES by writing the functions related to them, corresponding to two independent variables. For instance, the remaining equations to close the thermodynamic cycle are:

$$h_2 = enthalpy(T_2, p_2) \tag{3.23}$$

$$v_2 = volume(T_2, p_2) \tag{3.24}$$

$$h_j = enthalpy(T_j, p_j) \tag{3.25}$$

$$s_j = entropy(T_j, p_j) \tag{3.26}$$

$$v_j = volume(T_j, p_j) \tag{3.27}$$

The equations written so far are sufficient to obtain the thermodynamic cycle on the Clapeyron diagram. Since $\Delta\bar{h}_r$ and $\Delta\bar{s}_r$ of the considered HTM and LTM are known, the number of equations is 23 with 27 unknowns. Proper equations can be added in different ways to have a solvable system with the number of unknown variables equal to the number of equations. For instance, one possible way is to add four equations defining the values of η_{is}, β, T_1 and T_4. To distinguish between cycle points in adsorbed and desorbed state, specific enthalpy and entropy are computed through the Neveu equations (3.9 and 3.10):

$for\ j = 1, 5$

$$h_j^* = h_j - \frac{\Delta\bar{h}_{r,h}}{RT_j} exp\left(-\frac{\Delta\bar{h}_{r,h}}{RT_j} + \frac{\Delta\bar{s}_{r,h}}{R}\right)(v_j - \Delta v_S); \tag{3.28}$$

$$s_j^* = s_j - \frac{\Delta\bar{h}_{r,h}}{RT_j^2} exp\left(-\frac{\Delta\bar{h}_{r,h}}{RT_j} + \frac{\Delta\bar{s}_{r,h}}{R}\right)(v_j - \Delta v_S) \tag{3.29}$$

$for\ j = 3, 4$

$$h_j^* = h_j - \frac{\Delta\bar{h}_{r,l}}{RT_j} \exp\left(-\frac{\Delta\bar{h}_{r,l}}{RT_j} + \frac{\Delta\bar{s}_{r,l}}{R}\right)(v_j - \Delta v_S) \tag{3.30}$$

$$s_j^* = s_j - \frac{\Delta\bar{h}_{r,l}}{RT_j^2}\exp\left(-\frac{\Delta\bar{h}_{r,l}}{RT_j} + \frac{\Delta\bar{s}_{r,l}}{R}\right)(v_j - \Delta v_S) \quad 3.31$$

3.1.4 Energy equations

Once the points of thermodynamic cycle are determined, it is possible to evaluate the energy transferred by the working fluid in terms of specific enthalpy variations, by applying the first law balance. To do so, let us define the following specific energy variables in J/kg:

- q_H: overall specific thermal energy to be stored.
- q_0: overall specific thermal energy released to the ambient sink.
- q_C: overall specific cold production.
- q_m: overall specific thermal energy released to the intermediate temperature sink.
- l: specific work output.

Each of the specific thermal energy terms is the sum of a sensible heat term and a reaction heat term:

$$q_H = q_{H,sen} + q_{H,r} \Rightarrow q_{H,sen} = h_1^* - h_5^*; \quad q_{H,r} = h_1 - h_1^* \quad 3.32$$

$$q_0 = q_{0,sen} + q_{0,r} \Rightarrow q_{0,sen} = h_3 - h_2; \quad q_{0,r} = h_3^* - h_3 \quad 3.33$$

$$q_C = q_{C,sen} + q_{C,r} \Rightarrow q_{C,sen} = h_4^* - h_3^*; \quad q_{C,r} = h_4 - h_4^* \quad 3.34$$

$$q_m = q_{m,sen} + q_{m,r} \Rightarrow q_{m,sen} = h_5 - h_4; \quad q_{m,r} = h_5^* - h_5 \quad 3.35$$

From the above equations, it can be inferred that not all the energy to be stored is converted into heat of reaction $q_{H,r}$. Instead, part of it is used as sensible heat to bring the HTM in thermal equilibrium with the hot source at temperature T_H. On the other hand, the net cold production is lower than the total heat of reaction $q_{C,r}$, related to the LTM: since the adsorbed working fluid needs to be cooled to the cold source temperature, this results in a negative contribution to the overall refrigeration effect. In other words, a part of the gross cooling potential $q_{C,r}$ is used to bring the adsorbed ammonia in thermal equilibrium with the cold source at temperature T_C. To close the cycle, the equation for the specific work is set:

$$l = h_1 - h_2 \quad 3.36$$

Based on the thermodynamic cycle and on the specific energy transferred, the working steps of TRSC can be summarized as follows (Figure 3.3):

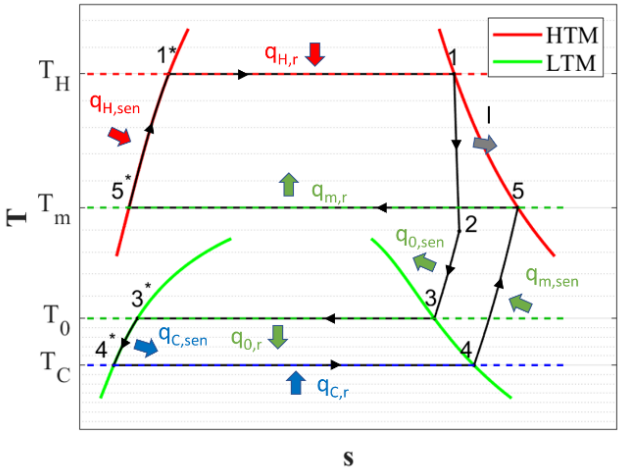

Figure 3.3: Thermodynamic cycle of TRSC on the T-s diagram, showing sensible heat and reaction heat contributions.

- *Preheat phase (sensible charge step):* the working fluid ammonia adsorbed in HTM is preheated to the hot source temperature T_H through the sensible heat input $q_{H,sen}$.
- *Reaction charge phase:* reaction heat $q_{H,r}$ is absorbed by HTM and the working fluid undergoes desorption flowing through the scroll expander and producing specific work l. The ammonia reaches thermal equilibrium with LTM through the sensible heat $q_{0,sen}$ and is then adsorbed releasing $q_{0,r}$ at environmental sink temperature T_0.
- *Precool phase (sensible discharge step):* the ammonia adsorbed in LTM is precooled to the cold source temperature T_C, releasing sensible heat input $q_{C,sen}$.
- *Reaction discharge phase:* reaction heat $q_{C,r}$ is supplied to LTM and working fluid undergoes desorption flowing towards the HTM. The working fluid reaches thermal equilibrium with HTM through the sensible heat $q_{m,sen}$ and is then adsorbed releasing $q_{m,r}$ at intermediate sink temperature T_m.

Relevant performance parameters can be computed, as a function of the application purpose of the system. In the case of cold and power production, the ideal first and second law efficiencies are defined as follows:

$$\eta_{I,id} = \frac{l + q_C}{q_H} \tag{3.37}$$

$$\eta_{II,id} = \frac{l + e_C}{e_H} \tag{3.38}$$

Where e_H and e_C are the specific exergy flows associated to the stored heat and to the cold production respectively:

$$e_H = q_H \left(1 - \frac{T_0}{T_H}\right) \quad 3.39$$

$$e_C = q_C \left(\frac{T_0}{T_C} - 1\right) \quad 3.40$$

3.2 System steady state (sizing)

After the thermodynamic cycle has been implemented, proper equations have been added to include the effects related to the amounts of the various materials composing the reactors. Indeed, the pure thermodynamic cycle only allows to carry out an intensive evaluation of the TRSC, useful to estimate its intrinsic performance. Nevertheless, more realistic estimation can be achieved by considering the effective size and thermal masses of the system. Therefore, proper variables and equations have been defined to encompass the following materials:

- The total quantity of ammonia that can be exchanged between the reactors. In the steady state case, it is assumed that the HTR and the LTR are always in the complete adsorbed or desorbed states.
- The solid reactive material ammoniated at a lower or higher state in both reactors.
- The expanded natural graphite (ENG), which is assumed to be mixed with solid reactive material in the reactors to increase the thermal conductivity of the reactive block (paragraph 2.3.1).
- The metal which composes the heat exchanger in both reactors.

The equation for the total amount of ammonia that can be exchanged by a single reactor is:

$$m_{NH_3,tot} = \bar{M}_{NH_3}(\nu_2 - \nu_1)n_{S_2} = \bar{M}_{NH_3}(\nu_2 - \nu_1)n_{S_1} \quad 3.41$$

Where $\bar{M}_{NH_3}$ is the molar mass of ammonia, equal to 0.017 kg/mol. The following equations are set to link the quantities of pure solid and sorbent ammoniated at high and lower states:

$$n_s = n_{S_1} = n_{S_2} \quad 3.42$$

$$m_s = \bar{M}_s n_s \quad 3.43$$

$$m_{S_2} = \bar{M}_{S_2} n_{S_2} = (\bar{M}_s + \nu_2 \bar{M}_{NH_3}) n_{S_2} \quad 3.44$$

$$m_{S_1} = \bar{M}_{S_1} n_{S_1} = (\bar{M}_s + \nu_1 \bar{M}_{NH_3}) n_{S_1} \quad 3.45$$

Where $\bar{M}_s$ is the molar mass of the considered pure solid. For instance, in the case of reaction $MnCl_2$ 6-2, $\bar{M}_s$ is the molar mass of $MnCl_2$ while $\bar{M}_{S_2}$ is the molar mass of $MnCl_2(NH_3)_6$. The amounts of graphite and metal are added by introducing two parameters, i.e. the graphite ratio f_{EG} and metal ratio τ, defined as follows:

$$f_{EG} = \frac{m_{EG}}{m_s + m_{EG}} \tag{3.46}$$

$$\tau = \frac{m_{HX}}{m_s} \tag{3.47}$$

Figure 3.4 summarizes the variables defining the different materials inside the two reactors, HTR and LTR.

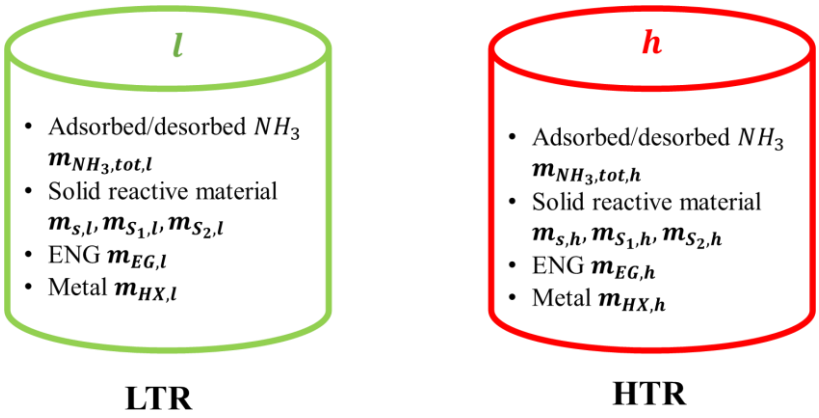

Figure 3.4: Material composition of LTR and HTR.

It is important to notice that the equations from 3.41 to 3.47 are set for both reactors. An additional equation is implemented to achieve properly sized reactors:

$$m_{NH_3,tot,l} = m_{NH_3,tot,h} = m_{NH_3,tot} \tag{3.48}$$

With such a constrain, the reactors are dimensioned to exchange the same amount of stoichiometric working fluid. As a result, equation 3.48 prevents the system from being oversized or undersized.

3.2.1 Thermal masses

The thermal masses of the reactors are defined based on whether they are in adsorbed ($x = 1$) or desorbed ($x = 0$) state:

$$x = 1 \Rightarrow \quad TM_{S_2} = (m_{S_2} c_{S_2} + m_{HX} c_{HX} + m_{EG} c_{EG}) \tag{3.49}$$

$$x = 0 \;\Rightarrow\; TM_{S_1} = (m_{S_1} c_{S_1} + m_{HX} c_{HX} + m_{EG} c_{EG}) \tag{3.50}$$

Where c is the specific heat of the considered material. For the reactive solid at high and low ammoniation states the specific heat is defined as follows:

$$c_{S_2} = \frac{\bar{c}_{S_2}}{\bar{M}_{S_2}} = \frac{\bar{c}_s + \nu_2 \bar{c}_{NH_3}}{\bar{M}_{S_2}} \tag{3.51}$$

$$c_{S_1} = \frac{\bar{c}_{S_1}}{\bar{M}_{S_1}} = \frac{\bar{c}_s + \nu_1 \bar{c}_{NH_3}}{\bar{M}_{S_1}} \tag{3.52}$$

Once the amounts of materials adopted in the reactors and the related thermal masses are defined, the energy quantities exchanged within the cycle are computed:

$$Q_H = Q_{H,sen} + Q_{H,r} = TM_{S_2,h}(T_1 - T_5) + m_{NH_3,tot}(h_1 - h_1^*) \tag{3.53}$$

$$Q_0 = Q_{0,sen} + Q_{0,r} = \; m_{NH_3,tot}(h_3 - h_2) + m_{NH_3,tot}(h_3^* - h_3) \tag{3.54}$$

$$Q_C = Q_{C,sen} + Q_{C,r} = TM_{S_2,l}(T_4 - T_3) + m_{NH_3,tot}(h_4 - h_4^*) \tag{3.55}$$

$$Q_m = Q_{m,sen} + Q_{m,r} = \; m_{NH_3,tot}(h_5 - h_4) + m_{NH_3,tot}(h_5^* - h_5) \tag{3.56}$$

$$L = m_{NH_3,tot}(h_1 - h_2) \tag{3.57}$$

It is noteworthy that the thermal masses of the reactors affect only the sensible heat contributions relative to the stored heat $Q_{H,sen}$ and the cold production $Q_{C,sen}$. Indeed, the sensible terms $Q_{0,sen}$ and $Q_{m,sen}$ are related to pure ammonia flows, which are brought to thermal equilibrium with environmental sink and intermediate sink, respectively. The exergy quantities corresponding to the refrigeration effect and the stored heat are also defined:

$$E_C = Q_C \left(\frac{T_0}{T_C} - 1\right) \tag{3.58}$$

$$E_H = Q_H \left(1 - \frac{T_0}{T_H}\right) \tag{3.59}$$

3.2.2 System total size

The total size of the system is defined in terms of the mass and volume of the two reactors, while the dimensions of the scroll expander and auxiliary equipment are neglected. Concerning the system mass, the following equations are set:

$$m_{tot} = m_{tot,h} + m_{tot,l} \tag{3.60}$$

$$m_{tot,h} = m_{S_2,h} + m_{EG,h} + m_{HX,h} \tag{3.61}$$

$$m_{tot,l} = m_{S_1,l} + m_{EG,l} + m_{HX,l} \tag{3.62}$$

The masses of the two reactors are summed considering the HTR as in the complete adsorbed state, while the LTR in the complete desorbed state. An equivalent result could be obtained by combining the masses of the two reactors in the desorbed state with the total amount of ammonia exchanged between them. Regarding the system volume, the equations are:

$$V_{tot} = V_{tot,l} + V_{tot,l} \tag{3.63}$$

$$V_{tot,h} = V_{S_2,h} + V_{EG,h} + V_{HX,h} \tag{3.64}$$

$$V_{tot,l} = V_{S_2,l} + V_{EG,l} + V_{HX,l} \tag{3.65}$$

In this case both reactors are considered in the adsorbed state, in which the volume occupied by the materials is maximum. For each reactor, the volumes of graphite and metal are computed as follows:

$$V_{EG} = \frac{m_{EG}}{\rho_{EG}}; \quad V_{HX} = \frac{m_{HX}}{\rho_{HX}} \tag{3.66}$$

The volume of the reactive solid at higher ammoniation state is defined as:

$$V_{S_2} = n_s \left(\frac{\bar{M}_S}{\rho_S} + \frac{\nu_2 \bar{M}_{NH_3}}{\rho_{NH_3}} \right) \tag{3.67}$$

Where ρ_{NH_3} is the density of ammonia. The assumption made here is that the volume of an ammoniated sorbent is equal to the sum between the pure solid volume and the volume of the adsorbed ammonia. Hence, the density of the solid at the high ammoniation level can be defined as follows:

$$\rho_{S_2} = \frac{m_{S_2}}{V_{S_2}} = \frac{\bar{M}_s + \nu_2 \bar{M}_{NH_3}}{\left(\frac{\bar{M}_s}{\rho_s} + \frac{\nu_2 \bar{M}_{NH_3}}{\rho_{NH_3}}\right)} \quad 3.68$$

The properties of the materials which compose the reactors are summarized in Table 3.1.

Table 3.1: Thermophysical properties of the reactor materials.

$\bar{M}_{NH_3}$	$\bar{c}_{NH_3}$	ρ_{NH_3}	c_{HX}	ρ_{HX}	c_{EG}	ρ_{EG}
[kg/mol]	[J/mol/K]	[kg/m^3]	[J/kg/K]	[kg/m^3]	[J/kg/K]	[kg/m^3]
0.017	80.27	600	921	2710	720	2000

3.2.3 Validation of the steady state model

The steady state system model has been validated using data resulting from the model proposed by Godefroy et al. [31]. In his work, the author investigated the performance of TRSC, adopting the single reaction $BaCl_2$ 8-0 as LTM, while using a broad set of solid/ammonia reactions as HTM. Table 3.2 represents the HTR reactions selected to validate the model, together with the corresponding operating hot source temperatures and volumetric expansion ratios. This last parameter is defined as:

$$R_v = \frac{v_2}{v_1} \quad 3.69$$

Where v_2 and v_1 are the specific volumes of ammonia at the expander outlet and inlet, respectively.

Table 3.2: HTR reactions (HTMs) selected for the steady state validation. For each reaction, different hot source temperatures and volumetric expansion ratios were adopted by Godefroy.

HTR reactions	$\Delta\bar{h}_r$	$\Delta\bar{s}_r$	T_H	R_v
[S ν_2-ν_1]	[J/mol]	[J/mol/K]	[K]	[-]
$ZnCl_2$ 4-2	49467	230.24	465.89	4.56
$CuCl_2$ 5-3.3	50241	230.75	470.37	4.56
$FeCl_2$ 6-2	51266	227.99	492.77	4.60
$CuCl_2$ 3.3-2	56497	237.22	497.25	4.44
$CoCl_2$ 6-2	53986	228.1	497.25	2.92
$MgCl_2$ 6-2	55660	230.63	497.25	2.64

Other relevant parameters have been set based on information found in Godefroy's work:

- Cold source temperature set to $T_C = 0$ °C.
- Scroll expander isentropic efficiency equal to $\eta_{is} = 1$.
- Parameters related to the amounts of metal and ENG are set to $\tau = 0$ and $f_{EG} = 0$.
- Work produced by the expander is set to $L = 1$ kWh.

Simulations have been run for each $BaCl_2$ 8-0-HTM configuration and first and second law efficiencies have been computed:

$$\eta_I = \frac{L + Q_C}{Q_H} \tag{3.70}$$

$$\eta_{II} = \frac{L + E_C}{E_H} \tag{3.71}$$

Figure 3.5 shows the values of such parameters obtained from the system steady state model for each HTM selected, compared with the available data.

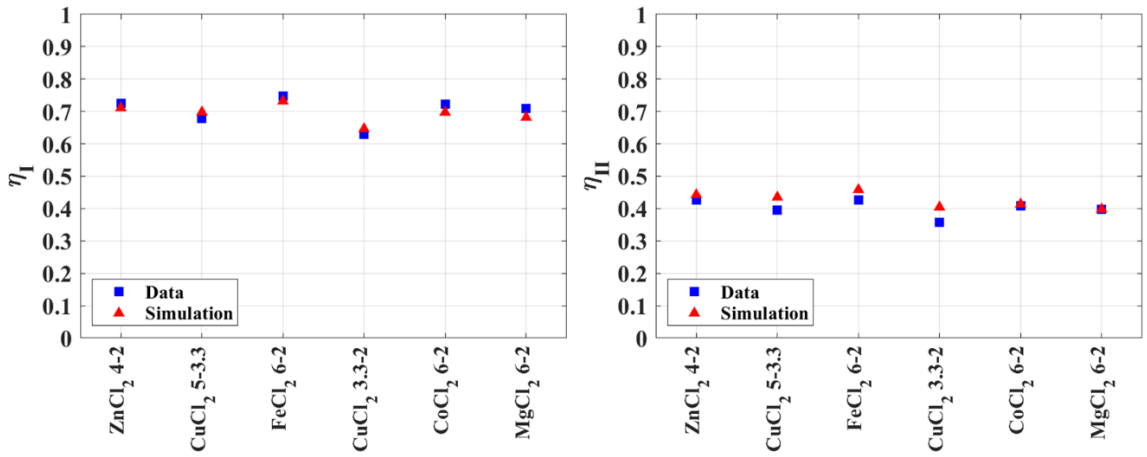

Figure 3.5: Validation of the system steady state model, with data taken from [31].

Table 3.3: Percentage relative error, related to each $BaCl_2$ 8-0-HTM configuration. $E_{rel,I}$ is the error related to η_I, $E_{rel,II}$ is the error corresponding to η_{II}.

HTR reactions	$E_{rel,I}$	$E_{rel,II}$
[S ν_2-ν_1]	[%]	[%]
$ZnCl_2$ 4-2	1.99	3.48
$CuCl_2$ 5-3.3	2.77	10.31
$FeCl_2$ 6-2	2.01	7.59
$CuCl_2$ 3.3-2	2.65	13.47
$CoCl_2$ 6-2	3.46	1.23
$MgCl_2$ 6-2	3.86	0.45

The percentage relative errors related to each simulation are reported in Table 3.3. Results show an overall good validation, with higher discrepancy in the evaluation of the second law efficiency.

3.3 Dynamic model

In the steady state case, an important feature of the thermochemical reactors is neglected within the cycle, that is the kinetics of the chemical reaction. In fact, chemisorption reactions have been modeled as ideally instantaneous processes, occurring purely at an equilibrium state (along the equilibrium lines). Nevertheless, practical solid/gas thermochemical reactions can only be carried out when temperature and pressure deviate from the equilibrium line to achieve reasonable heat and mass transfer rates and reaction kinetics (section 2.2). In the following section the lumped parameters model of TRSC implemented to capture the dynamics related to heat transfer and reaction kinetics phenomena in the whole cycle is presented. The main purpose of such a model is to investigate and physically interpret the transient behavior of relevant quantities, as well as to highlight the relation between system performance and components behavior in the dynamic state.

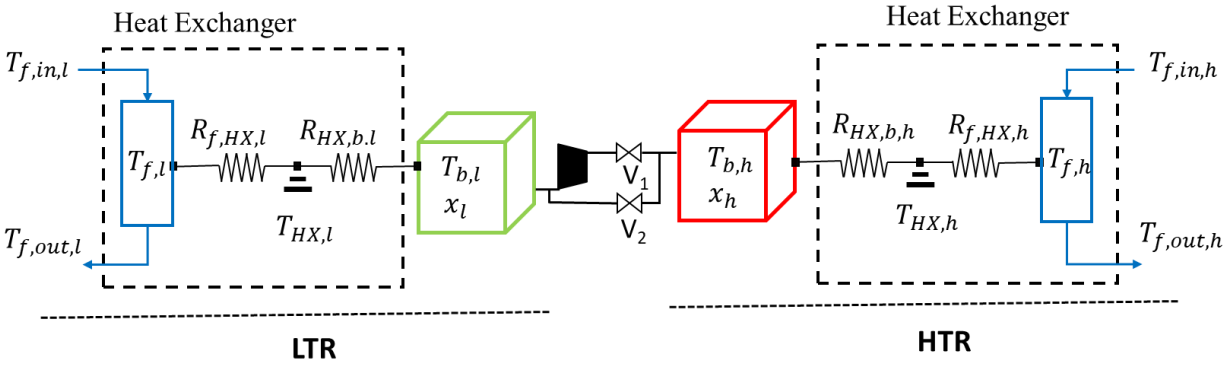

Figure 3.6: Schematics of the lumped parameters model. Subscript *l* indicates the LTR; subscript *h* indicates the HTR.

Figure 3.6 represents the schematics of the model. Each reactor is modeled through three lumped parameters:

- The heat transfer fluid (HTF), with mean temperature T_f:

$$T_f = \frac{T_{f,in} + T_{f,out}}{2} \tag{3.72}$$

- The heat exchanger metal, with temperature T_{HX}.
- The reactive bed temperature, with temperature T_b.

The heat exchanger is modeled through two thermal resistances: $R_{f,HX}$ between the HTF and the metal heat exchanger (fluid side), and $R_{HX,b}$ between the metal heat exchanger and the reactive bed (sorbent side). The corresponding overall thermal conductance coefficients are:

$$UA_{f,HX} = \frac{1}{R_{f,HX}}; \quad UA_{HX,b} = \frac{1}{R_{HX,b}} \tag{3.73}$$

In the following paragraphs, the set of ordinary differential equations adopted to model the working steps of the whole cycle is described. For simplicity, the Resorption case (bypassed expander) is firstly presented, while the effect of the scroll expander is added subsequently in the reaction charge phase. The equations are implemented and solved with a built-in MATLAB ODE solver.

3.3.1 Preheat and precool intermediate steps

Let us consider Figure 3.7, in which the intermediate steps in the simple resorption case are represented on the Clapeyron diagram.

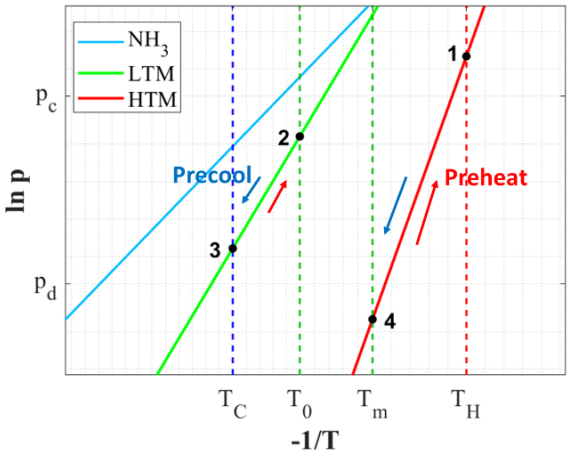

Figure 3.7: Intermediate steps in the dynamic case for the simple resorption cycle.

During preheat step the HTR is heated from T_m to T_H, while LTR is heated from T_C to T_0. On the other hand, during precool stage the reversed process is achieved and LTR is cooled from T_0 to T_C, while HTR is cooled from T_H to T_m.
Both reactors are modeled with one ODE for each of the three lumped components, i.e. six total equations. Concerning the HTR:

$$m_{f,h}c_{f,h}\frac{dT_{f,h}}{dt} = \dot{m}_{f,h}c_{f,h}\left(T_{f,in.h} - T_{f,out,h}\right) - UA_{f,HX,h}\left(T_{f,h} - T_{HX,h}\right) \tag{3.74}$$

$$m_{HX,h}c_{HX,h}\frac{dT_{HX,h}}{dt} = UA_{f,HX,h}\left(T_{f,h} - T_{HX,h}\right) - UA_{HX,b,h}\left(T_{HX,h} - T_{b,h}\right) \quad 3.75$$

$$TM_h\frac{dT_{b,h}}{dt} = UA_{HX,b,h}\left(T_{HX,h} - T_{b,h}\right) \quad 3.76$$

It should be noted that no thermal losses with the external environment have been considered. The equations set for the LTR are the same, but with the subscript l instead of h. m_f and $\dot{m}_f$ are the mass of HTF in the heat exchanger and the HTF mass flow rate respectively. It is assumed that HTF is water in the HTR and refrigerant R134a in the LTR. Hence, the specific heat c_f is defined depending on the operating conditions in each stage:

$$c_{f,h} = c(T_{f,in,h}, p_{eq,h}, water) \quad 3.77$$

$$c_{f,l} = c(T_{f,in,l}, p_{eq,l}, R134a) \quad 3.78$$

The thermal mass of the reactor in the dynamic state TM is defined as a function of the actual advancement of the adsorption/desorption reaction:

$$TM = xm_{S_2}c_{S_2} + (1-x)m_{S_1}c_{S_1} + m_{EG}c_{EG} \quad 3.79$$

During the preheat step the global conversion ratio x is constant and equal to 1 for HTR and 0 for LTR. On the contrary, during the precool step x is equal 0 for HTR and 1 for LTR. Note that the metal is not considered in TM, since its effect is already included in the corresponding lumped component. The input variables which define the evolution in time of the working steps are the ODEs initial conditions, the global conversion rate, and the HTF inlet temperature $T_{f,in}$. For a fixed working step, the initial conditions are assumed to be the same for the three lumped components:

$$T_b(0) = T_{HX}(0) = T_f(0) \quad 3.80$$

Table 3.4 summarizes the main input variables of ODEs for the two reactors in the two intermediate steps.

Table 3.4: Dynamic model HTF inlet temperature, initial conditions, and global conversion ratio in the two intermediate steps.

STEP	Reactor	$T_{f,in}$	$T_b(0)$	x
Preheat	HTR	T_H	T_m	1
	LTR	T_0	T_C	0
Precool	HTR	T_m	T_H	0
	LTR	T_C	T_0	1

3.3.2 Reaction charge phase

After the preheat stage, the HTR and LTR are at temperatures T_H and T_0, respectively (Figure 3.7). Connecting the two reactors, a non-equilibrium pressure is imposed and simultaneous HTM desorption and LTM adsorption are triggered. To model the kinetics of such reactions the semi-empirical equations proposed by Mazet et al. [43] were implemented:

$$Desorption \Rightarrow \frac{dx}{dt} = A_r x^{m_r} \frac{\left(p_c - p_{eq}(T_b)\right)}{p_c} \tag{3.81}$$

$$Adsorption \Rightarrow \frac{dx}{dt} = A_r (1-x)^{m_r} \frac{\left(p_c - p_{eq}(T_b)\right)}{p_c} \tag{3.82}$$

where A_r and m_r are the Arrhenius factor and the exponential factor, respectively. The former coefficient indicates the correlation between the reaction velocity and the working temperature, while the latter reflects the influence of the vacant sites on the reaction progress [33]. Such parameters depend on the considered solid/gas reaction and can be obtained experimentally. In this work, they were assumed constant and equal to the values obtained by Han et al. [39] for the reaction $MnCl_2$ 6-2. Hence A_r and m_r were assumed equal to 0.001087 and 1.185, respectively. The term p_c is the non-equilibrium pressure imposed on the reactors as they are connected, while $p_{eq}(T_b)$ is the reaction equilibrium pressure corresponding to the reactor temperature, which varies in time. During the reaction charge phase, equations 3.81 and 3.82 are applied to HTR and LTR, respectively. The equations related to the HTF and the heat exchanger metal of both reactors are the same as in the intermediate step (equations 3.74 and 3.75). On the other hand, the ODE related to the reactive bed becomes the following for both reactors:

$$\left(TM + m_{NH_3,tot} c_{NH_3}(1-x)\right)\frac{dT_b}{dt} = UA_{HX,b}(T_{HX} - T_b) + m_{NH_3,tot}\Delta h_r \frac{dx}{dt} \tag{3.83}$$

The term added to the thermal mass TM on the left-hand side of the equation considers the mass of ammonia which is being adsorbed/desorbed during the process. Hence, the assumption done here is that the adsorbed/desorbed gaseous ammonia is at the same temperature as the reactor undergoing synthesis/decomposition. Such a hypothesis is physically realistic in the decomposition process since the vapor is desorbed at the reactor's temperature. On the other hand, during synthesis, the gaseous ammonia is in thermal disequilibrium with the reactor, and equation 3.83 is less consistent. Nevertheless, the quantity of transferred heat between gaseous and solid phase during adsorption/desorption has not a direct impact on the key performance parameters evaluated in this work, as it can be inferred from equations 3.37 and 3.38. The term added on the right-hand side of equation 3.83 defines the heat of adsorption/desorption within the reactor. Note that the heat of reaction Δh_r has been considered constant with respect to temperature in the dynamic analysis.

So far, a system of eight ODEs has been defined, describing the evolution in time of $T_b, T_{HX}, T_f \; and \; x$ in both reactors. A final equation is needed to determine the constrain pressure p_c. Such an equation is obtained by imposing the mass balance between HTR and LTR. In fact, during the reaction charge phase, the mass flow rate of desorbing ammonia from HTR should be the same as the mass flow rate of adsorbing ammonia in LTR:

$$\dot{m}_{NH_3,des,h} = \dot{m}_{NH_3,ads,l} = \dot{m}_{NH_3} \tag{3.84}$$

The mass flow rate of ammonia can be obtained from the definition of global conversion rate (equation 3.7):

$$\frac{d}{dt} m_{NH_3,h} = \frac{dx_h}{dt} m_{NH_3,tot,h} \tag{3.85}$$

$$\frac{d}{dt} m_{NH_3,l} = \frac{dx_l}{dt} m_{NH_3,tot,l} \tag{3.86}$$

Applying the mass balance equation to each reactor:

$$\dot{m}_{NH_3,des,h} = -\frac{d}{dt} m_{NH_3,h} \tag{3.87}$$

$$\dot{m}_{NH_3,des,l} = \frac{d}{dt} m_{NH_3,l} \tag{3.88}$$

Hence, equation 3.84 can be rewritten as:

$$-m_{NH_3,tot,h} \frac{dx_h}{dt} = m_{NH_3,tot,l} \frac{dx_l}{dt} \tag{3.89}$$

Substituting 3.81 and 3.82 into the above equation, the following expression for p_c is obtained:

$$p_c = \frac{A_{r,h}\, x_h^{m_{r,h}} p_{eq,h}\left(T_{b,h}\right) m_{NH_{3,tot,h}} + A_{r,l}\,(1-x_l)^{m_{r,l}} p_{eq,h}\left(T_{b,l}\right) m_{NH_{3,tot,l}}}{A_{r,h}\, x_h^{m_{r,h}} m_{NH_{3,tot,h}} + A_{r,l}\,(1-x_l)^{m_{r,l}} m_{NH_{3,tot,l}}} \tag{3.90}$$

In the case the reactors are sized to exchange the same quantity of stoichiometric ammonia (equation 3.48), the equation for the non-equilibrium pressure becomes:

$$p_c = \frac{A_{r,h}\, x_h^{m_{r,h}} p_{eq,h}\left(T_{b,h}\right) + A_{r,l}\,(1-x_l)^{m_{r,l}} p_{eq,h}\left(T_{b,l}\right)}{A_{r,h}\, x_h^{m_{r,h}} + A_{r,l}\,(1-x_l)^{m_{r,l}}} \tag{3.91}$$

3.3.3 The effect of the scroll expander in the reaction charge phase

Compared to the simple resorption case, the reaction charge phase for the TRSC is characterized by the expansion of vapor ammonia caused by the scroll expander. Since the aim of the model is to capture the dynamic effect of the reaction kinetics by means of a simple lumped parameters model, the same approach is adopted to account for the influence of the expander on the system. Hence, the effect of the expansion of gaseous ammonia before its adsorption in the LTR is considered through the following assumption: while in the resorption case, after the opening of the valve, a singlel non-equilibrium pressure p_c is imposed on both reactors, in the TRSC case the reactors are subjected to two distinct non-equilibrium pressures $p_{c,h}$ and $p_{c,l}$, triggering desorption and adsorption in HTR and LTR, respectively (Figure 3.8).

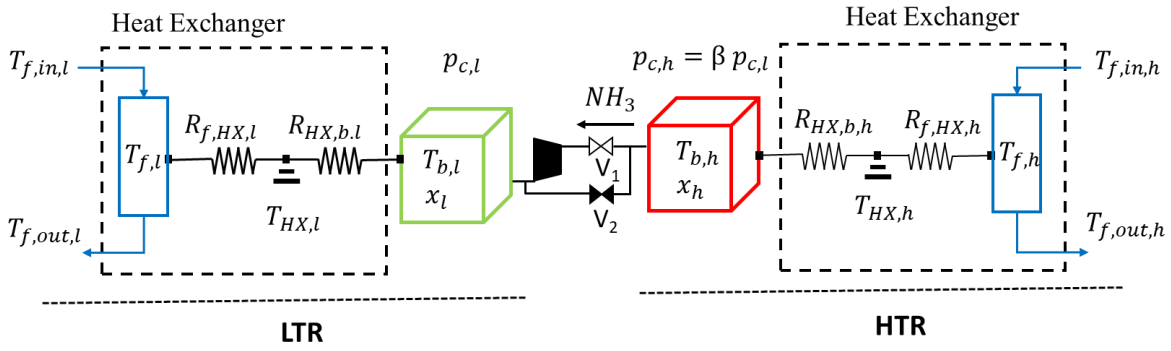

Figure 3.8: Schematics of the lumped parameters dynamic model for the reaction charge phase.

The two imposed pressures are related by the pressure ratio, which is the only parameter describing the expander in the model, together with the isentropic efficiency:

$$\beta = \frac{p_{c,h}}{p_{c,l}} \tag{3.92}$$

Therefore equations 3.81, 3.82 and 3.90 become:

$$\frac{dx_h}{dt} = A_{r,h} x_h^{m_{r,h}} \frac{\left(\beta p_{c,l} - p_{eq,h}(T_{b,h})\right)}{\beta p_{c,l}} \tag{3.93}$$

$$\frac{dx_l}{dt} = A_{r,l} (1 - x_l)^{m_{r,l}} \frac{\left(p_{c,l} - p_{eq,l}(T_{b,l})\right)}{p_{c,l}} \tag{3.94}$$

$$p_{c,l} = \frac{A_{r,h}\, x_h^{m_{r,h}} p_{eq,h}(T_{b,h})\, m_{NH_3,tot,h} + \beta A_{r,l}\, (1 - x_l)^{m_{r,l}} p_{eq,l}(T_{b,l})\, m_{NH_3,tot,l}}{\beta A_{r,h}\, x_h^{m_{r,h}} m_{NH_3,tot,h} + \beta A_{r,l}\, (1 - x_l)^{m_{r,l}} m_{NH_3,tot,l}} \tag{3.95}$$

Table 3.5: Inlet temperature of the HTF and initial conditions in the reaction charge phase.

PHASE	Reactor	$T_{f,in}$	$T_b(0)$	$x(0)$
Reaction charge	HTR	T_H	T_H	1
	LTR	T_0	T_0	0

Table 3.5 summarizes the input and initial conditions of the set of ODEs for the reaction charge phase.

3.3.4 Reaction discharge phase

Before the reaction discharge phase, HTR and LTR are brought to temperatures T_m and T_C, respectively, through the precool phase. As the reactors are connected, refrigeration is generated at temperature T_C, meaning that the HTF outlet temperature of LTR is set equal to T_C. Therefore, the equation (3.74) for the HTF is modified to impose the cold production at T_C with a defined fluid temperature variation between inlet and outlet ΔT_C:

$$\dot{m}_{f,l} c_{f,l} \Delta T_C = U A_{f,HX,l} \left(T_{f,l} - T_{HX,l}\right) \tag{3.96}$$

$$\Delta T_C = \left(T_{f,in.l} - T_{f,out,l}\right) \tag{3.97}$$

Thus, the mean temperature of LTR heat transfer fluid is assumed constant in time and no ODE is set for temperature $T_{f,l}$. The equations for the metal heat exchanger and for the reactive bed are the same as in the reaction charge phase for both reactors. On the other hand, since the LTR undergoes desorption, while the HTR achieves synthesis the equations relative to the reactors global conversion rates and to the imposed pressure p_d become:

$$\frac{dx_l}{dt} = A_{r,l} x_l^{m_{r,l}} \frac{\left(p_d - p_{eq,l}\left(T_{b,l}\right)\right)}{p_d} \tag{3.98}$$

$$\frac{dx_h}{dt} = A_{r,h} (1 - x_h)^{m_{r,h}} \frac{\left(p_d - p_{eq,h}\left(T_{b,h}\right)\right)}{p_d} \tag{3.99}$$

$$p_d = \frac{A_{r,l}\, x_l^{m_{r,l}} p_{eq,l}\left(T_{b,l}\right) m_{NH_{3,tot,l}} + A_{r,h}\, (1 - x_h)^{m_{r,h}} p_{eq,h}\left(T_{b,h}\right) m_{NH_{3,tot,h}}}{A_{r,l}\, x_l^{m_{r,l}} m_{NH_{3,tot,l}} + A_{r,h}\, (1 - x_h)^{m_{r,h}} m_{NH_{3,tot,h}}} \tag{3.100}$$

The total number of ODEs in the reaction discharge phase is seven, i.e. three for the LTR ($T_{b,l}$, $T_{HX,l}$, x_l) and four for the HTR ($T_{f,h}$, $T_{b,h}$, $T_{HX,h}$, x_h), while two are the constrain equations (3.96 and 3.100).

Table 3.6 summarizes the input and initial conditions of the set of ODEs for the reaction discharge phase.

Table 3.6: Input variables and initial conditions for ODEs relative to reaction discharge phase.

PHASE	Reactor	$T_{f,in}$	$T_{f,out}$	$T_b(0)$	$x(0)$
Reaction discharge	HTR	T_m	/	T_m	0
	LTR	$T_C + \Delta T_C$	T_C	T_C	1

3.3.5 Energy calculation

The total energy transferred into and from the system is calculated by integrating the energy fluxes with respect to time. For instance, the total energy to be stored is:

$$Q_{H,t} = \int_0^{t_{charge}} \dot{m}_{f,h} c_{f,h} \left(T_{f,in.h} - T_{f,out,h}\right) dt \tag{3.101}$$

Where t_{charge} is the sum of the preheat time and the reaction charge time. The refrigeration energy can be computed as:

$$Q_{C,t} = \int_0^{t_{d,sen}} \dot{m}_{f,l} c_{f,l} \left(T_{f,in.l} - T_{f,out,l}\right) dt + \int_0^{t_{d,r}} \dot{m}_{f,l} c_{f,l}\, \Delta T_C\, dt \tag{3.102}$$

Where $t_{d,sen}$ and $t_{d,r}$ are respectively the precool (sensible discharge) time and the reaction discharge time. The work produced by the expander is obtained through integration in time of the scroll expander power W:

$$L_t = \int W dt = \int_0^{t_{c,r}} \dot{m}_{NH_3,des.h} (h_1 - h_2) dt \tag{3.103}$$

$t_{c,r}$ is the reaction charge time. The values of enthalpy have been calculated at each time step with the *refprop* MATLAB tool, applying the same procedure as in the thermodynamic cycle implementation (equation from 3.18 to 3.23).
Finally, total exergy relative to the stored energy and the refrigeration effect can be computed:

$$E_{C,t} = Q_{C,t} \left(\frac{T_0}{T_C} - 1\right) \tag{3.104}$$

$$E_{H,t} = Q_{H,t} \left(1 - \frac{T_0}{T_H}\right) \tag{3.105}$$

3.3.6 Validation of the dynamic model

The dynamic model has been validated in the reaction charge phase of the simple resorption case through experimental data obtained from the work of Wu et al. [38]. The HTM and LTM adopted by Wu were $MnCl_2$ 6-2 and $SrCl_2$ 8-1, respectively, with the main input parameters represented in Table 3.7.

Table 3.7: Input parameters for the validation of the dynamic model.

$m_{s,h}$	$m_{s,l}$	T_H	T_0	T_C	T_m	m_{EG}/m_s	V_{HX}
[kg]	[kg]	[°C]	[°C]	[°C]	[°C]	[-]	[m^3]
3.21	3.72	120	50	30	50	85/15	0.009

The following assumptions were made:

- The thermal conductance of the heat exchanger was set to $UA = 200$ W/K for both the HTF and sorbent sides, in both reactors.
- The heat transfer fluid mass in the heat exchanger is assumed to be equal to the metal mass $m_f = m_{HX}$.
- The heat transfer fluid mass flow rate is assumed $\dot{m}_f = m_f/10$.

Figure 3.9 shows the validation for the reactor's temperature trends during the reaction charge phase.

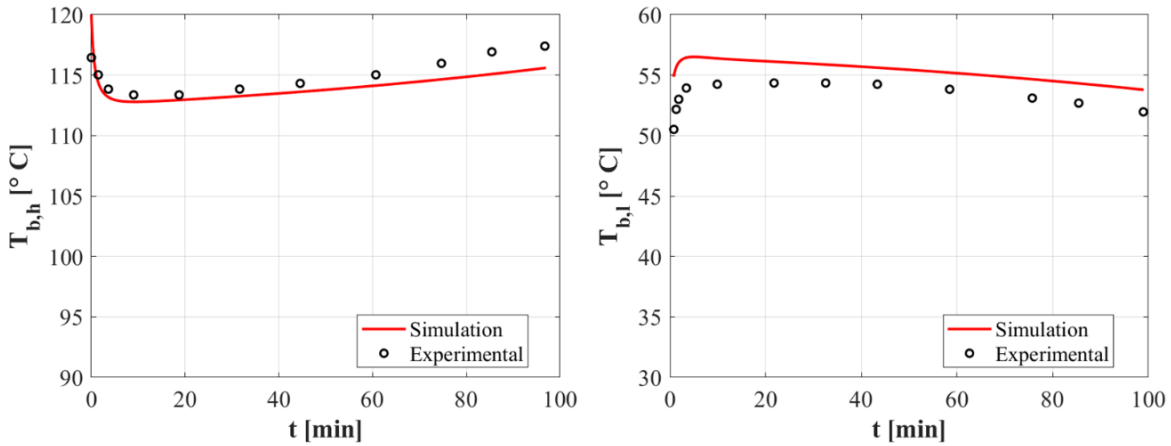

Figure 3.9: Validation of the temperature evolutions of HTR (left) and LTR (right) during reaction charge phase.

The validation results to be satisfactory from both the trend and temperature values viewpoints. A validation has been carried out also for the non-equilibrium pressure imposed on the two reactors, and it is represented in Figure 3.10. It results that the model provides a pressure trend that good resembles the evolution in time obtained in the experiments, but which is less satisfactory in terms of the intensity.

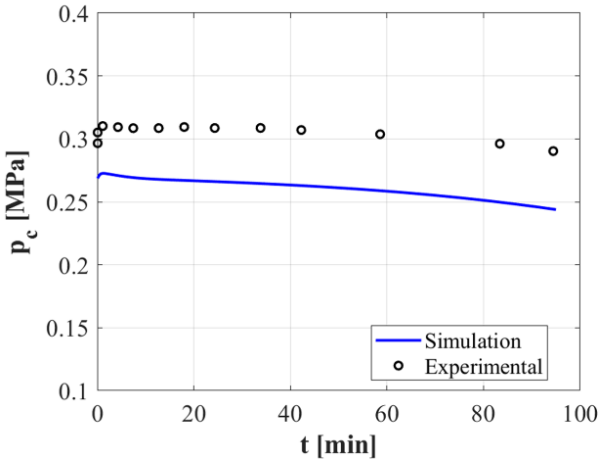

Figure 3.10: Validation of the constraint pressure trend during the reaction charge phase.

Through simulations, it was found that the pressure trend is very sensible to the molar entropy of reaction $\Delta\bar{s}_r$ of the solid/gas reaction considered. Figure 3.11 shows the validation obtained by increasing $\Delta\bar{s}_r$ by 0.5 % for both $MnCl_2$ 6-2 and $SrCl_2$ 8-1, which results in better quality.

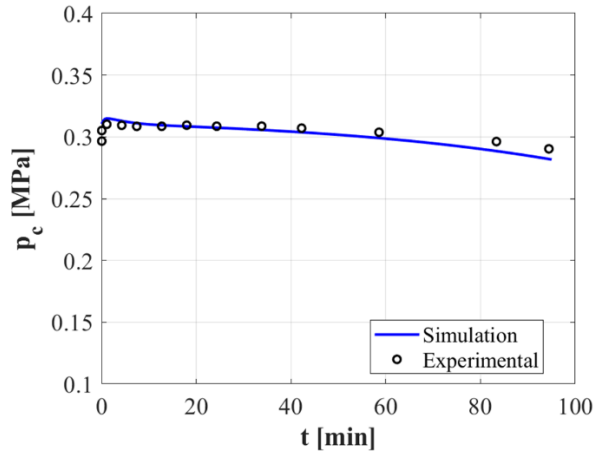

Figure 3.11: Validation of constraint pressure trend during reaction charge phase, after increasing the molar entropy of reaction of HTM and LTM by a percentage of 0.5 %.

Such a feature of the model is consistent with the fact that the properties of reactive mixtures at equilibrium cannot be defined by precise values. Instead, as it is acknowledged in the literature, a real solid/gas equilibrium condition is described by an area surrounding the equilibrium line on the Clapeyron diagram, defined as pseudo-equilibrium area [44,45]. For simplicity, pseudo-equilibrium areas are not considered for the solid/gas reactions adopted and their properties are assumed constant. The relative error between simulated results and experimental data has been computed in terms of integration of the temperature trends with respect to time (Figure 3.9). The percentage relative deviation obtained is 0.0034% for the HTR and 0.59 % for the LTR.

4. Application side

The general model presented in the previous chapter is used to explore a specific application for the TRSC for cold and power production. Hence, the following section aims to describe the main characteristics of the model configuration adopted and the rationale behind it, introducing the reader to the last chapter, addressing the main results. Firstly, the model structure and operating conditions are defined. Then, the strategy for the selection of suitable reactive mixtures to be used in the system reactors among a series of metal chloride-ammonia reactions is described. Finally, an overview of the computed key performance indicators is presented.

4.1 Model Configuration

Figure 4.1 shows how the developed modeling tool is used to investigate the TRSC adopted in a specific low-grade heat application.

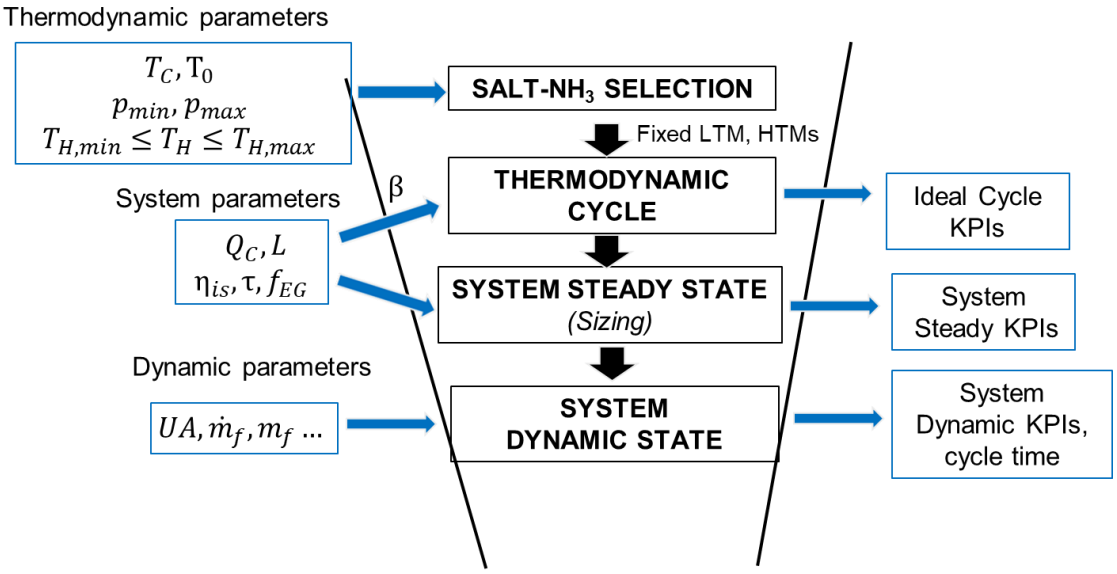

Figure 4.1: Model configuration to carry out the performance evaluation for a specific TRSC application.

Operating conditions are set in terms of thermodynamic parameters, system parameters and dynamic parameters: thermodynamic parameters represent the boundaries imposed to the thermodynamic cycle, such as operating temperatures and pressures. After defining such boundaries, a list of metal chloride-ammonia reactions is investigated and a single salt-NH_3 reaction to be used as LTM is selected, as well as a series of suitable HTM that can be coupled to it. Adding the system parameters, such as the energy requirements, to the coding tool in EES, the system sizing and pressure ratio are obtained. Key performance indicators related to the ideal thermodynamic cycle and to the overall system in steady state conditions for each LTM-

HTM couple can be computed. Finally, adding the dynamic parameters, the transient state can be studied and the related KPIs are obtained, together with the cycle time.
Realistic operating conditions in terms of thermodynamic parameters are set:

- Refrigeration temperature is set to $T_C = 0$ °C , with HTF temperature variation $\Delta T_C = 10$ °C.
- Environmental temperature is set to $T_0 = 30$ °C.
- Hot source temperature is not fixed, but ranges between two boundary values, i.e. $100\ °C \leq T_H \leq 200\ °C$.
- Minimum and maximum operating pressures are set to $p_{min} = 0.05$ bar and $p_{max} = 30$ bar.

Regarding the system parameters:

- In terms of application needs, for each cycle the system must provide fixed cold and work production $Q_c = 120$ kWh and $L = 12$ kWh.
- The isentropic efficiency of the expander is set to $\eta_{is} = 0.8$.
- For both reactors, the metal ratio and the graphite ratio are set to respectively $\tau = 0.3$ and $f_{EG} = 0.5$.

Main dynamic parameters are set as follows for both reactors:

- The global thermal conductance is fixed to $UA = 2000$ W/K.
- The heat transfer fluid mass in the heat exchanger is assumed to be equal to the metal mass $m_f = m_{HX}$.
- The heat transfer fluid mass flow rate is assumed $\dot{m}_f = m_f/10$.

4.2 Salt – ammonia reactions selection

A series of 35 metal chloride-ammonia reactions (Table 4.1) has been investigated as possible reactive mixtures for the low temperature (LTR) and high temperature reactors (HTR). Main properties such as enthalpy and entropy of reaction and molar specific heat of the pure salts are taken from the literature [14,46]. Note that the molar enthalpy and entropy of reaction correspond to a reference pressure $p_0 = 1$ Pa. Ammonia has been chosen as working fluid given its several benefits mentioned in paragraph 1.4.4, e.g. it is environmentally friendly, chemically stable, and it has a low boiling point. On the other hand, metal chlorides are selected as solid sorbents for the following advantages compared to other solids to be coupled with ammonia in chemisorption reactions [14]:

- Large total adsorption quantity ($> 1\ kg_{NH_3}/kg_s$ for most metal chlorides).
- High working pressure for metal chloride-NH_3 reactions, ensuring reasonable mass transfer performance.
- A large variety of metal chlorides makes them suitable for a large range of operating temperatures.
- Metal chloride-NH_3 is considered as the optimal working pair in terms of both cost and performance criteria.

Table 4.1: Database of the investigated metal chlorides – NH_3 reactions.

Salt – NH3	$\boldsymbol{\Delta\bar{h}_r}$	$\boldsymbol{\Delta\bar{s}_r}$	$\boldsymbol{\bar{c}_s}$	$\boldsymbol{\bar{M}_s}$
[S ν_2-ν_1]	[J/mol]	[J/mol/K]	[J/mol/K]	[kg/mol]
$BaCl_2$ 8-0	37665	227.25	75.10	0.208
$MnCl_2$ 6-2	47416	228.07	72.86	0.126
$NiCl_2$ 2-1	79515	232.17	71.60	0.130
$ZnCl_2$ 10-6	29588	219.23	71.27	0.136
$CaCl_2$ 4-2	42268	229.92	72.52	0.111
$FeCl_2$ 6-2	51266	227.99	76.57	0.127
$MnCl_2$ 2-1	71019	232.35	72.86	0.126
$MgCl_2$ 1-0	87048	230.88	71.31	0.095
$SrCl_2$ 8-1	41431	228.8	75.53	0.159
$ZnCl_2$ 1-0	104625	227.79	71.27	0.136
$CaCl_2$ 8-4	41013	230.3	72.52	0.111
$CuCl_2$ 10-6	31387	227.72	71.81	0.134
$SnCl_2$ 9-4	31806	224.86	70.60	0.190
$PbCl_2$ 8-3.25	34317	223.76	70.05	0.278
$SnCl_2$ 4-2.5	38920	229.82	70.60	0.190
$PbCl_2$ 3.25-2	39339	230.27	70.05	0.278
$ZnCl_2$ 6-4	44779	230.24	71.27	0.136
$PbCl_2$ 2-1.5	46035	230.89	70.05	0.278
$PbCl_2$ 1.5-1	47290	232.5	70.05	0.278
$ZnCl_2$ 4-2	49467	230.24	71.27	0.136
$CuCl_2$ 5-3.3	50241	230.75	71.81	0.134
$CuCl_2$ 3.3-2	56497	237.22	71.81	0.134
$CoCl_2$ 6-2	53986	228.1	78.41	0.130
$PbCl_2$ 1-0	55660	231.04	70.05	0.278
$MgCl_2$ 6-2	55660	230.63	71.31	0.095
$NiCl_2$ 6-2	59217	227.75	71.60	0.130
$CaCl_2$ 2-1	63193	237.34	72.52	0.111
$MgCl_2$ 2-1	74911	230.3	72.86	0.095
$FeCl_2$ 2-1	76167	231.91	76.57	0.127
$CoCl_2$ 2-1	78134	232.17	78.41	0.130
$ZnCl_2$ 2-1	80352	229.72	71.27	0.136
$MnCl_2$ 1-0	84202	233.18	72.86	0.126
$FeCl_2$ 1-0	86880	233.01	76.57	0.127
$CoCl_2$ 1-0	88303	232.8	78.41	0.130
$NiCl_2$ 1-0	89810	233.01	71.60	0.130

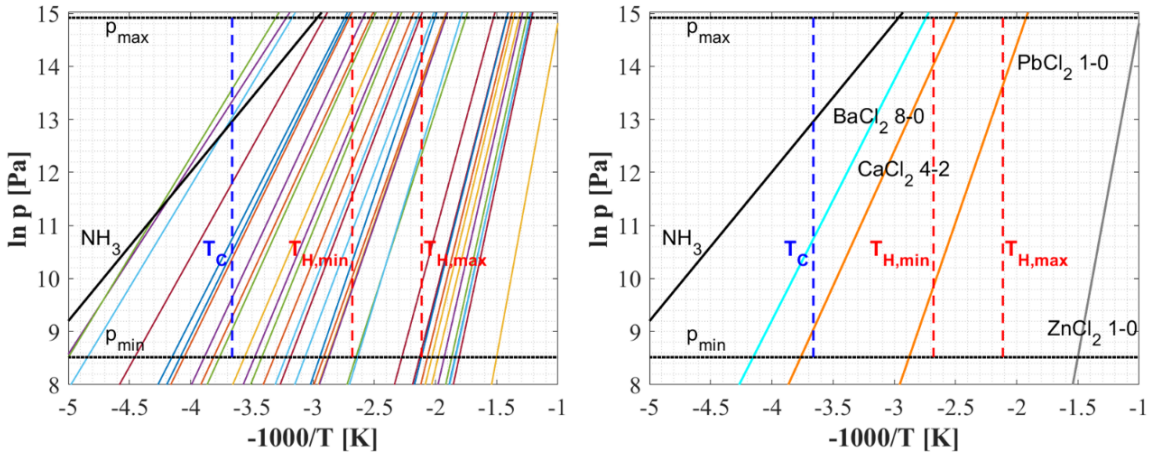

Figure 4.2: Equilibrium lines of all the metal chloride-ammonia reactions in Table 4.2 and operating temperatures and pressures (left). In the right graph: example of suitable salt-ammonia reactions (cyan and orange lines) and not suitable reactions (grey line) for the specified operating conditions.

It is clear from Figure 4.2 that the selection of suitable metal chloride-ammonia reactions depends on the fixed operating temperatures and pressures. Regarding the LTR, which operates at the refrigeration temperature T_C during the discharge phase, only the salts having the equilibrium pressure $p_{eq}(T_C)$ between the minimum allowable pressure and the ammonia saturation pressure $p_{NH_3}(T_C)$ are selected. Graphically, suitable LTR salts have the intersection between the equilibrium lines and the refrigeration temperature line (blue line) in the area delimited by the minimum pressure line and the ammonia saturation line. Similar logic is applied for the selection of reactive mixtures in the HTR, operating at a temperature T_H ranging between $T_{H,min}$ and $T_{H,max}$: suitable HTR salts are characterized by equilibrium lines which pass across the area defined by the two extreme hot source temperature lines (red lines) and the extreme operating pressures. As an example, the right graph in Figure 4.2 represents the equilibrium lines of four salt-ammonia reactions with respect to the thermodynamic operating conditions: $BaCl_2$ 8-0 is suitable as LTM but not as HTM; $CaCl_2$ 4-2 can be adopted as both LTM and HTM; $PbCl_2$ 1-0 is suitable only as HTM; $ZnCl_2$ 1-0 cannot be adopted in the system. In the following paragraphs, additional considerations are carried out to further narrow down the metal chloride-ammonia reactions to be adopted in the LTR and the HTR.

4.2.1 LTR reactive mixture

Once the metal chloride-ammonia reactions which fulfill the above described requirements have been identified, a single LTR salt can be selected based on its intrinsic properties, such as mass energy density ed_m, volume energy density ed_V and specific adsorption capacity S_C:

$$ed_m = \frac{\Delta H_r(\nu_2 - \nu_1)}{\bar{M}_{S_2}} \qquad 4.1$$

$$ed_V = \frac{\Delta H_r(\nu_2 - \nu_1)}{\bar{M}_{S_2}} \rho_{S_2} \quad 4.2$$

$$S_C = \frac{(\nu_2 - \nu_1)\bar{M}_{NH_3}}{\bar{M}_s} \quad 4.3$$

The first two parameters describe how much energy can be managed by the reactive mixture per unit mass and unit volume, while the last parameter represents the quantity of gaseous ammonia that can be adsorbed/desorbed per unit mass of pure salt. As it can be seen from Table 4.2 where the most promising metal chlorides have been shortlisted, $BaCl_2$ 8-0 and $SrCl_2$ 8-1 appear to be the reactions with the better intrinsic energetic properties, with values of ed_m and ed_V in the range of $0.24 - 0.28$ kWh/kg and $280 - 300$ kWh/m^3 respectively. The latter has been selected as the definitive LTM for its highest sorption capacity, given that, in the overall system, work is extracted through a scroll expander: in fact, a higher quantity of gaseous ammonia transferred between the two reactors yields a higher work production per unit mass of pure salt. Moreover, as it is later discussed in the Results chapter (chapter 5), selecting the reaction with a higher S_C ensures a higher system efficiency in terms of reduced thermal mass effects.

Table 4.2: Suitable LTR salt-NH_3 reactions. $SrCl_2$ 8-1 has been selected as LTR for the analysis.

LTM	$\Delta\bar{h}_r$	$\Delta\bar{s}_r$	$\bar{c}_s$	$\bar{M}_s$	ed_m	ed_V	S_C
[S ν_2-ν_1]	[J/mol]	[J/mol/K]	[J/mol/K]	[kg/mol]	[kWh/kg]	[kWh/m^3]	[kg_{NH_3}/kg_s]
$BaCl_2$ 8-0	37665	227.25	75.10	0.208	0.243	298.2	0.653
$CaCl_2$ 4-2	42268	229.92	72.52	0.111	0.131	142.4	0.306
$SrCl_2$ 8-1	41431	228.8	75.53	0.159	0.274	289.1	0.751
$CaCl_2$ 8-4	41013	230.3	72.52	0.111	0.185	163.8	0.613
$PbCl_2$ 8-3.25	34317	223.76	70.05	0.278	0.109	165.1	0.290
$SnCl_2$ 4-2.5	38920	229.82	70.60	0.190	0.063	100.5	0.134
$PbCl_2$ 3.25-2	39339	230.27	70.05	0.278	0.041	97.8	0.076

4.2.2 HTR reactive mixtures

Concerning the high temperature reactor, further considerations need to be made to select the proper HTMs and to guarantee the correct functioning of the resorption cogeneration system. Two conditions must be met:

- The equilibrium pressure of the HTM at hot source temperature must be higher than the equilibrium pressure of the selected LTM (i.e. $SrCl_2$ 8-1*)* at ambient source temperature.
- At fixed pressure, the equilibrium temperature of the HTM must be higher than the equilibrium temperature of the selected LTM.

If the first condition is not fulfilled, the scroll expander cannot be equipped to the system, since the gaseous ammonia would flow in counterpressure. Moreover, regardless of the use of the expander, the resorption system could not operate because of practical issues relating to the system pressure and equilibrium deviation described in paragraph 2.2.1: before triggering desorption-adsorption in two reactors, the desorbing reactor must be kept at an equilibrium pressure higher than the equilibrium pressure of the adsorbing reactor. If such a condition is not fulfilled the non-equilibrium pressure imposed in the two reactors when the valve is opened would not be able to activate the sorption reactions.
The second condition is related to the fact that once the LTM is fixed, HTR salts must effectively work as a High Temperature Material.
Differently with respect to the LTM selection, the HTR reactive mixtures explored in this work are not unique. Indeed, all the suitable HTR salt-ammonia reactions (Table 4.3) among the list of 35 metal chlorides-ammonia reactions are investigated at different hot source temperatures. The hot source temperatures for each HTM is defined according to the following criteria:

- if $p_{min} < p_{eq}(T_{H,max}) < p_{max}$, then $T_H = T_{H,max}$.
- if only $p_{min} < p_{eq}(T_{H,min}) < p_{max}$, then $T_H = T_{eq}(p_{max})$.

The resulting hot source temperatures are shown in Table 4.3 together with the operating pressure ratios, for the various configurations considered.

Table 4.3: HTR salt-ammonia reactions suitable to be coupled with $SrCl_2$ 8-1 LTR reaction. Hot source temperatures and pressure ratios selected for the various configurations are also shown.

HTM	$\boldsymbol{\Delta\bar{h}_r}$	$\boldsymbol{\Delta\bar{s}_r}$	$\boldsymbol{\bar{c}_s}$	$\boldsymbol{\bar{M}_s}$	$\boldsymbol{S_C}$	$\boldsymbol{T_H}$	$\boldsymbol{\beta}$
[S ν_2-ν_1]	[J/mol]	[J/mol/K]	[J/mol/K]	[kg/mol]	[kg_{NH_3}/kg_s]	[K]	[-]
$FeCl_2$ 6-2	51266	227.99	76.57	0.127	0.536	473.15	2.90
$CuCl_2$ 3.3-2	56497	237.22	71.81	0.134	0.164	473.15	2.95
$CoCl_2$ 6-2	53986	228.1	78.41	0.130	0.524	473.15	3.06
$PbCl_2$ 1-0	55660	231.04	70.05	0.278	0.061	473.15	3.08
$MgCl_2$ 6-2	55660	230.63	71.31	0.095	0.714	473.15	3.10
$NiCl_2$ 6-2	59217	227.75	71.60	0.130	0.525	473.15	3.48
$CaCl_2$ 2-1	63193	237.34	72.52	0.111	0.153	473.15	3.44
$MnCl_2$ 6-2	47416	228.07	72.86	0.126	0.540	455.60	3.07
$CaCl_2$ 4-2	42268	229.92	72.52	0.111	0.306	399.04	4.19
$ZnCl_2$ 6-4	44779	230.24	71.27	0.136	0.249	421.47	3.77
$PbCl_2$ 2-1.5	46035	230.89	70.05	0.278	0.031	430.66	3.55
$PbCl_2$ 1.5-1	47290	232.5	70.05	0.278	0.031	435.84	3.44
$ZnCl_2$ 4-2	49467	230.24	71.27	0.136	0.249	465.60	2.91
$CuCl_2$ 5-3.3	50241	230.75	71.81	0.134	0.215	470.62	2.84

Finally, Figure 4.3 shows the general thermodynamic boundaries on the Clausius-Clapeyron diagram for the two salt-ammonia reactions.

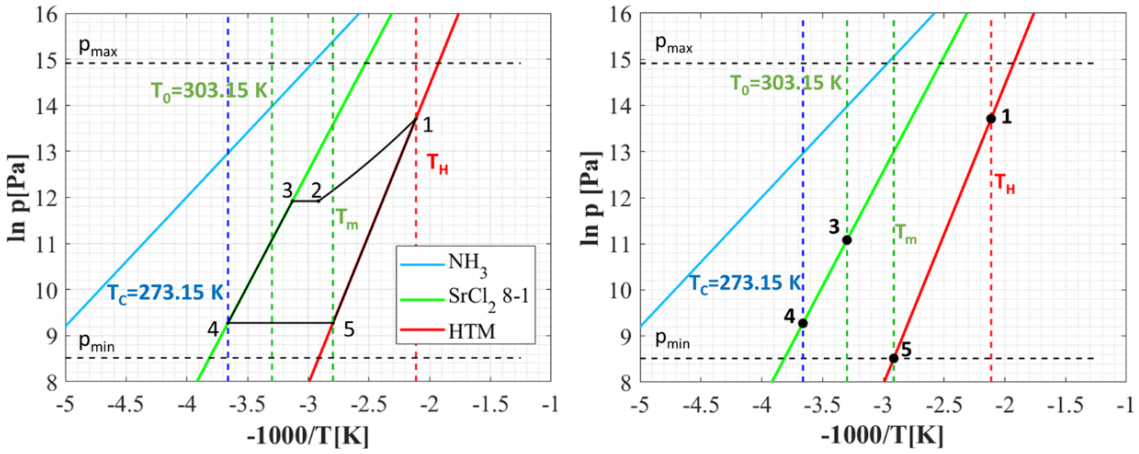

Figure 4.3: General thermodynamic conditions imposed to the LTM-HTM pairs for the steady state case (left) and the dynamic case (right).

It can be seen from this graph which conditions each LTM-HTM pair operates at, and the differences, in such conditions, between the steady state case and the dynamic case. Such differences are relevant since they will directly affect the results discussed in the last chapter. Particularly, it is important to remark that:

- In the dynamic case since the selected LTM and temperatures T_C and T_0 are fixed for each LTM-HTM pair evaluated, the operating points **3** and **4** are also fixed. Regarding the steady state case, point 4 is fixed but the operating point 3 changes since the pressure ratio varies for each configuration. The deriving implications are linked to the sensible heat contribution in the precool phase and they are discussed in the Results chapter.
- For each HTM the pressure corresponding to operating the point **5** in the dynamic case is fixed and equal to the minimum permitted pressure p_{min}. Hence, varying the HTM the intermediate temperature T_m changes but the pressure difference $p_4 - p_5$ remains the same. In the steady state case, no pressure difference is considered between the reactors during the discharge desorption/adsorption stage and the intermediate temperature T_m is different with respect to the corresponding temperature in the dynamic case. Again, the related effects on the computed sensible heat in the preheat phase and on the results is examined in the next chapter.
- Varying the selected HTM, the operating point **1** also varies, both in terms of temperature and pressure, for both steady and dynamic case.

4.3 Performance evaluation

Once the suitable metal chlorides-ammonia reactions to be used in the system have been identified, which are $SrCl_2$ 8-1 for the Low Temperature Reactor and the reactions in Table 4.3 for the High Temperature Reactor, the cycle is simulated for each LTM-HTM pair. The Key Performance Indicators (KPIs) obtained at three different levels are defined:

- **Ideal cycle KPIs**, which reveal the performance of the pure thermodynamic cycle. Such parameters are the ideal first and second law efficiencies:

$$\eta_{I,id} = \frac{l + q_C}{q_H} \tag{4.4}$$

$$\eta_{II,id} = \frac{l + e_c}{e_H} \tag{4.5}$$

- **System steady state KPIs**, which consider the effects of the overall thermal masses. Relevant parameters evaluated are the system first and second law efficiencies and mass and volume energy densities:

$$\eta_I = \frac{L + Q_C}{Q_H} \tag{4.6}$$

$$\eta_{II} = \frac{L + E_c}{E_H} \tag{4.7}$$

$$ED_m = \frac{L + Q_C}{m_{tot}}; \quad ED_V = \frac{L + Q_C}{V_{tot}} \tag{4.8}$$

Relative percentage deviations of the first and second law efficiencies between the ideal case and the system steady state case are computed:

$$\delta_I = \frac{\eta_{I,id} - \eta_I}{\eta_{I,id}} 100 \tag{4.9}$$

$$\delta_{II} = \frac{\eta_{II,id} - \eta_{II}}{\eta_{II,id}} 100 \tag{4.10}$$

Such indicators are useful to highlight the configuration which undergoes the highest efficiency drop related to the system sizing.

- **System Dynamic state KPIs**. Such parameters are computed considering quantities integrated over cycle time:

$$\eta_{I,t} = \frac{L_t + Q_{C,t}}{Q_{H,t}} \tag{4.11}$$

$$\eta_{II,t} = \frac{L_t + E_{C,t}}{E_{H,t}} \tag{4.12}$$

$$ED_{m,t} = \frac{L_t + Q_{C,t}}{m_{tot}}; \quad ED_{V,t} = \frac{L_t + Q_{C,t}}{V_{tot}} \tag{4.13}$$

Relative percentage deviations of the first and second law efficiencies of the sized system between the steady state case and the dynamic state case are computed:

$$\delta_{I,t} = \frac{\eta_{I,t} - \eta_I}{\eta_I} 100 \tag{4.14}$$

$$\delta_{II,t} = \frac{\eta_{II,t} - \eta_{II}}{\eta_{II}} 100 \tag{4.15}$$

Further relevant parameters, i.e., mass and volume power densities PD_m and PD_V, which consider the cycle duration, are also computed. Indeed, aside from the efficiency and energy density as design criteria, the overall time needed to achieve the charging and discharging phases represents an important feature to consider in energy storage systems. The power density parameter adds such information to the energy density, and it can be defined as the mean power at which the system would operate if it were operating at constant power. Therefore, a high power density is achieved when a good trade-off between cycle time and energy density is accomplished.

$$PD_m = \frac{ED_{m,t}}{t_{cycle}}; \quad PD_V = \frac{ED_{V,t}}{t_{cycle}} \tag{4.16}$$

Where the cycle time is divided into reaction charge time $t_{c,r}$, sensible charge time $t_{c,sen}$, reaction discharge time $t_{d,r}$ and sensible discharge time $t_{d,sen}$.

$$t_{cycle} = t_{c,r} + t_{c,sen} + t_{d,sen} + t_{d,r} \tag{4.17}$$

5. Results

Main results obtained through the application of the model on the specified case, adopting different $SrCl_2$ 8-1 – HTM configurations are illustrated in the following chapter. In the first part the key performance indicators obtained in the steady state analysis are reported: regarding the ideal cycle, a brief discussion on the thermodynamic parameters of the cycle which influence its efficiency is carried out. Concerning the sized system, the impact of the thermal masses on the performance is investigated in detail to detect which properties of the salt-ammonia reactions and the cycle are most responsible for it. In the second section, the dynamic simulation for a selected $SrCl_2$ 8-1 – HTM configuration is carried out and the evolution in time of relevant quantities is illustrated and physically interpreted. Finally, in the last part, the performance evaluation of the different configurations in the dynamic state is accomplished, with the purpose to highlight which operating features are critical in determining high cycle times. A parametric analysis is then presented on a specific $SrCl_2$ 8-1 – HTM configuration, showing the effects of such features on the cycle time and useful outputs.

5.1 Steady state analysis

Figure 5.2 shows the values of first and second law efficiencies related to the ideal thermodynamic cycle for the selected HTMs and fixed LTM at $SrCl_2$ 8-1.

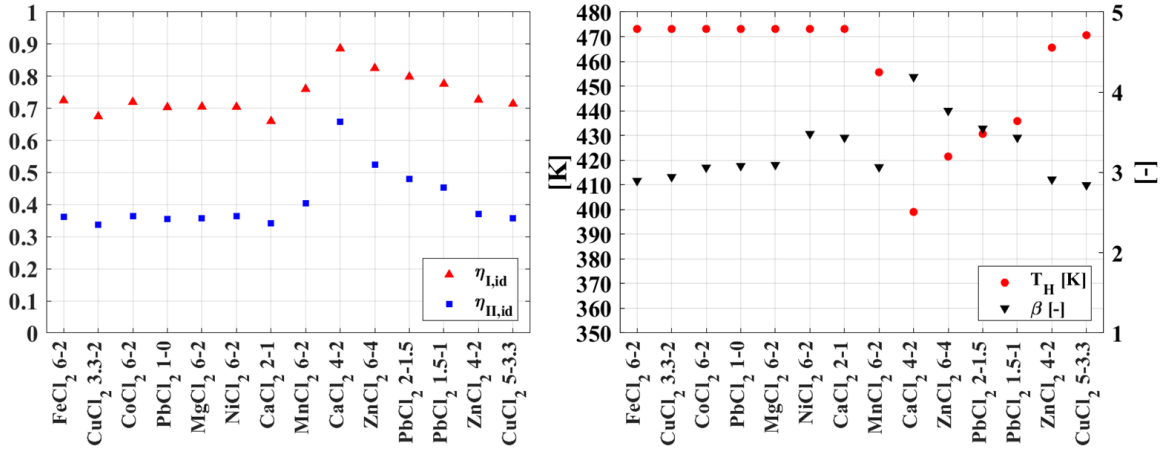

Figure 5.1: First law and second law efficiency for ideal cycle (left); hot source temperatures and pressure ratio for each selected HTM (right).

The configurations which appear to have higher performance are the ones operating at lower hot source temperature T_H and higher pressure ratio β. Such working conditions are beneficial from the point of view of the sensible heat consumption, in both the preheat and precool stages. Indeed, using a heat source at lower temperature results in minor temperature variation needed

in the preheat stage, hence lower specific heat input q_H. In addition, adopting both lower T_H and higher β ensures a reduced expander outlet temperature, which enables the LTM reactor to adsorb gaseous ammonia at a lower temperature. Thus, during the precool stage, the LTR undergoes smaller temperature variation and minor sensible heat release, resulting in a higher net specific refrigeration energy q_C.

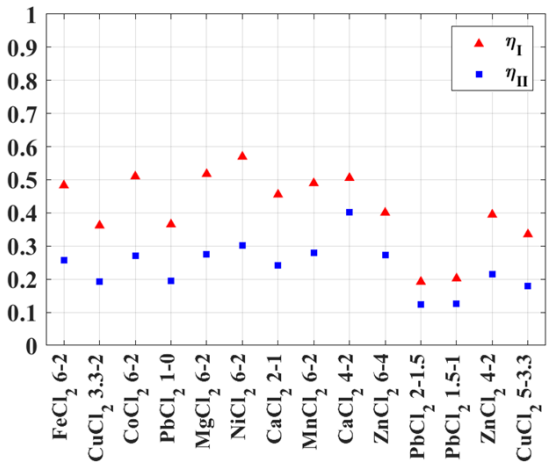

Figure 5.2: First law and second law efficiency for the system in steady state conditions.

Concerning the system steady state case (Figure 5.2), since the useful products of the cycle Q_C and L are fixed for each analyzed LTM-HTM working couple, the configurations with the higher efficiency values are characterized by the lower energy and exergy inputs, Q_H and E_H, respectively. Moreover, differently from the ideal case, it results that the performance values of the steady state case are not particularly affected by the operating hot source temperatures and pressure ratios. Such a feature is due to the fact that in the steady state case, the effective size of the reactors is considered, which has far more influence on the efficiency, with respect to the operating conditions of the thermodynamic cycle.

5.1.1 Energy density

The effect of the system's size on the performance can be seen also in Figure 5.3, representing the mass and volume total energy densities corresponding to the different $SrCl_2$ 8-1 – HTM configurations. For instance, the stoichiometric variation between higher and lower ammoniated salt $(\nu_2 - \nu_1)$ of the selected HTM reaction appears to have an influence on the values of the mass energy density. Indeed, a lower quantity of ammonia involved in the chemisorption reactions at fixed pure salt mass implies larger amounts of reactive material needed in the reactors to produce the energy needs Q_C and L.

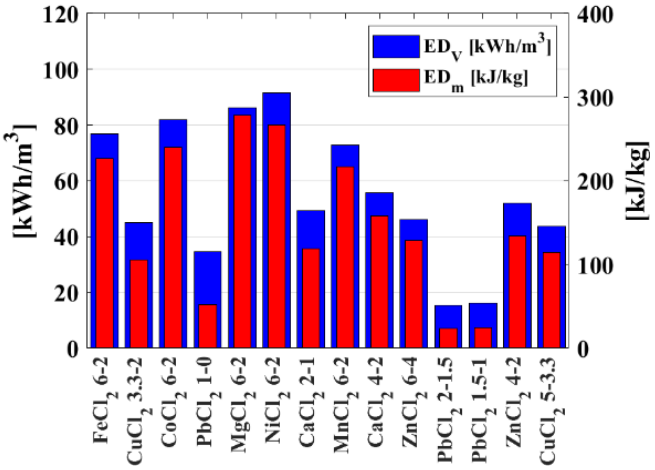

Figure 5.3: Total volume energy density ED_V and specific energy ED_m for each configuration in steady state.

Another parameter that affects the total energy density is the molar weight $\bar{M}_s$ of the pure salt used as a reactive medium: clearly adopting heavier material results in a lower energy density. For instance, the reactions $PbCl_2$ 1-0 and $CaCl_2$ 2-1 have the same stoichiometric variations $(\nu_2 - \nu_1)$, but, since lead has higher molar weight than calcium, the former HTM reveals lower mass energy density than the latter. It is worth noticing, that the specific adsorption capacity S_C is directly proportional to the ratio between $(\nu_2 - \nu_1)$ and $\bar{M}_s$ (equation 4.3). Hence, it is reasonable to presume that configurations adopting HTM with higher S_C would reveal higher energy densities. However, such assertation is valid only in the case all configurations adopt the same amount of ammonia $m_{NH_3,tot}$ that is exchanged between the two reactors, as it is shown in Figure 5.4.

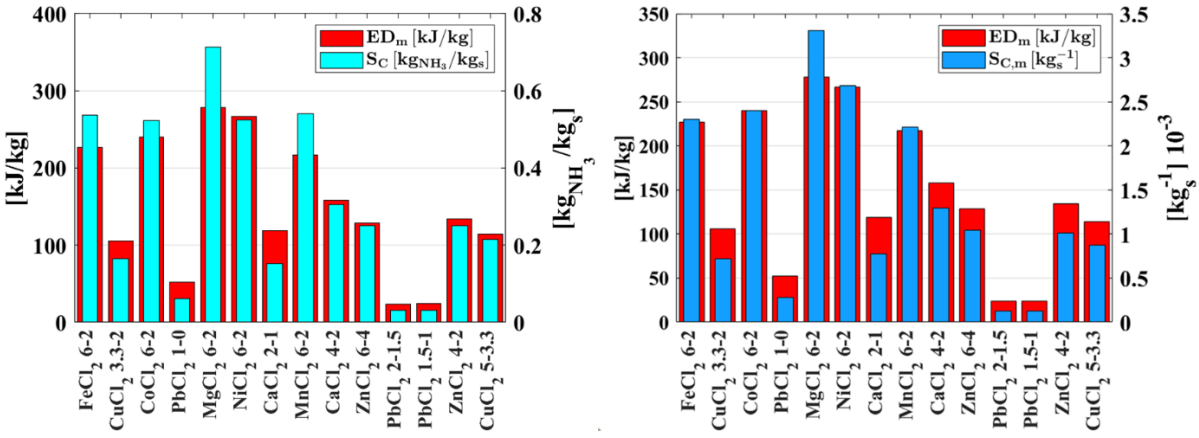

Figure 5.4: Total specific energy for each configuration, compared with the specific adsorption capacity (Left), and with specific adsorption capacity normalized to the mass of ammonia (right).

The left graph of the figure represents the mass energy density of the system for each selected HTM, compared with its specific adsorption capacity. It appears that not always the configuration with the higher S_C is characterized by a higher ED_m, as for $FeCl_2$ 6-2 and $CoCl_2$

6-2. On the other hand, let us consider the specific adsorption capacity normalized with respect the total amount of ammonia used in each configuration:

$$S_{C,m} = \frac{S_C}{m_{NH_3,tot}} \tag{5.1}$$

Observing the right graph of Figure 5.4, there is a clear correspondence between the values of mass energy density and normalized Specific adsorption capacity $S_{C,m}$. Therefore, it can be inferred that to identify the best solution in terms of high mass energy density, it is sufficient to detect the configuration with the highest specific adsorption capacity normalized to the amount of ammonia adopted. In other words, at a fixed amount of working fluid in the system, the highest mass energy density is obtained by adopting the HTM with the highest S_C.
The most performing configuration results to be the one adopting $NiCl_2$ 6-2 reactive mixture as HTM: first and second law efficiencies in the steady state case are 0.57 and 0.3 respectively, with the total volume energy density of 91.7 kWh/m^3 and mass energy density of 267 kJ/kg. However, such a selection does not result in high performance from the point of view of the power density and cycle time required, as illustrated in section 5.3.

5.1.2 The effect of thermal masses on the efficiency

As previously discussed previously (5.1), the thermal masses of the reactors have a major influence on the performance with respect to the operating hot source temperature and pressure ratio. This paragraph aims to highlight which properties of the salt-ammonia reactions and of the thermodynamic cycle are mostly responsible for high values of thermal masses, thus high efficiency losses between ideal and steady state case. To do so, let us consider the equations for the first law efficiency in the ideal ($\eta_{I,id}$, eq. 5.4) and steady state (η_I, eq. 5.5) cases, written as follows:

$$\eta_{I,id} = \frac{l + q_{C,r} - |q_{C,sen}|}{q_{H,r} + q_{H,sen}} \tag{5.2}$$

$$\eta_I = \frac{m_{NH_3,tot} l + m_{NH_3,tot} q_{C,r} - |Q_{C,sen}|}{m_{NH_3,tot} q_{H,r} + Q_{H,sen}} = \frac{l + q_{C,r} - \frac{|Q_{C,sen}|}{m_{NH_3,tot}}}{q_{H,r} + \frac{Q_{H,sen}}{m_{NH_3,tot}}} \tag{5.3}$$

Equations 5.2 and 5.3 prove that the deviation between $\eta_{I,id}$ and η_I are exclusively related to the sensible heat, both in the precool and in the preheat stage. The same consideration is valid for the second law efficiency. The expressions of the sensible heat can be further investigated:

$$Q_{H,sen} = TM_{S_2,h}(T_1 - T_5); \;\; Q_{C,sen} = TM_{S_2,l}(T_4 - T_3) \tag{5.4}$$

with $TM_{S_2,h}$ and $TM_{S_2,l}$ the thermal masses of the HTR and LTR at high ammoniation state (defined in equation 5.49), respectively. Thus, the sensible heat contribution can be written in the following general form:

$$Q_{sen} = TM\Delta T_{sen} \tag{5.5}$$

$$\Rightarrow Q_{sen} = (m_{S_2}c_{S_2} + m_{HX}c_{HX} + m_{EG}c_{EG})\Delta T_{sen} \tag{5.6}$$

Considering the definition of graphite ratio and metal ratio from equation 5.46 and 5.47.

$$\Rightarrow Q_{sen} = (m_{S_2}c_{S_2} + \tau m_s c_{HX} + \left(\frac{f_{EG}}{1-f_{EG}}\right)m_s c_{EG})\Delta T_{sen} \tag{5.7}$$

Rewriting the mass of the pure salt and the mass of the salt ammoniated at the higher state in terms of stoichiometric moles of exchanged ammonia (equation 3.8):

$$Q_{sen} = \left(\frac{n_{NH_3,tot}}{\nu_2-\nu_1}\bar{M}_{S_2}c_{S_2} + \tau\frac{n_{NH_3,tot}}{\nu_2-\nu_1}\bar{M}_s c_{HX} + \left(\frac{f_{EG}}{1-f_{EG}}\right)\frac{n_{NH_3,tot}}{\nu_2-\nu_1}\bar{M}_s c_{EG}\right)\Delta T_{sen} \tag{5.8}$$

Given the definition of specific heat of the highest ammoniate (equation 3.51) and using the definition of specific adsorption capacity S_C (equation 4.3):

$$Q_{sen} = \frac{m_{NH_3,tot}}{S_C}\Delta T_{sen}\left(\frac{\bar{c}_s}{\bar{M}_s} + \nu_2\frac{\bar{c}_{NH_3}}{\bar{M}_s} + \tau c_{HX} + \left(\frac{f_{EG}}{1-f_{EG}}\right)c_{EG}\right) \tag{5.9}$$

The above expression shows that three design parameters have a major impact on the sensible heat: the total cycle gaseous ammonia $m_{NH_3,tot}$, the temperature difference in the preliminary state ΔT and the specific adsorption capacity S_C of the salt-ammonia reaction used. The term composed by ΔT and S_C on the right-hand side of equation 5.9 can be defined as the sensible heat coefficient:

$$\lambda_{sen} = \frac{\Delta T_{sen}}{S_C} \tag{5.10}$$

The term in the brackets on the right side of the equation 5.9 has the units of a specific heat and can be defined as the equivalent specific heat of the reactor in the adsorbed state:

$$c_{TM} = \left(\frac{\bar{c}_s}{\bar{M}_s} + \nu_2\frac{\bar{c}_{NH_3}}{\bar{M}_s} + \tau c_{HX} + \left(\frac{f_{EG}}{1-f_{EG}}\right)c_{EG}\right) \tag{5.11}$$

Finally, the sensible heat contribution can be written as follows:

$$Q_{sen} = \lambda_{sen}m_{NH_3,tot}c_{TM} \tag{5.12}$$

Based on expressions 5.10 - 5.12, some considerations can be made regarding the properties which influence the thermal masses effects:

- Selecting the pure salt with higher specific adsorption capacity S_C allows to obtain a lower sensible heat contribution, improving the overall performance.
- Higher cycled ammonia $m_{NH_3,tot}$ will inevitably increment the amounts of reactive salts adopted in the reactors, increasing their thermal masses. On the other hand, reducing the cycled ammonia would also reduce the useful effects of cold and work production. Indeed, substituting equation 5.9 in the efficiency expression (eq. 5.3), the total cycled ammonia term is canceled, proving that such a design parameter does not affect the overall system first and second law efficiency.
- Reducing the preheat/precool temperature difference ΔT_{sen} results in positive effects on the sensible heat, thus on the performance. At fixed operating pressures, the reactive mixtures with a higher enthalpy of reaction ΔH_r, i.e. higher inclination of the equilibrium line, will result in lower ΔT_{sen}.
- At fixed metal ratio τ and graphite ratio f_{EG}, properties of the salt-ammonia reaction which influence the sensible heat for the different configurations are the pure salt specific heat c_s and the high ammoniation stoichiometric coefficient ν_2.

Figure 5.5 represents the values of λ_{sen} and c_{TM} for both HTR and LTR, in each selected configuration, together with the first and second law efficiency deviations δ between ideal and steady state case (eq. 5.9 and 5.10). It appears that there is a correspondence between the trend of the sensible heat coefficient evaluated for the HTR ($\lambda_{sen,h}$) and the trend of δ. Such a feature proves that $\lambda_{sen,h}$ is far more influencing on the overall side effects related to the thermal masses, with respect the same coefficient relative to the LTR ($\lambda_{sen,l}$). In fact, for each analyzed configuration the LTM undergoes a temperature variation during the precool phase which is smaller than the corresponding ΔT applied to the HTM during the preheat phase. Moreover, the adopted salt-ammonia reaction for each configuration in the LTR is $SrCl_2$ 8-1, which is the reaction characterized by the highest value of $S_C = 0.751\ \mathrm{kg_{NH3}/kg_s}$: as seen in equation 5.8, a high specific adsorption capacity is beneficial from the viewpoint of the reduction of the sensible heat consumption. The impact of the equivalent specific heat c_{TM} of the reactors on the performance loss results to be less relevant compared to the sensible heat coefficient. Indeed, c_{TM} is one or more order of magnitude smaller than λ_{sen} for each selected configuration.

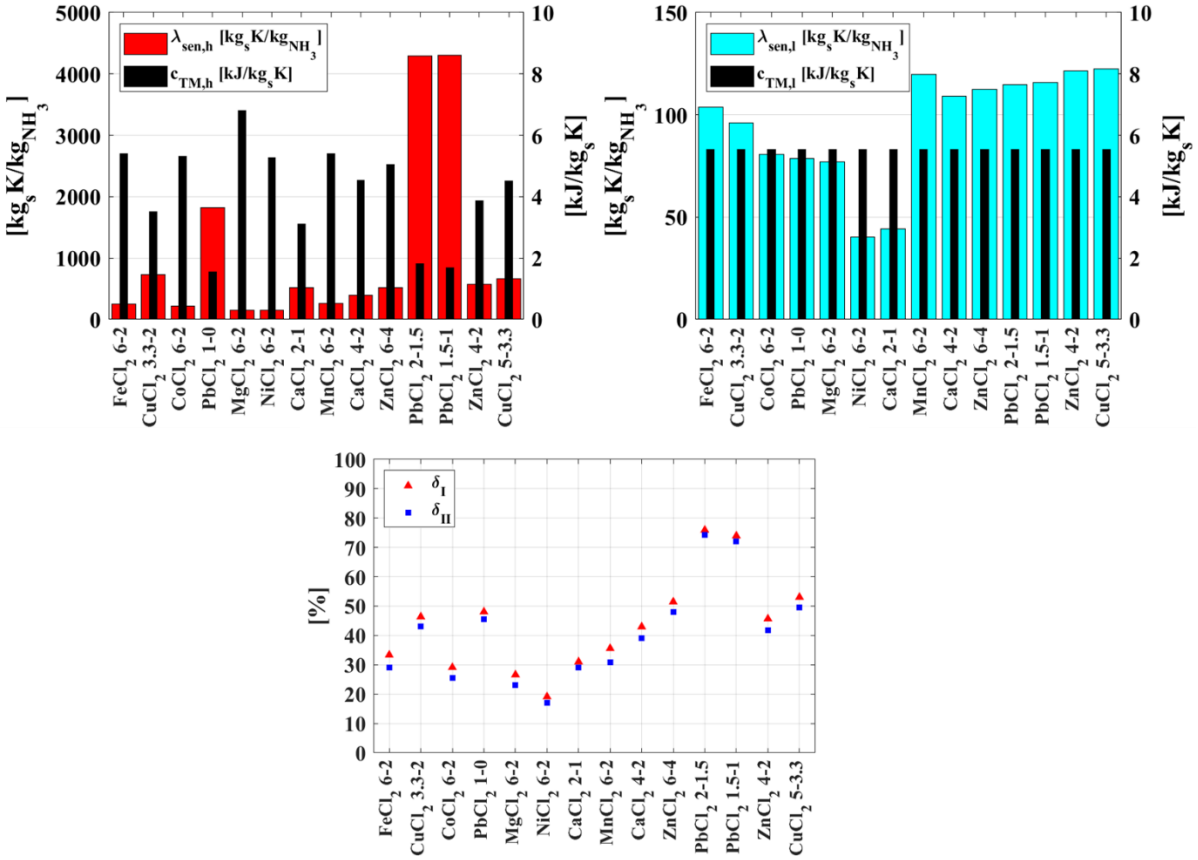

Figure 5.5: Values of λ_{sen} and c_{TM} for different selected HTM, relative to the HTR (left) and to the LTR (right), and performance efficiency percentage deviation between ideal and steady state case (bottom). Note the correspondence between the trend of the evaluated for the HTR $\lambda_{sen,h}$ and δ_I, δ_{II}.

In conclusion, some guidelines to design a TRSC configuration with the aim of minimizing the side effects of thermal masses on the performance are summarized:

- The most impacting parameter is λ_{sen} of the two reactors, hence it is favorable to adopt a system configuration in which such parameter is minimum. If the temperature during precool/preheat phase cannot be calculated, as rule of thumb the best salt-ammonia reactions to be used are the ones with highest specific adsorption parameter S_C.
- Designing a reactor with minimum equivalent specific heat c_{TM} reduces the effect of thermal masses and favors the efficiency. Nevertheless, the impact of such a parameter is negligible with respect to λ_{sen}.

5.1.3 Summary of results from steady state analysis

- The efficiency of the ideal cycle is thermodynamically favored by low hot source temperature and high pressure ratio, since minor sensible heat consumption is achieved.
- The efficiency of the sized system is affected more by the thermal masses, rather than by the operating hot source temperature and pressure ratio. The best HTM is $NiCl_2$ 6-2

with first and second law efficiency of 0.57 and 0.3 respectively; mass and energy density of 267 kJ/kg and 91.7 kWh/m^3 respectively.

- Higher mass energy density is accomplished by configurations adopting HTM with higher Specific adsorption capacity S_C, normalized to the total mass of cycled ammonia.
- Specific adsorption capacity is also the main intrinsic property that affects the impact of the thermal masses on the performance. To minimize the loss of efficiency caused by the effective size of the reactors it is convenient to adopt a configuration with the minimum value of coefficient λ_{sen}.

5.2 Dynamic state

After the steady state performance evaluation is performed for each suitable configuration, the dynamic model is used to obtain the evolution in time of relevant quantities, for a specific $SrCl_2$ 8-1 – HTM working couple. Hence the phenomena involved are explored in detail with the purpose to carry out a physical interpretation for the behavior of the reactors and of the working fluid, in each phase of the operating cycle. The selected $SrCl_2$ 8-1 – HTM configuration is the one adopting $MnCl_2$ 6-2 as HTM. Such a choice is made since the dynamic model has been validated for that specific working couple, ensuring more reliable results. Moreover, as it is shown in the next section, the $SrCl_2$ 8-1 – $MnCl_2$ 6-2 configuration reveals to be a favorable solution among the other options considering its high power density.

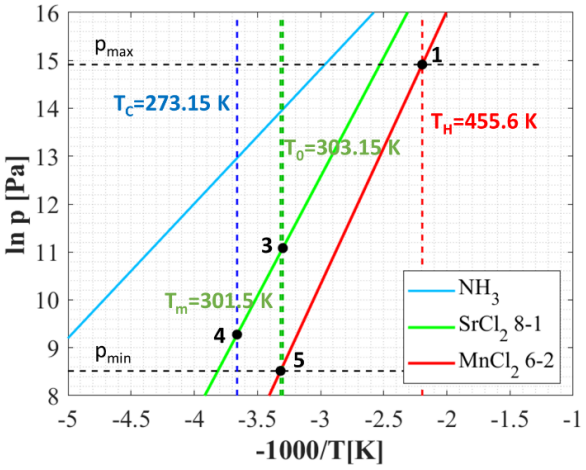

Figure 5.6: Operating conditions on Clapeyron diagram for the $SrCl_2$ 8-1 – $MnCl_2$ 6-2 configuration.

Taking Figure 5.6 as a reference, the operating conditions and working phases which constitute the cycle, are recapped as follows:

- *Preheat – Sensible charge phase:* HTR is heated from intermediate sink temperature T_m to hot source temperature T_H (from **5** to **1**) and LTR is heated from cold source temperature T_C to ambient sink temperature T_0 (from **4** to **3**).

- *Reaction charge phase:* Desorbed ammonia flows from HTR through scroll expander and is adsorbed in LTR (point **3**).
- *Precool – Sensible discharge phase:* LTR is cooled from ambient sink temperature T_0 to cold source temperature T_C (from **3** to **4**), while HTR is cooled from hot source temperature T_H to intermediate sink temperature T_m (from **1** to **5**).
- *Reaction discharge phase:* Ammonia desorbed from LTR is adsorbed in HTR (point **5**).

The simulations are stopped based on the following two criteria, depending on the cycle phase:

- For the intermediate steps, i.e. precool and preheat phases, the transient is ended as both reactive bed temperatures reach a deviation smaller or equal than 0.1 K with respect the source/sink temperature. For instance, the sensible charge phase ends when $T_H - T_{b,h} \leq 0.1$ K and $T_0 - T_{b,l} \leq 0.1$ K.
- Regarding the reaction phases, the transient ends as the global conversion ratio of both reactors reach a deviation smaller or equal than $5 \cdot 10^{-4}$ with respect the target value, i.e. 0 or 1. For instance, the reaction charge phase ends when $x_h - 0 \leq 5 \cdot 10^{-4}$ and $1 - x_l \leq 5 \cdot 10^{-4}$.

5.2.1 Preheat phase

During the preheat stage the two reactors are disconnected and heated to the corresponding target temperatures. While the heating occurs, the equilibrium condition is maintained in both reactors, hence the composition of the reactive mixture is invariant: the global conversion ratio of the two reactors is fixed at $x_h = 1$ for the HTR and at $x_l = 0$ for the LTR. Figure 5.7 shows the temperature evolution of the reactive bed, the metal composing the heat exchanger and the heat transfer fluid, relatively to HTR (subscript h) and LTR (subscript l).

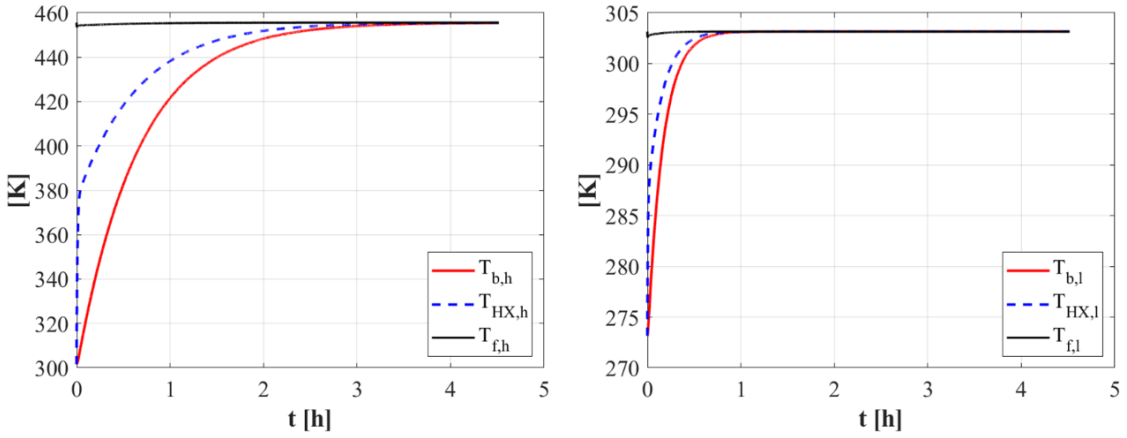

Figure 5.7: Temperature evolution of the reactive bed T_b, heat exchanger T_{HX}, and heat transfer fluid T_f during the preheat phase relatively to HTR (left) and LTR (right).

It can be inferred from the graph that HTR has larger a thermal mass compared to LTR. In fact, the bed material and the heat exchanger metal which compose the LTR need less time to reach

the desired temperature than the same components corresponding to HTR. The minor thermal mass of the LTR is due mainly to the following reasons:

- The LTR is in the desorbed state as it undergoes the heating process ($x_l = 0$), meaning that the reactive mixture is purely composed of strontium chloride ammoniated to the lower state $SrCl_2(NH_3)_1$. On the contrary, HTR is in the adsorbed state, hence it is purely composed of manganese chloride ammoniated at the higher state $MnCl_2(NH_3)_6$. Therefore, regardless of the different amounts of pure salt in the reactors, HTR has a mass higher than LTR by a quantity $m_{NH_3,tot}$.
- The higher specific adsorption parameter of the $SrCl_2$ 8-1 reaction with respect to $MnCl_2$ 6-2.

Another interesting feature worth noticing is the almost invariant evolution in time of the heat transfer fluid mean temperature T_f in both reactors. The physical reason for such a trend can be explained considering how the heat transfer fluid is modeled: the inlet fluid temperature is fixed at the desired source/sink temperature and the mass of the fluid in the reactor is as large as the quantity of metal. Hence, the high thermal inertia of the fluid together with the constant high energetic flow entering the reactor results in a negligible impact of the thermal power transfer on the mean temperature T_f. A slight variation of the fluid temperature only occurs at the beginning of the process, as the thermal power transferred is maximum.

5.2.2 Reaction charge phase

As the reactors are brought to the desired equilibrium temperatures at different pressure levels, the desorption/adsorption process of HTM and LTM is achieved by connecting them. As the valve is opened two constraint pressures are instantaneously imposed on the reactors, which evolve throughout the whole reactive process. Such pressures deviate from the equilibrium pressures of the salt-ammonia reactions corresponding to their temperatures (which is also varying in time), triggering the driving force necessary to achieve the decomposition/synthesis process.

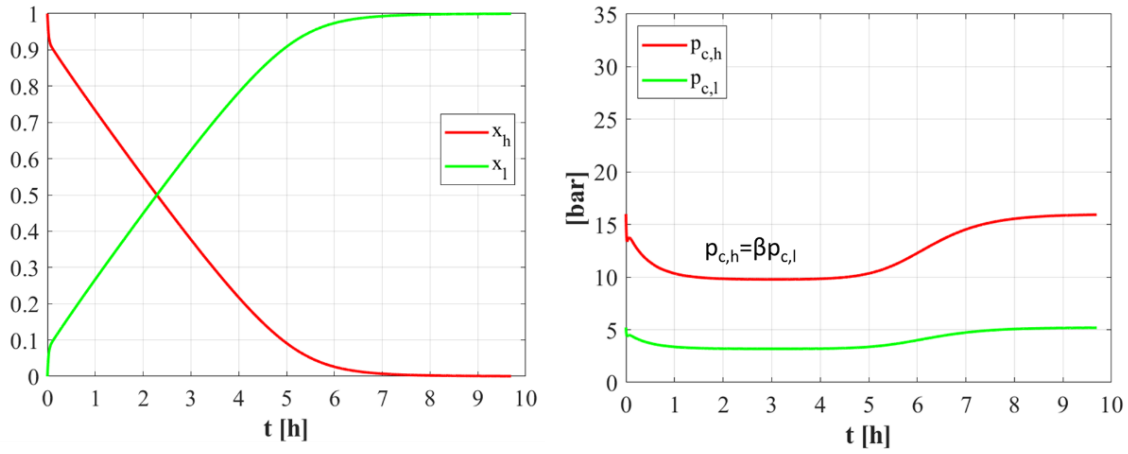

Figure 5.8: Evolution in time of the global conversion rate (left) and of the constraint pressure (right) during reaction charge phase. The red line refers to HTM, while the green line refers to LTM.

Figure 5.8 represents the evolution in time of the global conversion rates and of the non-equilibrium pressures of the reactors during the reaction charge phase.
It is interesting to notice that the global conversion rate trends of the two subsystems are exactly mirrored with respect to each other, meaning that the magnitude of the driving forces relative to HTR decomposition and LTR synthesis are equal. Hence, the two reactors are equally intense from the kinetic viewpoint and act as a single system, in which no component prevails to the other. Such a feature is strictly related to the design of the reactors based on the cycled ammonia $m_{NH_3,tot}$: the amounts of reactive mixtures in HTR and LTR have been properly sized in order to obtain the same stoichiometric quantity of ammonia to be desorbed/adsorbed in the reactors. The behavior of the system would be different if, for instance, the LTM would be oversized: the quantity of ammonia that the LTR could adsorb would be larger than the mass of ammonia desorbed by the HTR. Thus, the LTR would be characterized by stronger kinetics (equations 3.93 and 3.94) and would impose its driving force on the coupled reactions in the system. An example of such a case is illustrated in the next paragraph (5.2.3), in which the reaction charge phase is represented on the Clapeyron diagram. Concerning the non-equilibrium pressure evolution, it can be seen that $p_{c,l}$ is scaled with respect to $p_{c,h}$ by the factor $\beta = 3.07$. Indeed, the scroll expander is modeled as a simple constrain between the non-equilibrium pressures of the two reactors, given by the pressure ratio itself.
Three separated time intervals can be identified for both global conversion rate and constraint pressure trends: at the beginning of the process, a rapid variation occurs because of the maximum driving force imposed on the reactors after their instantaneous connection. The reactors get then stabilized in the second interval, during which the driving force and the constrain pressures are constant. Finally, as the HTM decomposition and LTM synthesis are almost complete, the driving force drops, causing the coupled reactions to slow down. The same time intervals can be detected in the trend of the mass flow rate and the power produced by the expander shown in Figure 5.9.

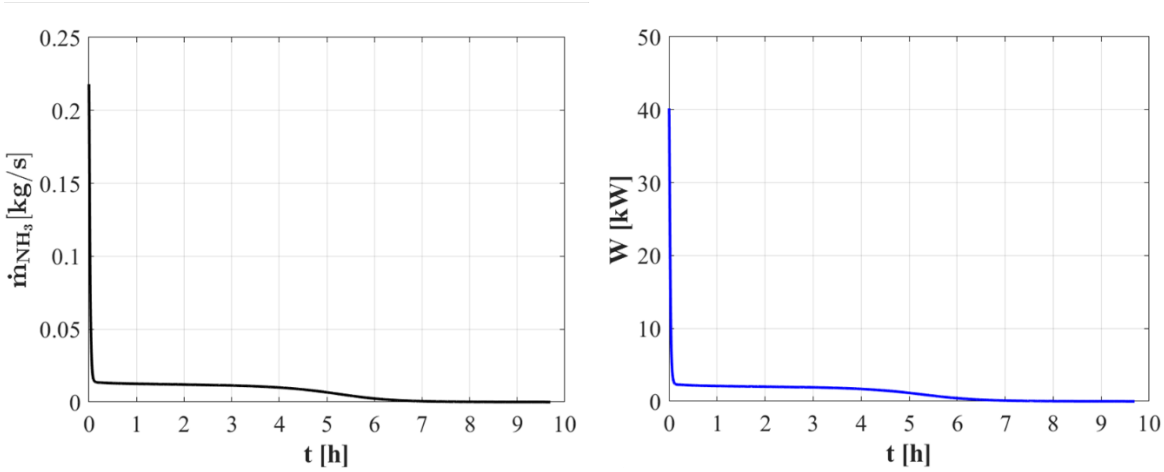

Figure 5.9: Evolution in time of the ammonia mass flow rate from HTR to LTR (left) and scroll expander power (right).

It is worth noticing that $\dot{m}_{NH_3}$ and W reveal the same trend, proving that the specific work produced is almost invariant during the reactive process. In other words, since the pressure ratio is assumed constant, the enthalpy difference between expander inlet and outlet is not drastically affected by the transformations occurring in the two reactors.
The last variable that needs to be discussed, relatively to the reaction charge phase is the temperature. Taking Figure 5.10 as a reference, it can be observed that the temperature variations occurring in the reactors are associated with the heat transferred during the corresponding chemisorption reactions.

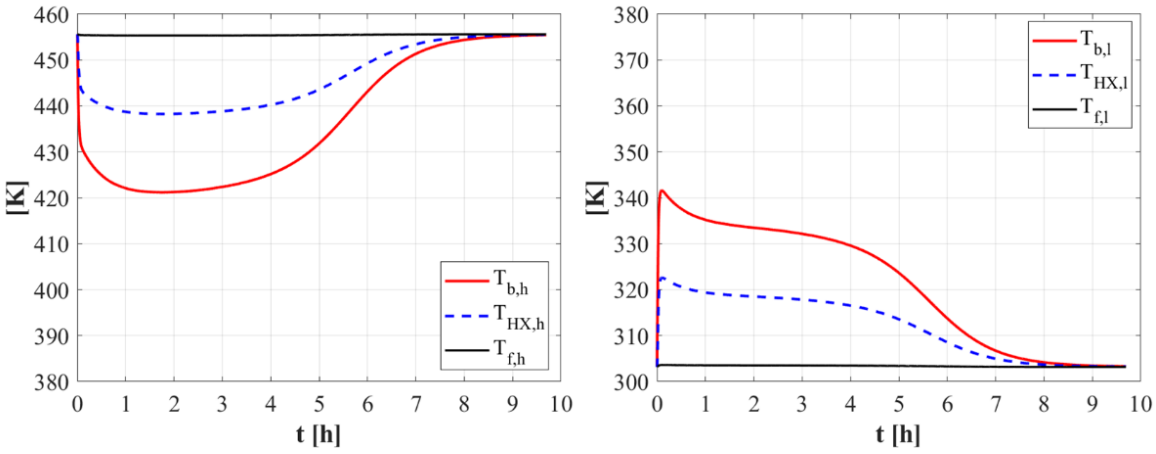

Figure 5.10: Temperature evolution of the reactive bed T_b, heat exchanger T_{HX}, and heat transfer fluid T_f during the reaction charge phase, relatively to HTR (left) and LTR (right).

Indeed, the HTR is undergoing endothermal desorption, which thermodynamically corresponds to a thermal sink located within the reactor. Hence, desorption causes the HTR temperature to decrease until a balance between heat supplied by the HTF and heat required by the reaction is achieved. On the other hand, the LTR is undergoing exothermal adsorption, meaning that an internal energy source causes the reactor temperature to steeply increase at the beginning of the process when the driving force is higher. After the temperature peak, the thermal energy absorbed by the HTF overcomes the heat generated by the synthesis reaction and LTR is cooled back to its beginning state. The entity of the temperature variation clearly depends on $\Delta\bar{h}_r$ of the considered salt-ammonia reaction: the higher temperature variation of the HTR compared to the LTR is related to the larger heat of reaction of $MnCl_2$ 6-2 with respect to $SrCl_2$ 8-1, which have a value of $\Delta\bar{h}_r$ equal to 47.4 kJ/mol and 41.4 kJ/mol, respectively.
Regarding precool and reaction discharge phases, similar considerations on the transient behavior during the preheat and reaction charge phases can be made. The only differences are:

- The reactors swap their role, meaning that the LTR acts as vapor generator, while the HTR becomes the vapor absorber.
- During desorption/adsorption phase a single non-equilibrium pressure is imposed on both reactors, since the expander is bypassed.

The results in terms of evolution in time related to the discharge phase are shown in the appendix.

5.2.3 Representation on the Clapeyron diagram

The evolution in time of temperature and pressure of HTR and LTR during the reaction charge phase is represented on the Clapeyron diagram in Figure 5.11.

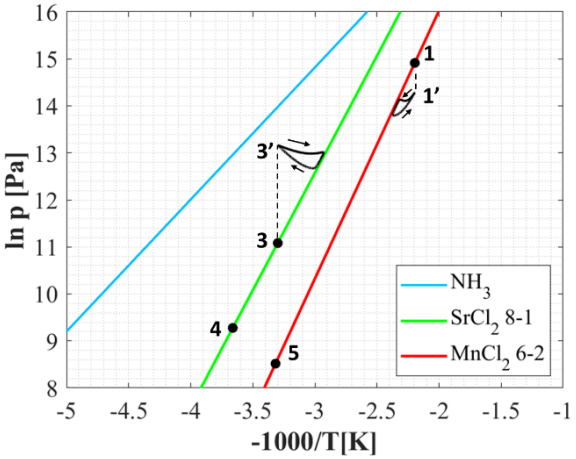

Figure 5.11: Reaction charge phase on the Clapeyron diagram.

The three different time intervals addressed previously (5.2.2) can be observed: as the reactors are connected, the constraint pressures $p_{c,h}$ and $p_{c,l}$ are instantaneously imposed, i.e. transformations (**1-1'**) for HTR and (**3-3'**) for LTR. Subsequently, the reactors rapidly evolve towards the equilibrium lines of the corresponding solid/ammonia reactions. Hence, the driving force of the simultaneous reactions lowers its intensity, until new equilibrium conditions for both reactors are achieved (**3'** and **1'**) and the reaction charge phase is ended. As previously mentioned (5.2.2), the reason for this behavior is that HTR and LTR are equally sized in order to adsorb/desorb the same stoichiometric quantity of ammonia $m_{NH_3,tot}$, and no reactor imposes its driving force on the other. The behavior of the system is different in the case the one reactor is oversized or undersized compared to the other. For instance, let us assume to size the reactors, imposing the following relation:

$$m_{NH_3,tot,l} = \frac{4}{3} m_{NH_3,tot,h} \qquad 5.13$$

Thus, the maximum quantity of gas that the LTR can adsorb/desorb is 4/3 times larger than the total amount of gas the HTR is capable to manage. In other words, LTR is oversized with respect to HTR. Figure 5.12 shows the global conversion rates and the reaction charge time on the Clapeyron diagram in this specific case. It can be noticed that, while the HTR is completely desorbed at the end of the charge phase, LTR has still the potential to adsorb gaseous ammonia (x_l tends to 0.75 instead of 1). Consequently, LTR kinetics is the prevailing driving force on the coupled reactions in the system. Indeed, as it can be inferred by the Clapeyron diagram, the reaction charge phase ends with the LTR at equilibrium conditions corresponding to $SrCl_2$ 8-1, i.e. with $p_{c,l} = p_{eq,l}(T_3)$.

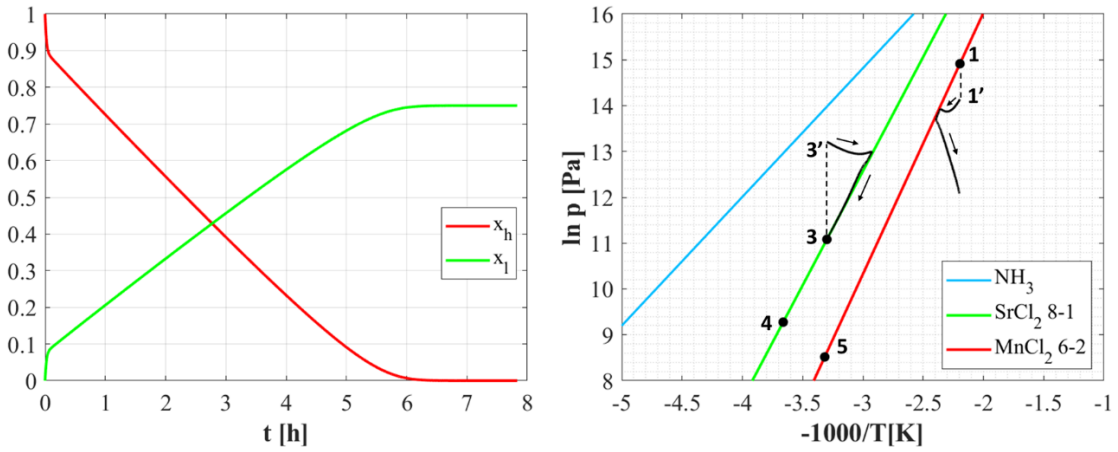

Figure 5.12: A case study in which LTR is oversized compared to HTR. Evolution in time of global conversion rates of HTR and LTR (left) and reaction charge phase on the Clapeyron diagram (right). LTR imposes its kinetics on HTR.

On the other hand, the HTR is driven by LTR until it reaches a final condition out of the equilibrium line corresponding to $MnCl_2$ 6-2, i.e. with $p_{c,h} = \beta p_{c,l}$. In conclusion, two scenarios can be expected when coupling two reactors in a thermochemical resorption system through the dynamic model:

- If a reactor is oversized with respect to the other, it imposes its equilibrium condition to the overall resorption system, because of its more impactful driving kinetics.
- If the reactors are sized in a such way that they have the potential to adsorb/desorb the same amount of gaseous working fluid, no reactor imposes its driving force to the other. Instead, the system evolves towards a new equilibrium condition.

5.2.4 Energy stored and cogeneration of power and cold

The evolution of the cumulated energy quantities in time, relative to the charge phase and discharge phase is illustrated in Figure 5.13.

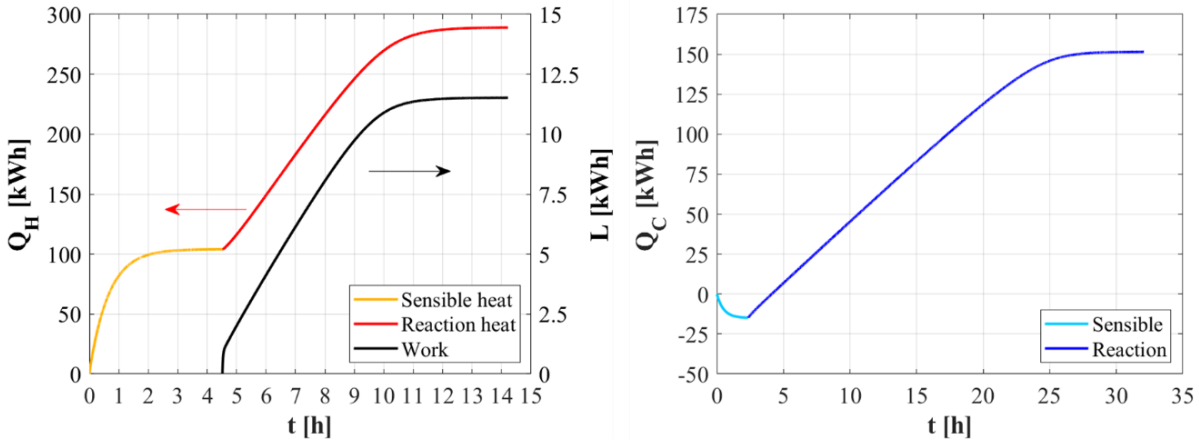

Figure 5.13: Evolution in time of stored energy and work produced during the charge phase (left); evolution in time of the cold production during the discharge phase (right).

A relevant aspect to highlight is the larger time needed to achieve the reactive phase with respect to the sensible heat transfer phase during both charge and discharge. Thus, it can be observed that reaction kinetics represents a more significant bottleneck to the completion of the overall cycle, than the thermal masses. Detailed analysis on the cycle time of the several configurations defined in the previous chapter is carried out in section 5.3 with the aim to identify the design parameters which mostly affect such a high duration of the reactive phases.
Concerning the sensible phases, the effect of thermal masses is far more impactful in the preheat stage rather than during precooling, given that the HTR adsorbs about 100 kWh, while LTR needs to release less than 25 kWh: indeed, the related values of the sensible heat coefficient λ_{sen} for $SrCl_2$ 6-2 and $MnCl_2$ 6-2, are about 110 kg_sK/kg_{NH_3} and 260 kg_sK/kg_{NH_3} respectively (Figure 5.5). Moreover, the cold production results to be larger than the design value $Q_C = 120$ kWh, set in the steady state case. The reason is linked to the practical need to bring the reactors at different pressure levels before desorption/adsorption addressed in the dynamic study: the sensible heat contribution in the discharge phase evaluated in the dynamic case results to be lower than the same contribution relative to the steady state case, due to the smaller temperature variation achieved (section 4.2.2, Figure 4.3). As a consequence, a larger net refrigeration effect is obtained. The impact of such an additional feature on the results in the dynamic case is addressed in detail in the following section, where the corresponding KPIs for each admissible configuration are visualized and commented.

5.3 Dynamic state performance evaluation

First and second law efficiencies resulting from the dynamic analysis (4.3) have been computed for each $SrCl_2$ 8-1-HTM configuration and compared with the values obtained in the steady state case (Figure 5.14).

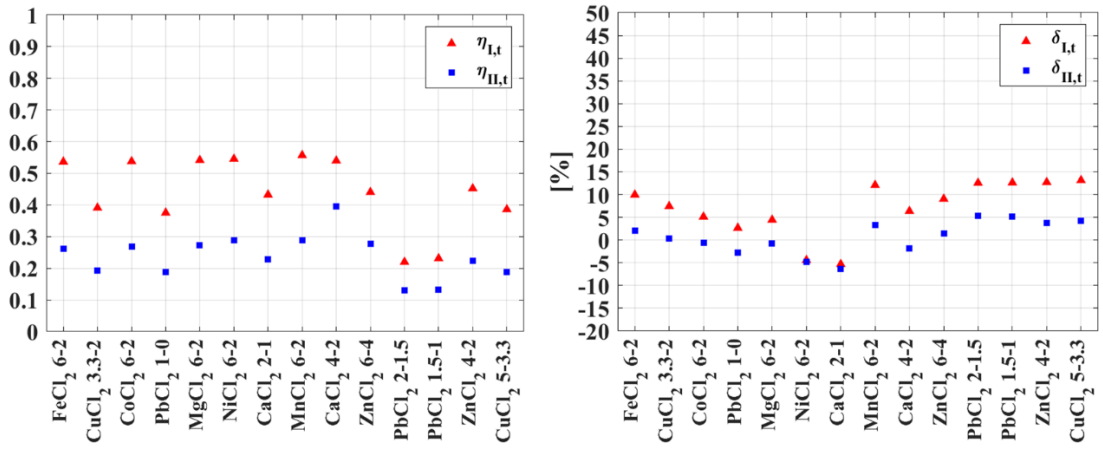

Figure 5.14: First and second law efficiencies related to the dynamic state analysis (left) and percentage deviations with respect to the steady state case (right).

The slight discrepancy, lower than 15% for each HTM evaluated, proves that the results are consistent from the energetic point of view. As already discussed previously (section 5.2.4), the main reason for such a deviation is related to the addition of practical conditions regarding kinetics in the dynamic study of the cycle, thus the different pressure levels of the reactors before synthesis/decomposition steps, with respect to the steady state case, as shown in Figure 5.15.

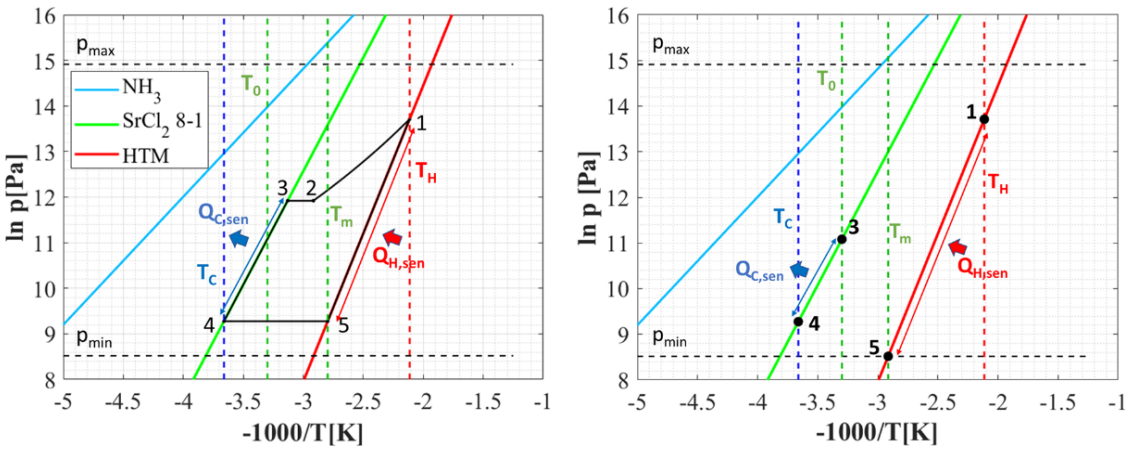

Figure 5.15: Sensible heat contributions in steady state (left) and dynamic state (right).

Before the reaction occurring during the charge phase, the pressure difference between HTM and LTM in the dynamic case is larger compared to the steady state case (points 1 and 3). On the other hand, before the discharge phase the HTM reactor is brought to a lower pressure with respect to the LTM reactor in the dynamic case, while in the steady state the reactors are at same pressure (operating points 4 and 5). Consequently, in the dynamic state the sensible heat contribution $Q_{H,sen}$ in the preheat stage is higher due to higher temperature raise achieved, while the sensible heat contribution $Q_{C,sen}$ in the precool stage results to be lower. The former feature causes an efficiency decrease of the cycle in the dynamic analysis, while the latter one contributes to increase it. It is interesting to notice that some configurations are affected by a negative deviation from the steady state results, while for others the performance increases. System configurations presenting a dynamic efficiency drop with respect to the steady state case are therefore characterized by an increment of $Q_{H,sen}$ which overcomes the effect of the reduction of $Q_{C,sen}$.

5.3.1 Cycle time

The dynamic analysis also provides information regarding the cycle duration related to each system configuration. Figure 5.16 shows the total cycle time, composed by its different contributions.

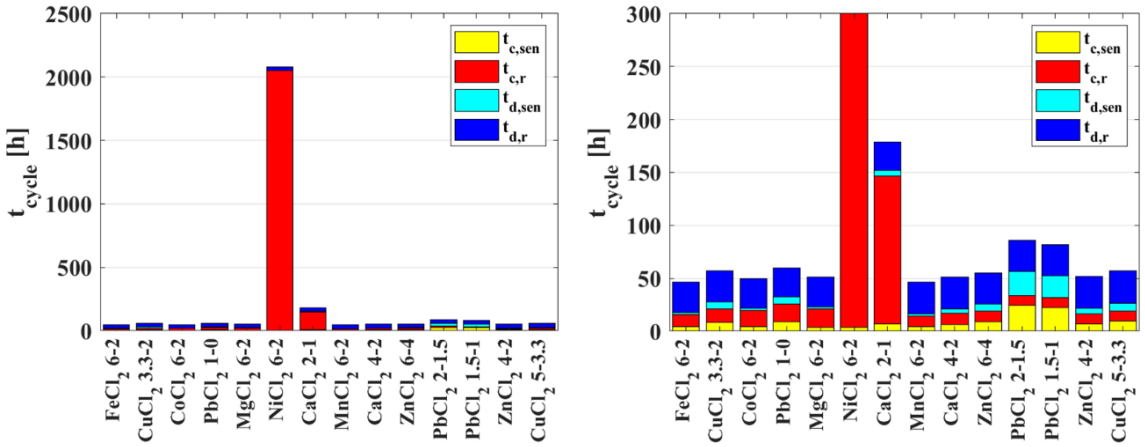

Figure 5.16: Cycle time for each $SrCl_2$ 8-1 – HTM configuration.

Several observations can be made in terms of how the cycle characteristics and salts properties affect the cycle duration:

- The time needed to complete the sensible heat transfer in both charge and discharge phases is the largest for the configurations with the largest thermal masses effects ($PbCl_2$ 2-1.5 and $PbCl_2$ 1.5-1 as HTM): the higher the sensible heat coefficient λ_{sen}, the higher the energy consumed/released by the reactor to achieve the preheat/precool temperature variation.
- The discharge desorption/adsorption phase providing the cooling effect has almost the same duration for each configuration. The main reason is that for each selected HTM the pressure difference imposed by the two reactors after the precool phase is the same, corresponding to $(p_4 - p_5)$ in the right graph of Figure 5.15. Physically, this implies that, as the valve is opened to trigger the discharge reaction, the non-equilibrium conditions imposed on the reactors are comparable for each HTM selected, causing in fact similar reactions kinetics.
- The duration of the charge desorption/adsorption phase, providing the heat storage and the work production, is related to the choice of the expander pressure ratio β, with respect to the maximum achievable pressure ratio β_{max}: configurations undergoing longer reaction charge phase are characterized by a value of β closer to β_{max} (e.g. $NiCl_2$ 6-2*)*. Such feature is explored more in depth from the physical point of view in paragraph 5.3.2.

After computing the total cycle time, it is possible to obtain the power density for each configuration (Figure 5.17). It is interesting to notice that, although a specific selected HTM might result in high performance from the energetic viewpoint in the steady state evaluation, it can reveal a drastic deficiency in terms of cycle time. For instance, it is the case of the configuration using $NiCl_2$ 6-2, with a volume energy density of about 91.7 kWh/m^3 and power density of only 0.04 kW/m^3, revealing to be the worst choice in terms dynamic performance.

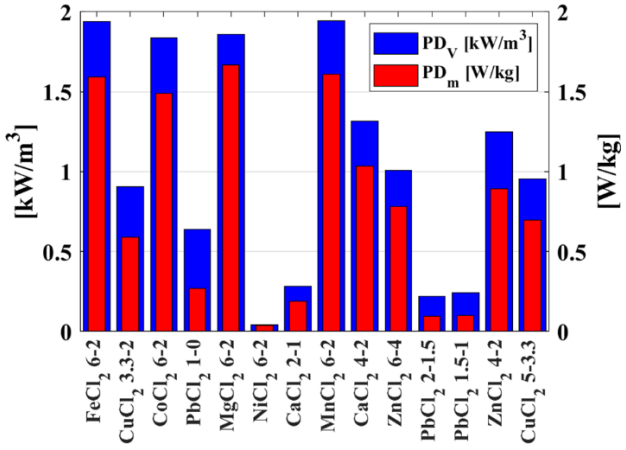

Figure 5.17: Power density for each $SrCl_2$ 8-1 – HTM configuration. $NiCl_2$ 6-2 appears to be the worst choice in terms of dynamic performance.

5.3.2 Influence of the pressure ratio on the reaction charge time

Two upper limits for the pressure ratio are to be considered while designing a TRSC: the first is related to the fact that the outlet pressure of the expander must be lower than the ammonia dew point at the corresponding temperature, in order to avoid phenomena of pitting corrosion of the materials composing the blades. The second upper limit is linked to the ambient sink temperature T_0:

$$\beta_{max} = \frac{p_{eq,h}(T_H)}{p_{eq,l}(T_0)} \qquad 5.14$$

The scroll expander outlet pressure must be higher than the equilibrium pressure of LTM corresponding to temperature T_0. Indeed, if this last condition is not fulfilled, it would cause the LTR to release adsorption heat at temperature lower than T_0, making the heat transfer from the reactor to the ambient sink physically impossible. To better understand how the value of scroll expander pressure ratio with respect to β_{max} influences the reaction charge time, let us consider the Clapeyron diagram for two different system configurations (Figure 5.18). Considering the case in which $NiCl_2$ 6-2 is adopted, the fixed pressure ratio has a value comparable to β_{max}. Since such a high pressure jump is requested between the expander's inlet and outlet, the non-equilibrium pressures imposed at the two reactors at the beginning of the reaction, i.e. $p_{c,h}$ at the HTR and $p_{c,l}$ at the LTR, can only slightly deviate from the equilibrium line at the corresponding temperature. This small deviation does not favor the reaction kinetics in the reactors, causing the reaction time to rise dramatically. On the contrary, in the case of $MnCl_2$ 6-2 configuration, the value of β is much smaller than the maximum acceptable value. Therefore, the non-equilibrium pressures imposed at the reactors have room to considerably deviate from the equilibrium conditions at the corresponding temperature, allowing to obtain a high driving force promoting the reactions.

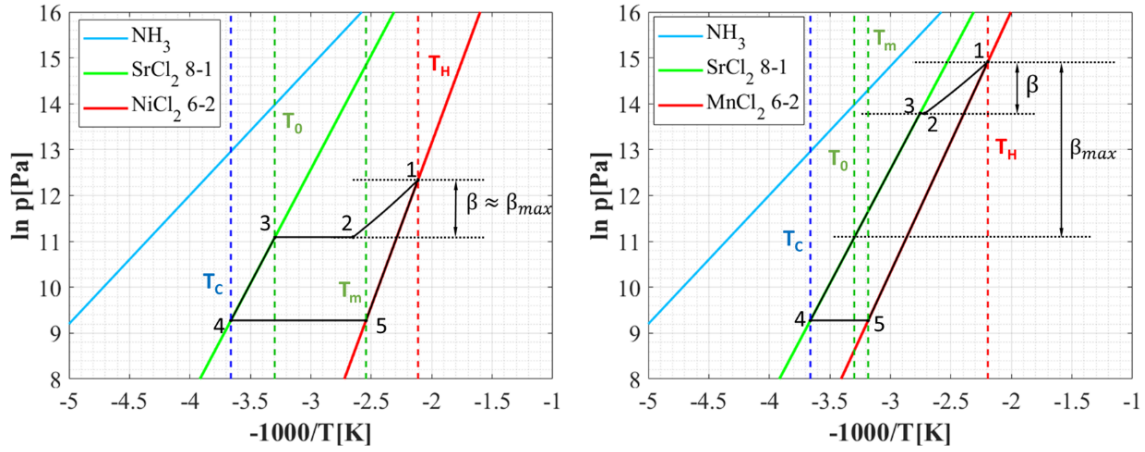

Figure 5.18: Clapeyron diagrams in the case of selecting the configurations with $NiCl_2$ 6-2 (left), and $MnCl_2$ 6-2 (right) as HTM.

In general, we could say that: the closer is the pressure ratio with respect to the maximum achievable pressure ratio β_{max} for the specific configuration, the smaller will be the deviation imposed to the two salt-ammonia reactions with respect to their equilibrium lines, when the valve is opened and the reactors are connected. This inevitably causes a weaker driving force for the chemical reactions of desorption in the HTR and adsorption in the LTR, thus larger time will be needed to complete the whole reactive charge phase.
The evolution of the pressure in time during decomposition/synthesis in the charge phase is shown in Figure 5.19 for the two configurations.

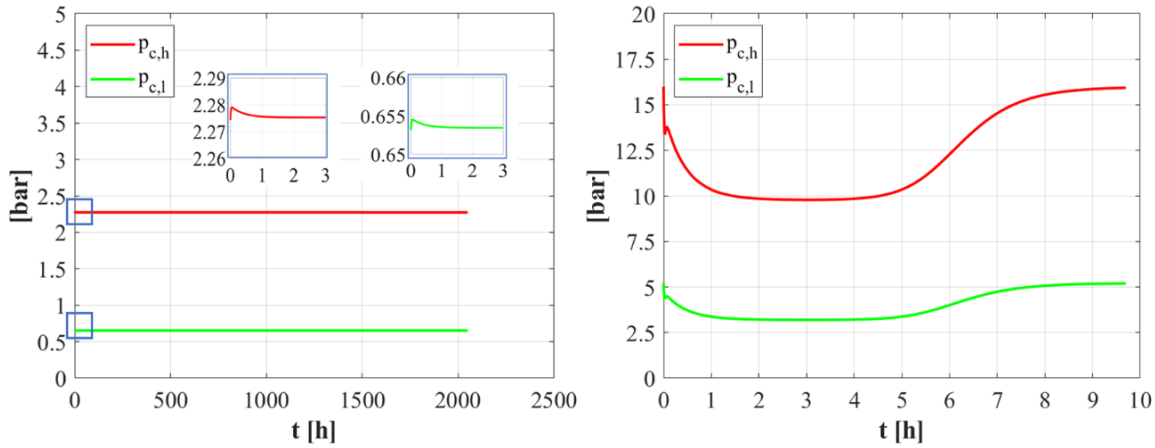

Figure 5.19: Evolution of the pressure in the two reactors in the case $NiCl_2$ 6-2 (left) and $MnCl_2$ 6-2 (right) as selected HTR.

It is interesting to notice that in the case of $NiCl_2$ 6-2 as selected HTM the pressures in the reactors result to have a constant trend in time: since the pressure deviations imposed to the reactors are very modest, it is reasonable to expect that the non-equilibrium pressures get stabilized at the early stages of the reaction, after slight variations two/three orders of magnitude

smaller than bars. On the other hand, in the case of $MnCl_2$ 6-2, the reactors undergo high deviation from the equilibrium pressure as the valve is opened, causing intense variation of the pressure trend, until the reaction is ended.
Since several potential system designs can exist, depending on the selection of LTM-HTM couples and operating conditions, it is useful to define a proper parameter, able to identify a priori whether the implementation of a scroll expander for a certain configuration would be critical from the point of view of the charge decomposition/synthesis time. We therefore define the expander coefficient ξ as:

$$\xi = \frac{\beta - 1}{\beta_{max} - 1} \tag{5.15}$$

When ξ tends towards 1, the charge reaction time tends to mathematical infinity, since β would tend to β_{max}. In fact, when $\beta = \beta_{max}$, no pressure deviation with respect to the reactions equilibrium lines are achievable and the decomposition/synthesis would not occur. On the other hand, as ξ is equal to 0, the reaction time is at its minimum value, corresponding to a configuration in which the expander is bypassed, i.e. Simple Resorption ($\beta = 1$). In Figure 5.20 the values of the coefficient ξ are represented for the different analyzed $SrCl_2$ 8-1-HTM configurations, together with the charge reaction times $t_{c,r}$.

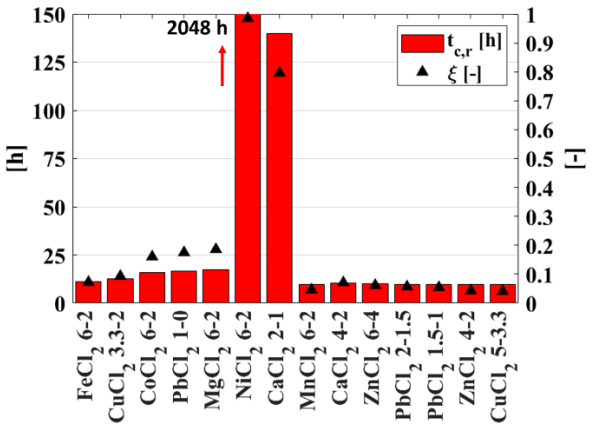

Figure 5.20: Expander coefficient for each $SrCl_2$ 6-2 – HTM configuration compared to the corresponding charge reaction time.

The fact that the trend of ξ well resembles the trend of the reaction charge time proves the relevant impact of the selection of the pressure ratio on the reaction kinetics. The lowest reaction time is obtained adopting the configuration with $CuCl_2$ 5-3.3 as HTM, with a value of 9.5 h, corresponding $\xi = 0.0408$.

5.3.3 Parametric analysis: reaction charge time

A specific system configuration with fixed a $SrCl_2$ 8-1-HTM working couple has been investigated through the dynamic model with the aim to highlight how the choice of the pressure ratio affects the reaction charge time $t_{c,r}$ and the work produced L_t. The selected HTM is $MgCl_2$ 6-2, which is one of the most performing reactive material from the power density viewpoint. The operating conditions are the same as defined in chapter 4, with the only difference that in this case several values of β are set as inputs to the model, while the produced work is calculated a posteriori. The values of β go from 1 to β_{max}, which for this specific configuration is equal to 12.3. Figure 5.21 represents the evolution of the global conversion rate x_h related to the HTM, undergoing desorption for the selected values of pressure ratio. It is noteworthy that the reaction charge time increases more significantly as the chosen pressure ratio approaches β_{max}, i.e. as the expander coefficient ξ tends to 1. This is coherent with what is mentioned in the previous paragraph: since the desorption/adsorption between HTM and LTM would not occur in the case of $\beta = \beta_{max}$, meaning that the reaction time would be infinite, we can expect that $t_{c,r}$ increases exponentially as the pressure ratio increases, with the upper limit tending to infinite as β tends to β_{max}.

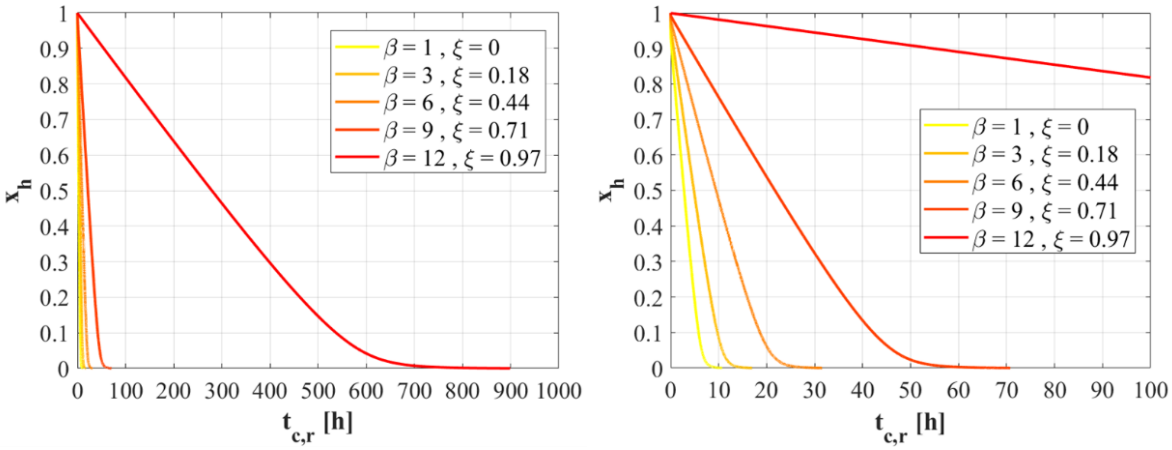

Figure 5.21: Evolution in time of HTM global conversion rate during the reaction charge phase for $SrCl_2$ 6-2-$MgCl_2$ 6-2 configuration, with different values of β.

Such a feature is to be found in Figure 5.22 as well, where the work production and $t_{c,r}$ are investigated as a function of β. It results that, while the raise of work production gets slower as the pressure ratio tends to its maximum value, the reaction charge time curve gets steeper with an exponential trend.

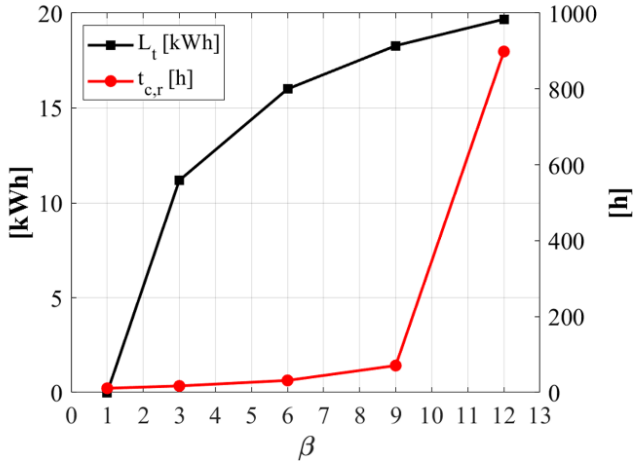

Figure 5.22: Reaction charge time and work production for $SrCl_2$ 8-1- $MgCl_2$ 6-2 configuration and different values of β.

This behavior implies that for a generic system composed of two thermochemical reactors connected via an expander, selecting a configuration with the maximum pressure ratio is not the most beneficial design. Indeed, the increase of desorption/adsorption phase duration obtained when a higher pressure ratio is selected is much more impactful than the raise of the potential work that can be produced. In other words, the drawbacks related to the selection of pressure ratio close to its maximum achievable value, in terms of reaction time, remarkably overcome the potential benefits that would be accomplished in terms of work production. For instance, as shown in Figure 5.22, the work production rise corresponding to an increase of pressure ratio from 9 to 12, is in the order of kWh, while the increment of time is in the order of $10^2\ h$. Therefore, depending on the specific application purposes, a suitable trade-off between useful work production and requested charge time should be envisioned to properly select the scroll expander pressure ratio.

5.3.4 Parametric analysis: reaction discharge time

As described in Section 5.3.1 the decomposition/synthesis reaction time during the discharge phase $t_{d,r}$ does not change considerably for the different selected HTM. Since the pressure difference $\Delta p_d = p_4 - p_5$ between the two reactors (right graph of Figure 5.15) is fixed, the non-equilibrium pressures imposed on them as the valve is opened result in similar reaction kinetics, and therefore similar reaction time for each configuration. It seems reasonable to presume that as such pressure difference changes, the reaction discharge times will be affected. Specifically, it can be expected that as Δp_d increases a higher deviation from the equilibrium lines can be achieved in both the reactors upon valve opening, meaning that a higher driving force for the chemical reactions will be achieved. On the contrary, if Δp_d is set to 0, the two reactors are at the same equilibrium pressure before connecting them, implying that when the valve is opened, no deviating pressure can be imposed, preventing the desorption/adsorption reactions from occurring. From the mathematical viewpoint, this means that as Δp_d tends to 0

the discharge reaction time tends to infinite. The $SrCl_2$ 8-1 - $MgCl_2$ 6-2 configuration has been again chosen to explore the described physical phenomenon, by varying the pressure difference Δp_d, keeping the other operating conditions fixed. Specifically, the operating point **5** has been kept at the minimum admissible pressure $p_{min} = 0.05\ bar$ and at the corresponding equilibrium temperature, while the operating point **4** is varied, shifting it along the LTM equilibrium line. Hence the cold source temperature T_C is necessarily altered, affecting the quality of the refrigeration. In Figure 5.23 the evolution in time of the LTM global conversion is shown for the selected pressure variations and cold source temperatures.

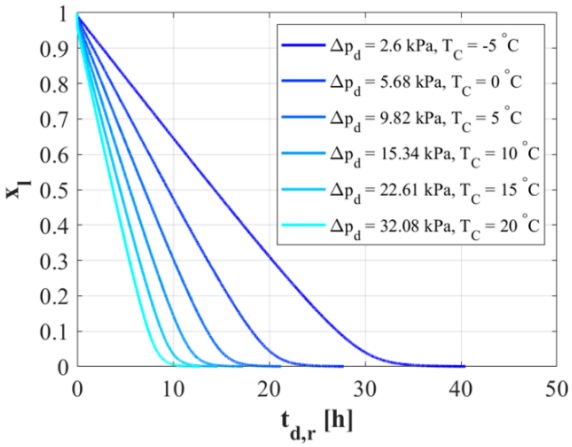

Figure 5.23: Evolution in time of LTM global conversion ratio during reaction discharge time for $SrCl_2$ 6-2-$MgCl_2$ 6-2 configuration, with different values of Δp_d.

Again, it is noteworthy that the reaction time seems to increase with an exponential trend as the parameter Δp_d tends to its lower limit, i.e. 0. Such feature is even more visible in Figure 5.24, which shows the trend of cold exergy production and $t_{d,r}$ as functions of Δp_d.

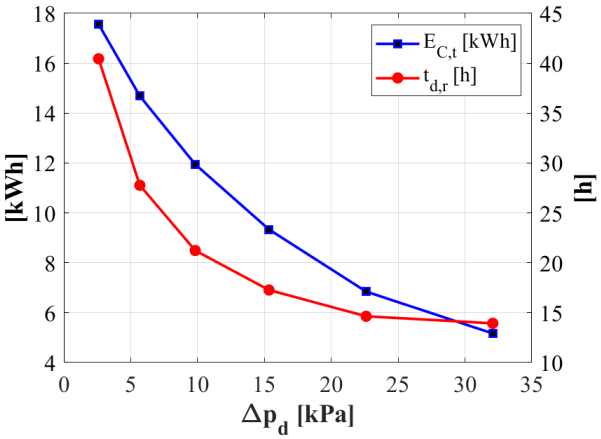

Figure 5.24: Reaction discharge time and cold exergy produced for $SrCl_2$ 8-1- $MgCl_2$ 6-2 configuration and different values of Δp_d.

Furthermore, another important implication is revealed: although it is beneficial to increase the pressure difference Δp_d in terms of reaction discharge time needed, it results to negatively affect the cold exergy production, since the refrigeration will unavoidably occur at higher temperature. Therefore, it is essential to properly find a compromise between refrigeration quality that the application must fulfill, and reaction time needed. An alternative solution to decrease the discharge reaction time without affecting the cold production temperature could be to shift the operating point **5** along the HTM equilibrium line, towards lower values of equilibrium temperature and pressure. Nevertheless, when applying this approach, it is important to prevent the operating pressure at point $\boldsymbol{p_5}$ from becoming lower than the admissible minimum pressure and that the intermediate sink temperature T_m becomes lower than the refrigeration temperature.

5.3.5 Summary of results from dynamic state analysis

- During synthesis/decomposition, if a reactor is oversized, it imposes its equilibrium condition to the whole system, due to its larger kinetics. On the other hand, if the reactors are equally sized, they evolve towards new equilibrium conditions, deviated from the HTM and LTM lines.
- Reaction kinetics represents a more impactful bottleneck on the overall cycle time, with respect to thermal masses for the analyzed TRSC.
- Although a salt-ammonia reaction presents the highest efficiency from the steady state point of view, it can reveal low performance in terms of dynamic behavior. In fact, $NiCl_2$ 6-2 is the HTM which results in the lowest value of power density. The HTM with best dynamic performance is $MgCl_2$ 6-2, with mass and volume power density of 1.36 W/kg, and 1.47 kW/m^3.
- Operating with a value of pressure ratio close to β_{max} results in very large reaction charge time. Specifically, reaction charge time increases exponentially as β tends to β_{max}. Hence, a trade-off between work production and cycle time should be carried out to select the most suitable value for β.
- As the initial pressure difference between LTR and HTR before desorption/adsorption in the discharge phase tends to zero, the reaction discharge time tends to infinite. A possible strategy to decrease the reaction discharge time is to increase the equilibrium pressure of LTM before discharge phase. However, an optimal trade-off between cycle time and cold exergy production should be found.

6. Conclusions

Thermochemical resorption cogeneration systems can fulfill diverse energy requirements, providing multiple functions, depending on the specific application scenario. They are suitable for low-grade thermal energy storage, not only in industrial applications for waste heat recovery but also for renewable thermal energy exploitation, e.g. in solar thermal plants, with intermittent or seasonal storage configuration. In this thesis, a Thermochemical Resorption cycle for storage of low-grade heat and cogeneration of power and cold (TRSC) has been investigated. Steady state and dynamic state analyses have been carried out, with the focus on the transient behavior of the components and the relationship between operating conditions and system performance. In chapter 1, the general background of low-grade heat utilization is presented, and the sorption working principles and technologies are described. After a state of the art of sorption cogeneration systems, the motivations and scope of this work are delineated. In chapter 2, the TRSC is described in detail, and possible application scenarios are illustrated. In chapter 3 the methods used for the implementation of the thermodynamic cycle, the sized system steady state model, and the dynamic state model are presented. Validations to support the features of the models and the assumptions done are also carried out. In chapter 4 the specific TRSC application explored in this work through the models is presented. Hence, the reactive materials and the model parameters are defined. Finally, the strategy adopted for the selection of suitable solid/gas reactions depending on the cycle operating conditions is described. In chapter 5 the results obtained are presented and discussed. Therefore, the following conclusions can be summarized:

1) The steady state analysis revealed that the thermodynamic performance of the TRSC increases as the temperature of the thermal energy to be stored decreases. Such a feature makes it more suitable for low and ultra low-grade heat storage. However, the thermal masses of the reactors have the highest impact on the performance of the analyzed system in terms of first and second law efficiencies. Selecting solid/gas reactions with higher specific adsorption capacity results in a lower effect of the thermal masses, thus higher system performance.
2) The dynamic model was used to investigate and physically the evolution in time of relevant quantities of TRSC during the cycle working steps. An interesting result is inferred by observing the reaction charge phase on the Clapeyron diagram for two differently sized TRSC systems: if the reactors are equally sized to exchange the same stoichiometric quantity of refrigerant, they are subjected to the same driving force and reach an equilibrium state deviated from the HTM and LTM equilibrium lines. On the other hand, if one of the reactors is oversized with respect to the other, it drives the couple reactions towards the equilibrium line relative to the oversized reactive material.
3) Although a specific configuration results in high steady state performance, it could reveal low-performing in terms of cycle time. Hence, it is essential to carry out both steady state and dynamic state analyses for this type of system. Reaction kinetics is the main factor that negatively impacts the system performance in terms of cycle time. The larger the deviation from the reaction equilibrium line, imposed at the beginning of

adsorption/desorption phases, the higher the reaction driving force. Therefore, it is not convenient to adopt a scroll expander with a pressure ratio close to its maximum allowable value, since it would imply a lower equilibrium drop and a larger cycle time. Instead, a proper trade-off between work that can be produced, and reaction charge duration should be met. It was also found that imposing high pressure difference between the reactors before triggering simultaneous adsorption\desorption allows to obtain high pressure equilibrium drops, thus low reaction time.

6.1 Suggestions for future work

Although preliminary results and conclusions have been obtained through the numerical models in this study, future work is necessary to better understand the potential of thermochemical resorption cogeneration cycles for low-grade heat exploitation. Suggestions for future work are summarized as follows:

- Further case studies should be analyzed in steady state with different sizing of the TRSC, i.e. with a production of power and cold set at different orders of magnitude. Hence, a parametric study could be carried out in which the impact of the cycle operating conditions (e.g. T_H, β) and intrinsic properties of reactive mixtures on the performance is evaluated at different system sizes.
- More rigorous validation should be conducted on the dynamic model for TRSC implemented in this work through experimental data. For instance, a wide range of solid/gas reactions should be experimentally investigated to estimate the semi-empirical coefficients to be adopted in the kinetic model.
- More detailed and accurate features of the numerical models should be implemented to study TRSC on a component scale. For instance, a model to estimate the global heat transfer coefficients of the heat exchanger, and to evaluate their influence on the cycle time could be developed.
- Additional effort should be invested to develop models capable to represent the whole transient cycle on the Clapeyron diagram. Real resorption cycles could be represented through two distinct continuous lines which evolve near the equilibrium lines of the two reactive material adopted.
- Further investigation should be carried out by developing a real case study in which TRSC is retrofitted to an industrial process for waste heat recovery or a renewable source-based system for heat storage. For example, the integration of TRSC in an existing plant could be analyzed to evaluate the advantages in terms of total efficiency gain and related savings.
- A detailed thermo-economic study and optimization should be carried out to evaluate the benefits of such a technology in terms of costs, revenues, and risks, compared to other low-grade heat technologies.

References

[1] Wang Cai T, Wang S, Cozzi L, Motherway B, Turk D. Towards a zero-emission, efficient, and resilient buildings and construction sector. 2017.

[2] Masson-Delmotte, V., P. Zhai, H.-O. Pörtner, D. Roberts, J. Skea, P.R. Shukla, A. Pirani, W. Moufouma-Okia, C. Péan, R. Pidcock, S. Connors, J.B.R. Matthews, Y. Chen, X. Zhou, M.I. Gomis, E. Lonnoy, T. Maycock, M. Tignor and TW. IPCC, 2018: Summary for Policymakers. In: Global Warming of 1.5°C. An IPCC Special Report on the impacts of global warming of 1.5°C above pre-industrial levels and related global greenhouse gas emission pathways, in the context of strengthening the global 2018.

[3] Administration USEI. International Energy Outlook 2019 2019.

[4] Interreg Central Europe. Low-grade waste heat utilization in the European Union 2017:3–9.

[5] I, Yu C, Chen R, Li JJ, Li JJ, Drahansky M, et al. State-of-the-Art Technologies on Low-Grade Heat Recovery and Utilization in Industry Janie. Intech 2012;i:13. https://doi.org/10.1016/j.colsurfa.2011.12.014.

[6] Verda V, Guelpa E. Metodi termodinamici per l'uso efficiente delle risorse energetiche. 2013. https://doi.org/10.15651/978-88-748-8652-4.

[7] Jouhara H, Khordehgah N, Almahmoud S, Delpech B, Chauhan A, Tassou SA. Waste heat recovery technologies and applications. Therm Sci Eng Prog 2018;6:268–89. https://doi.org/10.1016/j.tsep.2018.04.017.

[8] Lecompte S, Huisseune H, Van Den Broek M, Vanslambrouck B, De Paepe M. Review of organic Rankine cycle (ORC) architectures for waste heat recovery. Renew Sustain Energy Rev 2015;47:448–61. https://doi.org/10.1016/j.rser.2015.03.089.

[9] Zhang X, He M, Zhang Y. A review of research on the Kalina cycle. Renew Sustain Energy Rev 2012;16:5309–18. https://doi.org/10.1016/j.rser.2012.05.040.

[10] Nadeem F, Hussain SMS, Tiwari PK, Goswami AK, Ustun TS. Comparative review of energy storage systems, their roles, and impacts on future power systems. IEEE Access 2019;7:4555–85. https://doi.org/10.1109/ACCESS.2018.2888497.

[11] Steven Brown J, Domanski PA. Review of alternative cooling technologies. Appl Therm Eng 2014;64:252–62. https://doi.org/10.1016/j.applthermaleng.2013.12.014.

[12] Srikhirin P, Aphornratana S. A review of absorption refrigeration technologies 2001;5:343–72.

[13] Wang LW, Wang RZ, Oliveira RG. A review on adsorption working pairs for refrigeration 2009;13:518–34. https://doi.org/10.1016/j.rser.2007.12.002.

[14] Wang R, Wang L, Wu J. Adsorption refrigeration technology. 2014.

[15] Li TX, Wang RZ, Yan T, Ishugah TF. Integrated energy storage and energy upgrade, combined cooling and heating supply, and waste heat recovery with solid-gas thermochemical sorption heat transformer. Int J Heat Mass Transf 2014;76:237–46. https://doi.org/10.1016/j.ijheatmasstransfer.2014.04.046.

[16] Li TX, Wang RZ, Kiplagat JK, Chen H. Experimental study and comparison of

thermochemical resorption refrigeration cycle and adsorption refrigeration cycle. Chem Eng Sci 2010;65:4222–30. https://doi.org/10.1016/j.ces.2010.04.022.

[17] Wu S, Li TX, Yan T, Wang RZ. Experimental investigation on a thermochemical sorption refrigeration prototype using EG/SrCl2–NH3 working pair. Int J Refrig 2018;88:8–15. https://doi.org/10.1016/j.ijrefrig.2017.11.030.

[18] Li TX, Wu S, Yan T, Wang RZ, Zhu J. Experimental investigation on a dual-mode thermochemical sorption energy storage system. Energy 2017;140:383–94. https://doi.org/10.1016/j.energy.2017.08.073.

[19] Ma Z, Bao H, Roskilly AP. Seasonal solar thermal energy storage using thermochemical sorption in domestic dwellings in the UK. Energy 2019;166:213–22. https://doi.org/10.1016/j.energy.2018.10.066.

[20] Goswami DY. Solar Thermal Power Technology : Present Status and Ideas for the Future Solar Thermal Power Technology : Present Status and Ideas for the Future 2007;8312. https://doi.org/10.1080/00908319808970052.

[21] Tamm G. Theoretical and experimental investigation of an ammonia – water power and refrigeration thermodynamic cycle 2004;76:217–28. https://doi.org/10.1016/j.solener.2003.08.017.

[22] Jiang L, Wang LW, Roskilly AP, Wang RZ. Design and performance analysis of a resorption cogeneration system 2013:85–91. https://doi.org/10.1093/ijlct/ctt040.

[23] Yang Z, Qu M, Gluesenkamp KR. Ammonia-based chemisorption heat pumps for cold-climate heating applications : A comprehensive review ☆. Appl Therm Eng 2020;179:115674. https://doi.org/10.1016/j.applthermaleng.2020.115674.

[24] Classification S. Update on New Refrigerants Designations and Safety Classifications 2020.

[25] Wang L, Ziegler F, Roskilly AP, Wang R, Wang Y. A resorption cycle for the cogeneration of electricity and refrigeration. Appl Energy 2013;106:56–64. https://doi.org/10.1016/j.apenergy.2013.01.041.

[26] Lu Y, Wang Y, Bao H, Yuan Y, Wang L, Roskilly AP. Analysis of an optimal resorption cogeneration using mass and heat recovery processes. Appl Energy 2015;160:892–901. https://doi.org/10.1016/j.apenergy.2015.01.138.

[27] Jiang L, Roskilly AP, Wang RZ, Wang LW. Analysis on innovative resorption cycle for power and refrigeration cogeneration. Appl Energy 2018;218:10–21. https://doi.org/10.1016/j.apenergy.2018.02.174.

[28] Lu Y, Roskilly AP, Wang Y, Wang L. Study of a Novel Dual-source Chemisorption Power Generation System Using Scroll Expander. Energy Procedia 2017;105:921–6. https://doi.org/10.1016/j.egypro.2017.03.417.

[29] Bao H, Ma Z, Roskilly AP. Integrated chemisorption cycles for ultra-low grade heat recovery and thermo-electric energy storage and exploitation. Appl Energy 2016;164:228–36. https://doi.org/10.1016/j.apenergy.2015.11.052.

[30] Bao H, Ma Z, Roskilly AP. An optimised chemisorption cycle for power generation using low grade heat. Appl Energy 2017;186:251–61. https://doi.org/10.1016/j.apenergy.2016.06.080.

[31] Godefroy A, Perier-Muzet M, Mazet N. Thermodynamic analyses on hybrid sorption

cycles for low-grade heat storage and cogeneration of power and refrigeration. Appl Energy 2019;255:113751. https://doi.org/10.1016/j.apenergy.2019.113751.

[32] Jiang L, Wang LW, Zhang XF, Liu CZ, Wang RZ. Performance prediction on a resorption cogeneration cycle for power and refrigeration with energy storage. Renew Energy 2015;83:1250–9. https://doi.org/10.1016/j.renene.2015.06.028.

[33] Bao H, Wang Y, Roskilly AP. Modelling of a chemisorption refrigeration and power cogeneration system. Appl Energy 2014;119:351–62. https://doi.org/10.1016/j.apenergy.2014.01.012.

[34] Lu Y, Roskilly AP, Tang K, Wang Y, Jiang L, Yuan Y, et al. Investigation and performance study of a dual-source chemisorption power generation cycle using scroll expander. Appl Energy 2017;204:979–93. https://doi.org/10.1016/j.apenergy.2017.02.068.

[35] Neveu P, Domblides J-P, Castaing J. Diagrammes thermodynamiques relatifs aux equilibres solide/gas (1996). n.d.

[36] Lu HB, Mazet N, Spinner B. Modelling of gas-solid reaction - Coupling of heat and mass transfer with chemical reaction. Chem Eng Sci 1996;51:3829–45. https://doi.org/10.1016/0009-2509(96)00010-3.

[37] Lu HB, Mazet N. Mass-transfer parameters in gas-solid reactive media to identify permeability of IMPEX. AIChE J 1999;45:2444–53. https://doi.org/10.1002/aic.690451117.

[38] Wu S, Li TX, Yan T, Wang RZ. Advanced thermochemical resorption heat transformer for high-efficiency energy storage and heat transformation. Energy 2019;175:1222–33. https://doi.org/10.1016/j.energy.2019.03.159.

[39] Han JH, Lee KH, Kim DH, Kim H. Transformation analysis of thermochemical reactor based on thermophysical properties of graphite-MnCl2 complex. Ind Eng Chem Res 2000;39:4127–39. https://doi.org/10.1021/ie9904394.

[40] Kane M, Favrat D, Gay B, Andres O. Scroll expander organic rankine cycle (ORC) efficiency boost of biogas engines. ECOS 2007 - Proc 20th Int Conf Effic Cost, Optim Simul Environ Impact Energy Syst 2007;2:1017–24.

[41] Imran M, Usman M, Park BS, Lee DH. Volumetric expanders for low grade heat and waste heat recovery applications. Renew Sustain Energy Rev 2016;57:1090–109. https://doi.org/10.1016/j.rser.2015.12.139.

[42] Emhardt S, Tian G, Chew J. A review of scroll expander geometries and their performance. Appl Therm Eng 2018;141:1020–34. https://doi.org/10.1016/j.applthermaleng.2018.06.045.

[43] MAZET N, AMOUROUX M, SPINNER B. ANALYSIS AND EXPERIMENTAL STUDY OF THE TRANSFORMATION OF A NON-ISOTHERMAL SOLID/GAS REACTING MEDIUM. Chem Eng Commun 1991;99:155–74. https://doi.org/10.1080/00986449108911585.

[44] Goetz V, Spinner B, Lepinasse E. A SOLID-GAS THERMOCHEMICAL COOLING SYSTEM USING BaCl2/AND NiCl2 1997;22:49–58.

[45] Goetz V, Marty A. A model for reversible solid-gas reactions submitted to temperature and pressure constraints: simulation of the rate of reaction in solid-gas reactor used as

chemical heat pump. Chem Eng Sci 1992;47:4445–54. https://doi.org/10.1016/0009-2509(92)85122-R.

[46] Neveu P, Castaing J. Solid-gas chemical heat pumps: Field of application and performance of the internal heat of reaction recovery process. Heat Recover Syst CHP 1993;13:233–51. https://doi.org/10.1016/0890-4332(93)90014-M.

Appendix

Further results related to the $SrCl_2$ 8-1 – $MnCl_2$ 6-2 configuration analyzed in the dynamic state (Section 5.2) are presented.

A.1 Thermodynamic cycle

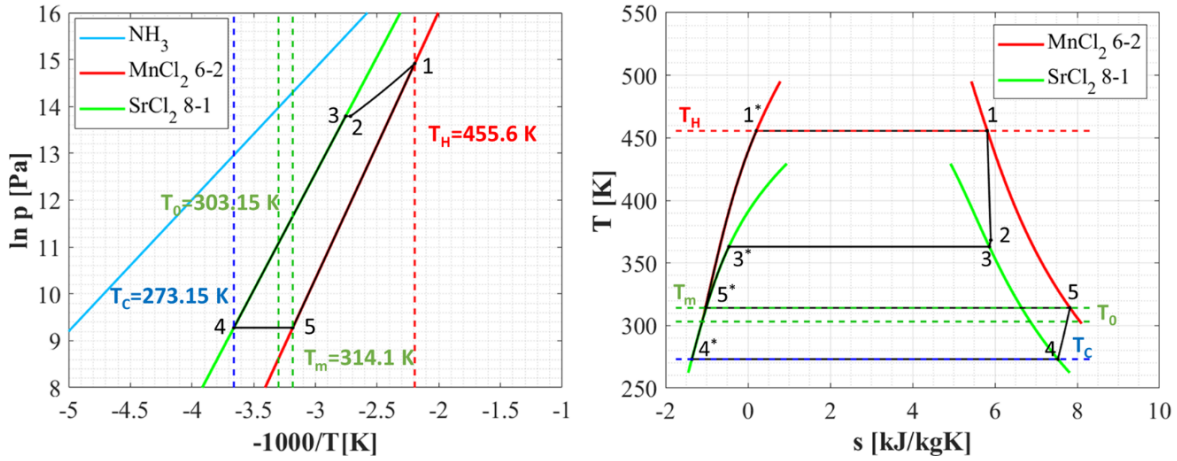

Figure A.1: Thermodynamic cycle of the $SrCl_2$ 8-1 – $MnCl_2$ 6-2 configuration on the Clapeyron diagram (left) and T-s diagram (Right).

Table A.1: Thermodynamic properties of the gaseous ammonia at each point of the cycle for the $SrCl_2$ 8-1 – $MnCl_2$ 6-2 configuration.

Point	p	T	h	s	v
	[bar]	[K]	[kJ/kg]	[kJ/kg/K]	[m^3/kg]
1	30	455.6	1849	5.816	0.06923
2	9.78	368.4	1672	5.902	0.1753
3	9.78	363	1659	5.866	0.1723
3*	9.78	363	-637.7	-0.461	-
4*	0.1	273.2	-929	-1.361	-
4	0.1	273.2	1500	7.531	12.47
5	0.1	314.1	1586	7.824	14.35
5*	0.1	314.1	-1196	-1.031	-
1*	30	455.6	-706.7	0.206	-

A.2 Discharge phase

The evolution in time of relevant quantities for the $SrCl_2$ 8-1 – $MnCl_2$ 6-2 during discharge phase is presented in the following section.

A.2.1 Precool phase

Figure A.1 shows the temperature evolution of the reactor components during precool stage.

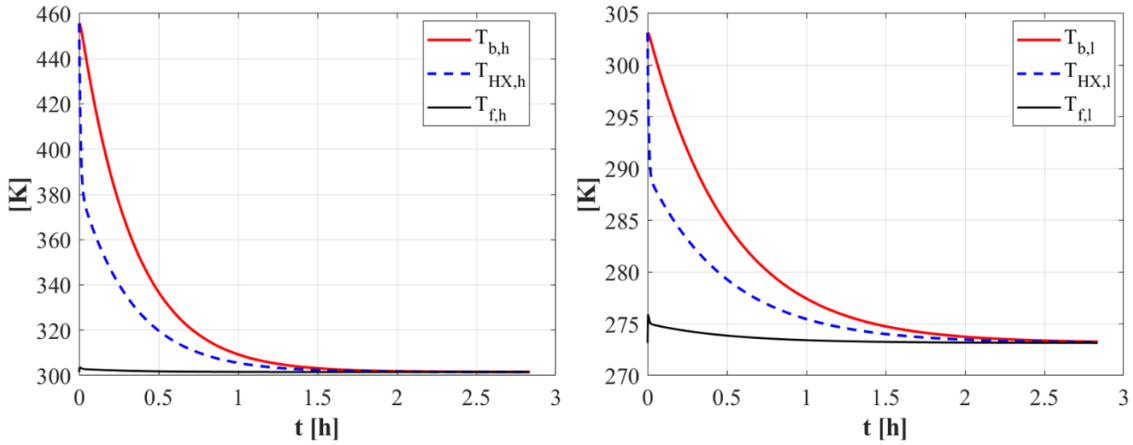

Figure A.2: Temperature evolution of the reactive bed T_b, heat exchanger T_{HX} and heat transfer fluid T_f during the precool phase relatively to HTR (left) and LTR (right).

It is noteworthy that the LTR needs more time than the HTR to reach the desired temperature. In fact, the LTR is in the complete adsorbed and its total mass is the sum between the LTM at low ammonization state and the total gaseous ammonia $m_{NH_{3,tot}}$. On the other hand, HTR's mass is only composed by the HTM at low ammonization state.

A.1.2 Reaction discharge phase

Figure A.3 represents the evolution in time of the reactors' global conversion rates and constraint pressure during the reaction discharge phase, while Figure A.4 shows the evolution in time of the gaseous ammonia mass flow rate. Note that in this case the reactors are subjected to the same non-equilibrium pressure since the scroll expander is bypassed. Moreover, as for the reaction charge phase, the curves can be divided into three time intervals, in which they have different trends.

1) The first part in which the variation is rapid, thus maximum driving force is imposed.
2) A second interval in which the driving force is constant, i.e. global conversion rates vary linearly, while pressure and mass flow rate are mostly constant.
3) Finally, in the third part, the reactions are almost complete and the driving force decreases.

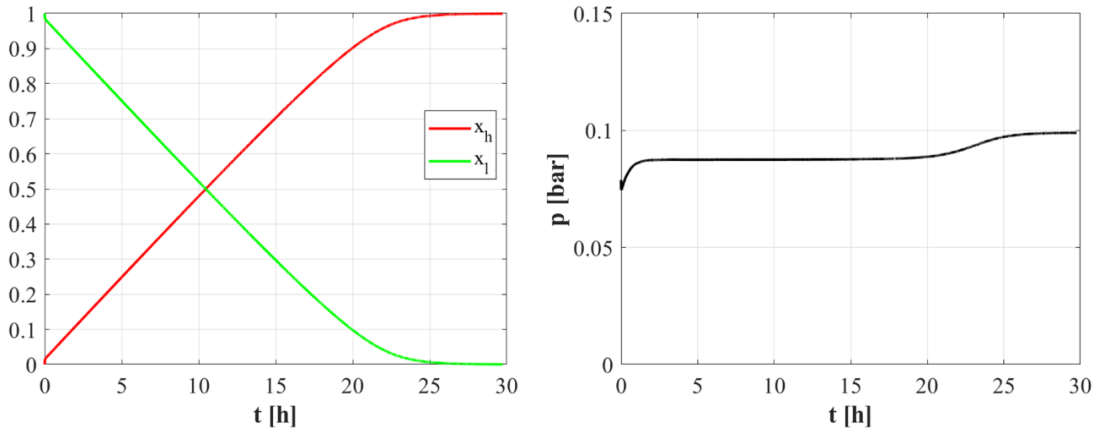

Figure A.3: Evolution in time of the global conversion rate (left) and of the constraint pressure (right) during reaction discharge phase.

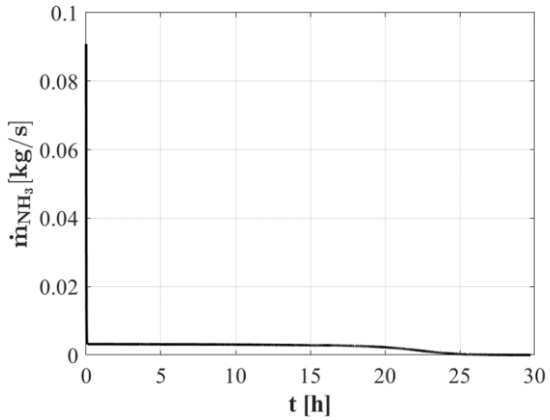

Figure A.4: Mass flow rate of ammonia during reaction discharge phase.

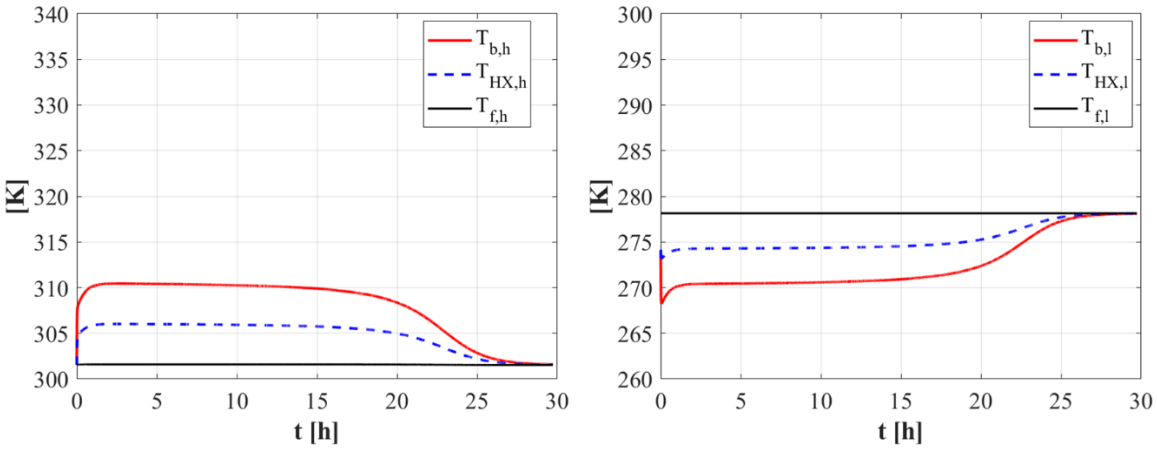

Figure A.5: Temperature evolution of the reactive bed T_b heat exchanger T_{HX} and heat transfer fluid T_f during reaction discharge phase, relatively to HTR (left) and LTR (right).

Figure A.5 represents the evolution in time of temperature of the reactor components. As for the charge phase, the reactors undergo an initial temperature variation depending on whether synthesis or decomposition occur: HTR is subjected to exothermal adsorption, i.e. its temperature increases. On the contrary, LTR undergoes endothermal desorption, and its temperature decreases.

A.1.3 Representation on Clapeyron diagram

Figure A.6 represents the reaction discharge phase on the Clapeyron diagram,

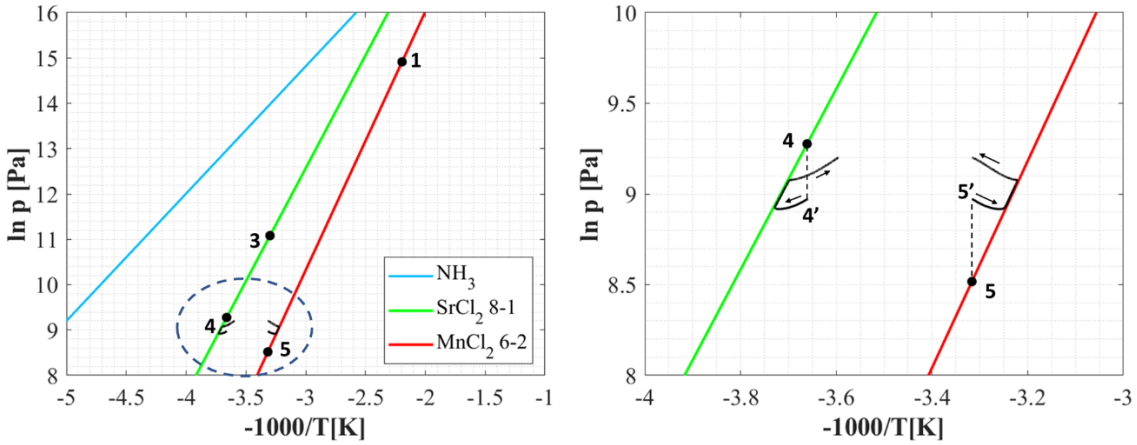

Figure A.6: Reaction discharge phase on the Clapeyron diagram.

As for the reaction charge phase, the reactors are sized in a such way that they have the potential to adsorb/desorb the same amount of gaseous ammonia. Thus, no reactor imposes its kinetics to the other and the system evolves towards a new state of equilibrium, different from the equilibrium state related to the HTM and LTM reactions. It is interesting to notice that, differently from the reaction charge phase, the new equilibrium does not coincide with the points **4'** and **5',** which are the conditions instantaneously imposed as the reactors are connected. Such a feature could be related to the different equations imposed in the model for the HTF in the reaction discharge phase.